

Characterisation and Functionality of SnO₂ Gas
Sensors Using Vibrational Spectroscopy

Schwingungspektroskopische Charakterisierung der
Funktionsweise von SnO₂-Sensoren

DISSERTATION

der Fakultät für Chemie und Pharmazie
der Eberhard-Karls-Universität Tübingen

zur Erlangung des Grades eines Doktors
der Naturwissenschaften

2005

vorgelegt von
SERPIL HARBECK

Tag der mündlichen Prüfung:	04.03.2005
Dekan:	Professor Dr. S. Laufer
1. Berichterstatter:	Privatdozent Dr. U. Weimar
2. Berichterstatter:	Professor Dr. V. Hoffmann

Content

1	Introduction and Motivation	1
1.1	Introduction	1
1.2	Motivation	3
2	Basics and Survey	5
2.1	Introduction to IR techniques	5
2.2	Diffuse Reflectance Spectroscopy DRIFT	6
2.2.1	Advantages of DRIFT Spectroscopy	6
2.2.2	Disadvantages	7
2.3	Reflection Types of Electromagnetic Radiation on Mat Surfaces	8
2.4	Intensity Distribution of Diffuse Reflectance: Law of Lambert	10
2.5	Theory of Diffuse Reflectance: Theory of Kubelka-Munk.....	12
2.6	Specular Reflectance.....	15
2.6.1	Methods for Minimizing Specular Reflectance	16
2.7	Diffuse Reflectance on Absorptive Materials	18
2.8	Adsorption Processes on Solid Surfaces.....	19
2.8.1	Physisorption	19
2.8.2	Hydrogen Bonding.....	20
2.8.3	Chemisorption.....	20
2.8.4	Ionosorption	22
2.9	Electronic Structure of Semiconductors	22
2.10	IR Characterisation of Metal Oxide Surfaces	25
2.11	Adsorption Mechanism of Selected Molecules on MOX surfaces	28
2.11.1	Oxygen Adsorption	28
2.11.2	Water Adsorption	33
2.11.3	CO Adsorption.....	42
2.12	Influence of Surface Additives on the Sensing Mechanism.....	50
2.13	Correlations between Spectroscopic and Electrical Data	51
3	Experimental Section	55
3.1	IR Spectrometer	55
3.2	DRIFT-unit	56
3.3	Sample Chamber	57
3.4	Gas Mixing Bench	58
3.5	Sensor Heating.....	59

3.6	Samples.....	60
3.7	Drying and Thermal Activation of the Sensors	62
3.8	Sampling of Gases in the Exhaust for the Photoacoustic IR Spectrometer	63
3.9	Measurement Protocol	64
3.10	Band Analysis.....	64
4	Results and Discussion	67
4.1	Characterisation of the Samples	68
4.1.1	Characterisation of Differently Prepared SnO ₂ Powders at RT	68
4.1.2	Characterisation of Un-doped and Pd-doped Sensors at RT.....	75
4.1.3	Temperature Effects.....	80
4.1.4	CO Measurements.....	90
4.1.5	Comparison of the Un-doped and Pd-doped Sensor.....	138
5	Conclusions and Outlook.....	143
5.1	Reaction Mechanism at Low Temperature (150°C)	144
5.1.1	In the Absence of Humidity	144
5.1.2	In the Presence of Humidity.....	144
5.2	Reaction Mechanism at High Temperatures (300 and 350°C)	146
5.2.1	In the Absence of Humidity	146
5.2.2	In the Presence of Humidity.....	146
5.3	Outlook.....	147
6	References	149

List of Symbols

B	a) Density of radiation b) Rotation constant
c	a) Concentration b) Speed of light
d	a) Thickness of Layer b) Distance between the interacting particles
e	Elementary charge
E	Extinction (Law of Lambert-Beer)
E_{attr}	Attraction energy
E_C	Lower edge of conduction band energy
E_F	Fermi energy
E_g	Band gap energy
E_{pot}	Potential energy
E_{rep}	Repulsive energy
$f(R_\infty)$	Kubelka-Munk unit for the intensity of the diffuse reflected radiation
g	Scattering anisotropy factor
h	Planck's constant
I	Intensity
I_s	Intensity of true specular reflection
I_{ds}	Intensity of diffuse specular reflectance
I_d	Intensity of diffuse reflectance
$J_{(x=0)}$	Radiant flux contrary to incoming radiation
k	a) Linear absorption coefficient b) Boltzmann constant
K	Absorption coefficient
n	Ratio of the refraction index of the sample to that of the surrounding medium

N_C	The density of the free charges in the conduction bands
N_D	Ionised donor density
N_i	Number of ions in the space charge area
n_s	The density of the free charges on the surface
ppm	part per million
R	a) Reflection b) Resistance
r	Distance between two atoms in a molecule
s	Linear scattering coefficient
S	Scattering coefficient
S_0	Irradiance
T	Transmission
T	Temperature
$V_0 (V_0^{\cdot}, V_0^{\cdot\cdot})$	Oxygen vacancies (single ionised, double ionised)
V_s	Schottky barrier
α	Incident angle
β	Observation angle
δ	Symbol for the deformation mode of a vibration
ε	a) Extinction coefficient b) Depth of potential c) Permittivity
ε_0	Permittivity of free space
Θ	Angle of incident light
κ	Absorption index
λ	Wavelength
ν	a) Frequency b) Symbol for stretching mode of vibration
$\tilde{\nu}_P, \tilde{\nu}_R$	Frequency of the maxima of the P and R rotation bands
Φ	Electrical potential

Φ_b Potential in the bulk
 Φ_x Potential in the edge layer

List of Abbreviations

ATR	Attenuated Total Reflection
cus	Coordinatively unsaturated sites
DC	Direct Current
DRIFT	Diffuse Reflectance Infrared Fourier Transform
EPR	Electron Paramagnetic Resonance
ES	Emission Spectroscopy
FT	Fourier Transformation
FTIR	Fourier Transform Infrared
HOMO	Highest Occupied Molecular Orbital
IR	Infrared
IRRAS	Infrared Reflection Absorbance Spectroscopy
ISS	Ion Scattering Spectroscopy
KM	Kubelka-Munk
LEED	Low Energy Electron Diffraction
LUMO	Lowest Unoccupied Molecular Orbital
MOX	Metal Oxide
PAS	Photo Acoustic Spectroscopy
r.h.	Relative humidity
RT	Room Temperature
TPD	Temperature Programmed Desorption
UPS	Ultraviolet Photoelectron Spectroscopy
XPS	X-ray Photoelectron Spectroscopy

1 Introduction and Motivation

1.1 Introduction

Gas sensors based on metal oxide sensitive layers are playing an important role in the detection of toxic pollutants (CO, H₂S, NO_x, SO₂ etc.) and inflammable gases (H₂, CH₄, hydrocarbons etc.) and in the control of industrial processes. Tin dioxide is widely used as a basic material for the preparation of gas sensing devices operated in these applications.

It is recognized that together with atmospheric oxygen the presence of humidity greatly influences the gas detection. Accordingly, it is important to understand the role of water vapour in the sensing mechanism. For this, there is a need to complete the phenomenological experiments with spectroscopic knowledge [1]. The latter one should be acquired in the same conditions in which this type of gas sensors is operated, namely: in air, in the presence of humidity and with the sensors heated above 100°C.

Infrared techniques seem to be most suitable for such tasks. Up to now, in the field of metal oxide sensors several phenomenological and spectroscopic investigations were performed over the past three decades. However, the first spectroscopic investigations on sensors under operating conditions were conducted only recently by Benitez et al. [2] and Pohle et al. [3, 4].

In the first case [2], a DRIFT study of the reversibility of CdGeON sensors towards oxygen exposure was performed. Their interest was directed more towards the bulk material changes as a result of O₂ reaction.

Pohle et al. studied adsorption of water vapour and oxygen on different metal oxides (GaO₃, WO₃, AlVO₄, Co₃O₄) thick film gas sensors in various operating conditions using IRES (Infrared Emission Spectroscopy). Among others, they found from the spectroscopic and electrical measurements a correlation between water adsorption and the evolution of the surface

hydroxyl group concentration and in this way it was proved that IR spectroscopy is applicable for the study of surface reactions on sensors.

In our previous experiments on differently prepared SnO₂ powders at room temperature (RT) [6], we found several surface species like different OH groups, coordinated water, oxygen ions and carbonate ions, differently hydrated proton species (H₃O⁺, H₅O₂⁺, H₇O₃⁺ etc. as defined in [6]). Furthermore, added CO molecules interact with specific terminal OH groups, water and oxygen ions at different reaction rates to form covalently bound carboxylate and carbonates groups. Adsorption according to a Langmuir isotherm of CO on the surface was also observed. These results differed from those of resistance and work function measurements [7], which suggested a surface mechanism where CO interacts with surface terminal hydroxyl groups forming CO₂ with subsequent release of electrons to the solid and a proton transfer to a surface oxide anion. This mechanism would have been supported by an increase of the absorption bands belonging to rooted OH groups, which was not observed in our measurements.

The disagreement between the electrical and spectroscopic data can be caused by

- different pre-treatments of the samples (the powders were heated up to 370°C under vacuum conditions, the sensors were heated at 300°C in ambient air),
- different measurement conditions (powder at RT and under vacuum, sensors at various temperatures and humidity levels in synthetic air),
- CO concentration (the measurements on powder were performed with pure CO, the electrical and work function measurements in the range of 30-200 ppm CO in air),
- the presence of the substrates and electrodes, known to play a role in the sensing mechanism, for the case of sensors [8].

Accordingly, the main goal of the currently performed work is to bridge the gap between phenomenological and spectroscopic methods. This is

done by simultaneously characterising the thick film SnO₂ sensors by electrical and spectroscopic methods under working conditions with a special interest in

- following the surface species evolution (and their electrical counterpart) induced by the change of temperature
- understanding the reaction mechanism between sensors and CO at various humidity levels.

Up to now several home made thick film sensors with different grain sizes and with different additives (Pt, Pd, Au) were tested by several methods (electrical measurements, work function measurements, UHV spectroscopy etc.) [9, 10]. For CO detection the Pd-doped sensor with the grain size 10 nm was found the most sensitive sensor in humid air. Therefore, DRIFT measurements were performed on un-doped and Pd-doped sensors, in order to understand the reaction mechanism and the differences induced by doping.

1.2 Motivation

The goal of this work is to improve the detection of surface species of SnO₂ thick film gas sensors under their working conditions (at elevated temperatures and in humidity) using DRIFT (Diffuse Reflectance Infrared Fourier Transform) spectroscopy, and to correlate the sensor signals with the relative changes of the DRIFT spectra. Although several spectroscopic investigations were performed in the last three decades, the reaction mechanisms between the sensor surface and gas are not completely understood. One of the main reasons for this might be the fact that the spectroscopic investigations were performed on very well defined model systems applying experimental techniques, which are usually performed under conditions far from the sensors' working conditions. Diffuse reflection infrared spectroscopy is one of the possible spectroscopic techniques, which allows performing measurements in the working condition of gas sensors.

Motivation

Its high sensitivity for the detection of surface species makes this technique the best possible choice. Therefore in this work, DRIFT investigations were conducted for the characterisation of un-doped and Pd-doped thick film sensors. Additionally, CO adsorption processes on both types of sensors were studied with DRIFT technique for the completion and/or verification of the results obtained by various phenomenological investigations performed previously on the same samples.

2 Basics and Survey

In this chapter an overview of the different infrared techniques is given, and various reflection types which occur after the interaction of electromagnetic radiation with the surface of materials are introduced. Basics of diffuse reflectance as well as basics of adsorption processes on the metal oxide surfaces for the selected gases of interest for this work (oxygen, water and carbon monoxide) are presented. Finally, this chapter presents an extensive overview on infrared spectroscopic literature on different metal oxide (MOx) materials. Additionally, the influences of the adsorption processes on the sensor resistance as well as correlation between the electrical and infrared spectroscopic data are shown.

2.1 Introduction to IR Techniques

Different IR techniques were developed in the past for the characterisation of a variety of applications, depending on the nature of the sample. One of the mostly used IR techniques is based on transmission. However, it is only applicable for transparent samples and with the transmission technique opaque samples cannot be studied as well as surface species in very low concentrations cannot be detected. In order to overcome these problems many other techniques were developed: emission (ES), reflection absorption (IRRAS), attenuated total reflection (ATR), photo acoustic (PAS), and diffuse reflectance (DRIFT) spectroscopy. For opaque samples, DRIFT or ES are the most suitable techniques. ES is capable of measuring opaque samples at high temperatures. IRRAS is applicable for thin films (thickness of 1-100 μm) of polymers, oils or lacquer deposited on metals. The ATR technique is used for the detection of adsorbed species, determination of their orientation, and characterisation of (ultra)thin films. In this technique, the ATR-crystal (as substrate, reference) must be transparent in the IR region and the refractive index of the sample must be

smaller than the refractive index of the substrate. Semiconductor materials like Si, ZnSe, Ge are mostly used substrates in this technique. Photoacoustic spectroscopy can be applied to almost all types of samples. It is a useful technique in particular for the investigation of depth profiling experiments on the surface of coated and laminar materials as well as for studies of aging, curing and diffusion processes into or out of a polymer matrix.

2.2 Diffuse Reflectance Spectroscopy DRIFT

Diffuse Reflectance has been employed for a long time as a versatile sample analysis tool for ultraviolet, visible and infrared spectroscopic analysis [11]. Initially, its use was restricted to the UV/visible or near-infrared regions of the spectrum because of the low energy throughput of many diffuse reflectance sampling devices, restriction in hardware and acquisition procedure. Following the advent of the Fourier Transform Infrared Spectrometers (FTIR) and improvements in diffuse reflectance accessory design, DRIFT became practical for the use in the mid-infrared region.

Diffuse reflectance spectroscopy is one of the most suitable methods for an examination of rough and opaque samples. The technique is especially suitable for the detection of surface species in low concentration. Additionally, diffuse reflectance measurements can be conducted on heated samples. Since the sensitive layer of the examined sensor is polycrystalline SnO₂ and its working temperature is between 200 and 400°C, it was therefore considered most suitable for the characterisation of thick film SnO₂ sensors.

2.2.1 Advantages of DRIFT Spectroscopy

Minimal or no sample preparation: There is no need for a preparation of a self-support disc like in transmission spectroscopy. The sample can be measured directly. In transmission IR measurements the sample must

usually be healed up by thermal activation to obtain the same transparency for every sample.

High sensitivity: Since the beam travels in the sample due to multiple scattering, diffraction and interaction of the light with the particles of the sample the area of the surface scanned with IR light is 100 to 1000 times larger than in the case of transmission (long path length). Therefore, this method is very suitable for the measuring species in low concentration.

High versatility: non-reflective materials, including highly opaque or weakly absorbing materials, irregular surfaces or coatings, such as polymer coatings on glass fibres, intractable samples through the use of specialized sampling devices can be analysed by this technique.

Capability of performing of the measurements under real life conditions: Up to now, several spectroscopic investigations (XPS, UPS, LEED, IR) were performed on metal oxides. However, all measurements were performed either on very well defined model systems or on the powders at RT mostly under vacuum after varying pre-treatments. However, results obtained by phenomenological and spectroscopic experiments were not in agreement, since different surface species exist on the surface depending on the temperature and humidity conditions of the sample. The DRIFT technique allows the detection of the surface in different conditions and makes it possible to compare or correlate results obtained by different methods.

2.2.2 Disadvantages

Separation of the diffuse reflectance from the specular reflectance: Both types of reflectance always occur together. Occurrence of the specular reflectance in the reflection spectra causes a shifting of band maxima and band contortions. In order to eliminate this unwanted specular reflectance a special unit is needed, which contains a complex mirror system.

Adjustment: Since the amount of the diffuse reflectance depends strongly on the angle of incident and angle of observation of the IR radiation, a very

sensitive adjustment of the system is needed. An insufficiently sensitive adjusted system will lose spectral information. Since the number of degrees of freedom of the mirrors is between two and four (depending on the DRIFT-unit, there are companies with different set ups and different models), it is difficult to find the right angle. A good adjustment can take several days.

Sample positioning: The orientation of the sample surface must be strictly planar, even small changes in the arrangement of the sample will influence the intensity of the recorded diffuse reflectance noticeably.

2.3 Reflection Types of Electromagnetic Radiation on Mat Surfaces

When infrared radiation is focused onto a surface, it is reflected in several ways. Figure 2.1 presents the different types of reflection pathways on rough surfaces. First, radiation can be reflected off the top surface at an angle of reflection equal to the incident angle. This reflection mode represents the true specular reflection (I_s), which is a function of the complex refractive index and the absorptivity of the material. This mode of reflectance dominates on smooth surfaces such as optical mirrors.

Second, the light can undergo multiple reflections on the surface without penetrating into the material. This reflection mode (I_{ds}), called diffuse specular reflectance, is also a function of the complex refractive index.

The third mode of interaction, true diffuse reflectance (I_d), results from the penetration of the incident beam into one or more sample particles and subsequent scattering from the sample matrix. The resulting radiation may emerge at any angle relative to the incident angle. Since it has travelled through the particles it contains high absorption characteristics of the sample material.

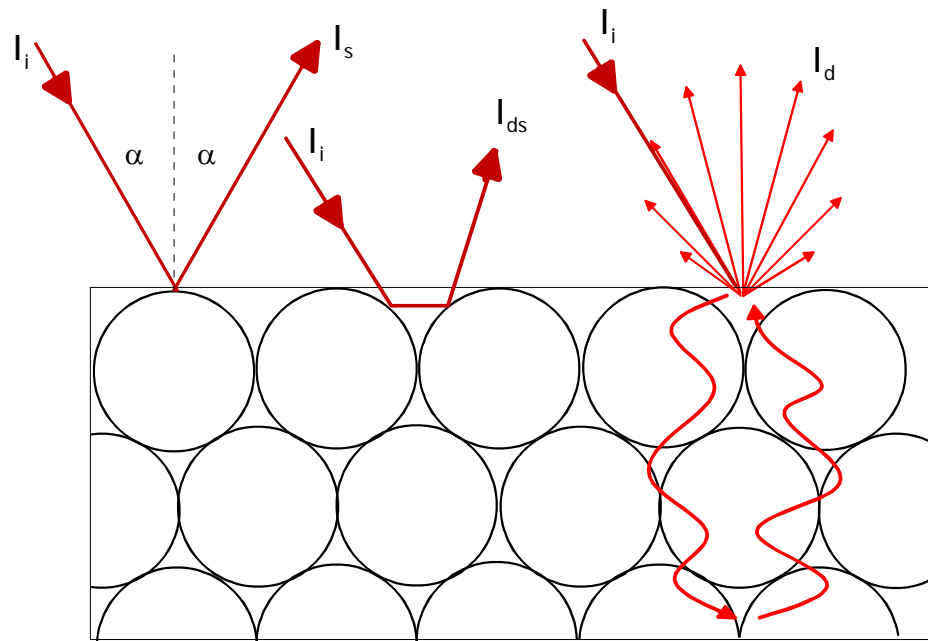


Figure 2.1: Different reflection types of radiation. I_s : specular reflectance, I_{ds} : diffuse specular reflectance, I_d : diffuse reflectance, I_i : incident beam.

The DRIFT method becomes more effective when the specular part of the total reflection is smaller. In real life it is not possible to separate all reflectance types, however there are some technical means to minimize the contribution of the specular reflectance. In the measurements performed in this work, the presence of the diffuse specular reflection was observed as a side effect through the detection of gaseous species like CO_2 . Since the presence of CO_2 in the spectrometer and sample chamber is excluded, CO_2 in the gas phase must be only in the sample. This side effect can be explained by the nature of the sample, which is a polycrystalline material. This polycrystallinity of the sample promotes multiple reflectance of the infrared radiation the grains acting as mirrors without penetration into grains. Thus the radiation pathway is elongated by the multiple reflections within the sample (sensor and substrate) and it enables the detection of gaseous species in the cavities. The measured P-R distance confirmed that the gaseous CO_2 is present in the cavities, since it is smaller than that expected for the measurement temperature (Figure 2.2). This observation is discussed in more detail in section 4.1.3.3.

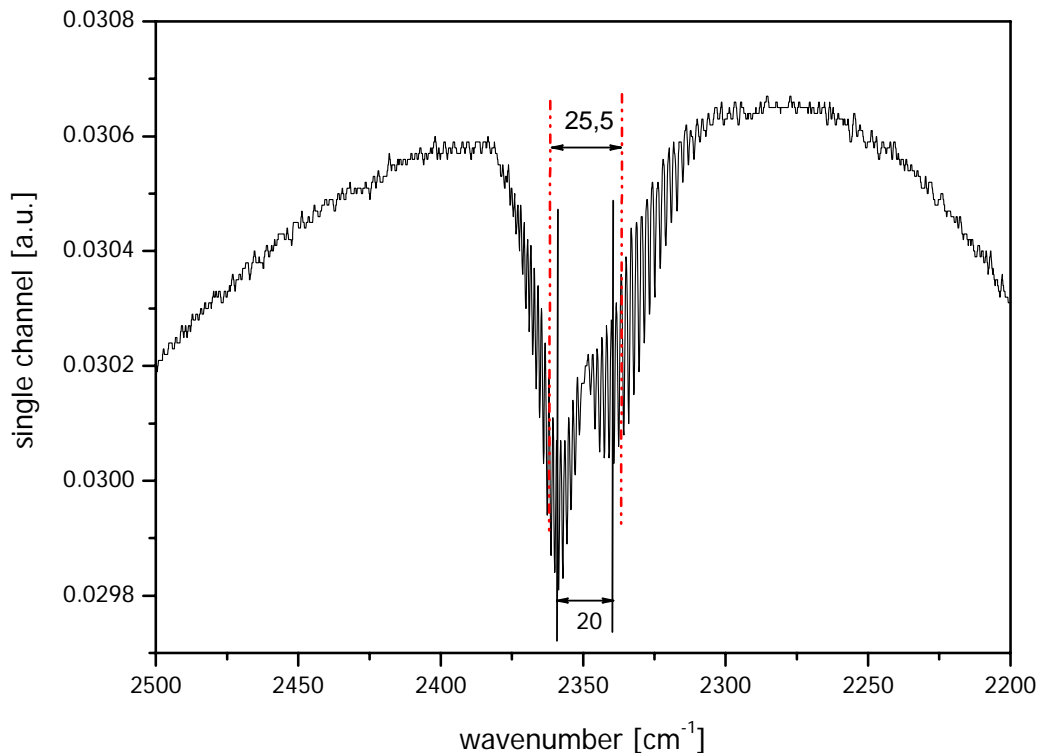


Figure 2.2: DRIFT-Spectrum of a tin dioxide sensor in the CO₂ spectral region. The spectrum was recorded with a spectral resolution of 0.5 cm⁻¹ at RT in synthetic air.

Gaseous CO₂ and H₂O were identified in the pores of some minerals like beryl and cordierite by high temperature infrared spectroscopy. Rossman et al. reported that structurally bound water in the pores starts partitioning into an unbound state with the characteristics of a gas above 400°C. The authors observed that the process is fully reversible and the dehydration occurs after most of the water is in an unbound state. Contrary to water, 40% of CO₂ still remained after heating to 800°C [12].

2.4 Intensity Distribution of Diffuse Reflectance: Law of Lambert

When infrared light arrives at matt surfaces, it will be partly refracted, partly reflected and diffracted, depending on the wavelength. In the case of short wave lengths (in comparison to the dimension of the crystal) the angular distribution of the diffracted part is small. Within the limit of $\lambda \rightarrow 0$ no diffraction pattern can be observed, and reflection can be described individually. Thus, the crystals are like mirrors and oriented in every

possible direction, and the radiation will be reflected into every solid angle of the half space, from which the radiation originated without penetration into the grains. This describes the above mentioned specular diffuse reflectance.

According to this consideration it is plausible that the part of specular reflection decreases with the grain size of the sample.

Precondition of ideal diffuse reflectance is that the radiation penetrates into the grains and the radiation is reflected into each solid angle of the half space, from which the radiation originated. In order to observe the diffuse reflected part of the radiation, the grain size of the sample must be smaller than the wavelength of the radiation. Particularly in the case of high wave lengths (comparable with the crystal size or higher) the different processes (diffraction, reflection and refraction) cannot be separated.

Lambert laid down the first law of diffuse reflectance, which is given by

$$\frac{dI_r / df}{d\varpi} = \frac{\text{const} \cdot S_0}{\pi} \cos \alpha \cdot \cos \vartheta = B \cdot \cos \vartheta \quad \text{Eq. 2-1}$$

where:

$\frac{dI_r / df}{d\varpi}$: the radiation efficiency of the reflectance per cm^2 and solid

angle,

S_0 : Irradiance

α, ϑ : Incidence angle, observation angle

B : Density of radiation $\left[\frac{\text{watt}}{\varpi \cdot \text{cm}^2} \right]$

The reflected radiation efficiency per cm^2 and solid angle is proportional to the cosine of the incident angle and cosine of the observation angle (Cosine law by Lambert). The constant indicates the part of the incident radiation efficiency, which is reflected. It is always smaller than one, because a part of the radiation is always absorbed.

Plotting the measured radiation efficiency as a function of the radius vector ϑ results in a polar curve called "indikatrix". Accordingly, from the equation 2-1, one obtains a circle which is tangent to the radiant area (Figure 2.3).

The diameter of the "indikatrix" is proportional to the irradiance. The reflectance from a unit area into a unit solid angle is only angle isotropic in regard to the azimuth and not in regard to ϑ .

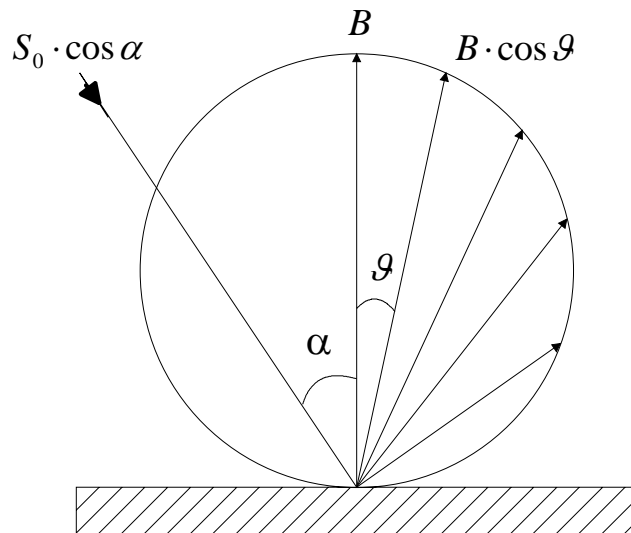


Figure 2.3: Angular distribution of the Lambert radiator [14].

2.5 Theory of Diffuse Reflectance: Theory of Kubelka-Munk

For the description of the diffuse reflectance of a scattering layer P. Kubelka and F. Munk developed a well-accepted theory [13]. This "Kubelka-Munk theory" is valid under the following conditions:

1. The sample must be planar. Non-planar geometries can be described only when additional assumptions are made.
2. The sample must have no edge loss.
3. The optical inhomogeneities in the sample that account for the scattering must be far smaller in size than the thickness of the sample and must be uniformly distributed over the sample.
4. The illumination used must be homogeneous and diffuse.
5. The sample must be made from a turbid material and have a constant finite thickness.

6. The sample's boundaries must not exhibit specular reflectance.
7. The sample must be weakly absorbent.

Kubelka-Munk assumes a sample, which is illuminated diffusely from above, and the absence of boundary reflections. Thus there are only two semi-diffuse fluxes inside the sample, one travelling down and one travelling up. The exact calculation of the total diffuse illumination results in a middle optical path length that is twice thickness of the layer [14, p.110]. Scattering is described by the diffuse scattering coefficient S , absorption by the diffuse absorption coefficient K .

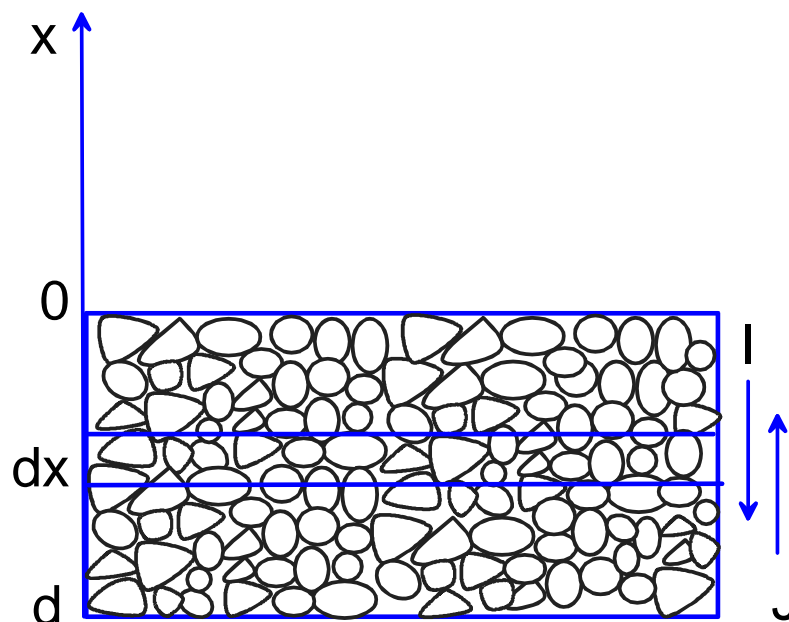


Figure 2.4: Radiation stream in the powder sample for the derivation of the concurrent differential equation according to Kubelka-Munk.

When radiation with the intensity I penetrates (in x direction) through an infinitesimal layer of thickness dx , the quantity of the absorbed radiation is $K \cdot I \cdot dx$, the quantity of the scattered radiation is $S \cdot I \cdot dx$, and the quantity of the radiant flux S coming from the bottom side is $S \cdot J \cdot dx$. The same consideration for the radiant flux is valid also in $-x$ direction (Figure 2.4, Equation 2-2 and 2-3).

$$-\frac{dI}{dx} = (K + S)I - SJ \quad \text{Eq. 2-2}$$

$$\frac{dJ}{dx} = (K + S)J - SI \quad \text{Eq. 2-3}$$

The definition of the reflection R is the ratio of the intensity of the radiation leak from the macroscopic surface $J_{(x=0)}$ or $I_{(r)}$ (reflected) and the intensity of the incident radiation $I_{(x=0)}$ or $I_{(i)}$ (incident).

$$R = \frac{J_{(x=0)}}{I_{(x=0)}} = \frac{I_{(r)}}{I_{(i)}} \quad \text{Eq. 2-4}$$

In the case of a very thin layer (thicknesses d) transmission T occurs defined as:

$$T = \frac{I_{(x=d)}}{I_{(x=0)}} \quad \text{Eq. 2-5}$$

The general solution of the differential equations 2-2 and 2-3 in hyperbolic form originates from Kubelka [15]. The reflectivity of the layer with a non-reflective background with the thickness of d is given in equation 2-6 [14]

$$R_d = \frac{1}{a + b \cdot ctgh(b \cdot S \cdot d)} = \frac{\sinh(b \cdot S \cdot d)}{a \cdot \sinh(b \cdot S \cdot d) + b \cosh(b \cdot S \cdot d)} \quad \text{Eq. 2-6}$$

whereas:

$$a = \frac{K + S}{S} \quad \text{and} \quad b = \sqrt{(a^2 - 1)}$$

Since $ctgh(b \cdot S \cdot d) = 1$ in the case of $d \rightarrow \infty$, the reflectivity of the infinite layer can be written in the following equation:

$$R_\infty = \frac{1}{a + b} = \frac{S}{S + K + \sqrt{K(K + 2S)}} \quad \text{Eq. 2-7}$$

S and K are related to the linear absorption coefficient k, the linear scattering coefficient s and the scattering anisotropy factor g. The original

Kubelka-Munk theory puts K equal to $2k$ and S equal to $2s$. R. Molenaar and co-workers [16] reported and referred to more recent publications that better agreement with experiment is achieved when the following definition of S is used

$$S = \frac{3s(1-g) - k}{4} \quad \text{Eq. 2-8}$$

with the boundary condition: $k < 3s(1-g)$.

The Kubelka-Munk absorption coefficient differs from 0, if

1. the sample absorbs strongly,
2. the ideal "white" material is mixed with an absorbing material,
3. there are absorbing surface species on the particle.

Reconstruction of the equation 2-6 leads to the Kubelka-Munk unit, $f(R_\infty)$, which gives a linear relationship between the concentration of the adsorbed species and the band intensities (similar to the Law of Lambert - Beer $E = \varepsilon \cdot c \cdot d$)

$$f(R_\infty) = \frac{(1 - R_\infty)^2}{2R_\infty} = \frac{K}{S} = \text{cons.} \cdot c \quad \text{Eq. 2-9}$$

It is supposed that the scattering coefficient S is independent of small concentration of adsorbed species, since the scattering coefficient S only depends on the matrix (here SnO_2).

It should be noted that both the Kubelka-Munk absorption and scattering coefficients (K and S) depend on the wavelength and are valid only for monochromatic radiation. It is not totally correct to compare the intensity of the species in Kubelka-Munk units absorbed at different wavelengths like in the case of Lambert-Beer-Extinction.

2.6 Specular Reflectance

In real life, diffuse reflectance and specular reflectance always occur together. The reflectance is called specular, when the angle of the outgoing

light is equal to the angle of the incident light on the surface interface. The direction and the intensity ratio of the incident light to reflected light can be calculated with the Fresnel Equation [14]:

$$R_{spec} = \frac{1}{2} \left[\left(\frac{\sqrt{n^2 - \sin^2 \Theta} - \cos \Theta}{\sqrt{n^2 - \sin^2 \Theta} + \cos \Theta} \right)^2 + \left(\frac{n^2 \cos \Theta - \sqrt{n^2 - \sin^2 \Theta}}{n^2 \cos \Theta + \sqrt{n^2 - \sin^2 \Theta}} \right)^2 \right] \quad \text{Eq. 2-10}$$

n : ratio of the refraction index of the sample to that of the surrounding medium, Θ : angle of the incident light.

In the case of illumination perpendicular to the surface from vacuum into a non-absorbing material, the equation is simplified as follows:

$$R_{spec} = \frac{(n-1)^2}{(n+1)^2} \quad \text{Eq. 2-11}$$

In the case of absorbing materials (which is the case in this work) a complex refraction index must be used instead of the real refraction index.

$$\tilde{n} = n(1 - i \cdot \kappa) = n - i \cdot k \quad \text{and} \quad k = n \cdot \kappa \quad \text{Eq. 2-12}$$

κ = absorption index

k = absorption coefficient

Taking the reflected light by the absorption into account the amplitude of the specular reflectance follows from the *equation 2-13*:

$$R_{spec} = \frac{[(n-1)^2 + k^2]}{[(n+1)^2 + k^2]} \quad \text{Eq. 2-13}$$

A comparison of the equations for non-absorbing and absorbing materials (equations 2-11 and 2-13) show that the intensity of the specular reflectance is higher for the absorbing material than for the non-absorbing material and the intensity of the diffuse reflectance is lower (equation 2-7).

2.6.1 Methods for Minimizing Specular Reflectance

Additional to the conditions needed for the Kubelka-Munk theory (planar, homogenous sample etc.) there are some tricks which help to reduce the specular reflectance.

The particle size should be smaller than the wavelength of the IR radiation (1-50 μm). In the case of larger particle size, a lot of inordinately orientated small mirroring surfaces are present, which cause specular and specular-diffuse reflectance.

Glauninger [17] performed a systematic study on silica gel plates to reduce or eliminate specular reflectance. The following experiments were performed:

- 1 Coating of the plates with KBr: In this experiment, KBr solution was sprayed on the silica gel plate, which is etherified with long chain alkanes, in order to reduce the differences between the refractive indexes. It has been shown that very thin layers of the KBr do not influence the specular reflection and in the case of very thick layers the KBr spectrum is dominant. With the layer thickness of 0.25 mm the optimum of the diffuse reflectance was obtained
- 2 Adjustment of the height of the sample surface: The complete optical geometry of the light pathway is changed through changes of the sample position in height. This vertical displacement changes the angle of incident and reflected IR radiation, so that a different type of reflection can be detected. Mostly, the adjustment of the diffuse reflection is done on the basis of an adjustment of the reflection unit, until getting maximum intensity of the signal. This leads to difficulties in the case of absorbing materials, because therewith the specular reflectance is also collected.

Both the experiments performed by Glauninger et al. and experiments conducted for this research shows how the intensity of the diffuse and specular reflectance changes at different incident angle of the IR radiation.

2.7 Diffuse Reflectance on Absorptive Materials

One of the conditions of the Kubelka-Munk theory is that the sample must be only weakly absorbent. In order to fulfil this assumption absorptive samples are diluted with a non-absorptive material such as alkali halides.

The influence of the refractive index on the spectra must be considered in the reflection spectroscopy of strong absorptive samples. In the case of samples with a strong absorption band, one obtains an anomalous dispersion curve. This indicates that the refractive index is depending on the wave length, at the position of absorption (see Figure 2.5). One obtains a very high value for the refractive index at the position of the absorption, which affects the consistence of the reflected radiation. As can be gathered from the equation (Eq. 2-13) for the specular reflectance - in the case of a perpendicular incident angle and reflection at interface to vacuum - the specular reflectance approaches 1, at high values of $k = n \cdot \kappa$.

$$R_{spec} = \frac{[(n-1)^2 + k^2]}{[(n+1)^2 + k^2]} \quad \text{Eq. 2-13}$$

This means, at the position of a strong absorption, the incident radiation is reflected almost 100% as unwanted specular reflectance. Thereby, it appears as a reflection maximum, so called "Reststrahlen", instead of a reflection minimum.

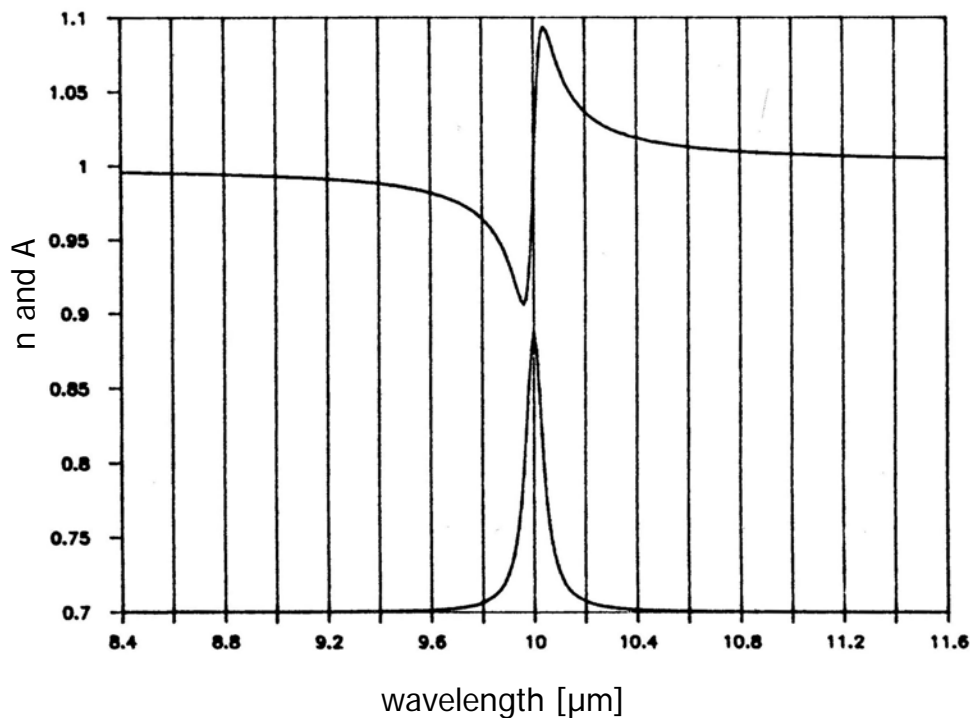


Figure 2.5: Dependence of the refractive index (n) and absorption coefficient (A) on the wavelength.

2.8 Adsorption Processes on Solid Surfaces.

The interaction between gases and solid surfaces is a basic process, providing an understanding of the working principle of gas sensors. The adsorption of different gases depends on the surface structure composition and gas molecules. The adsorption can take place in different ways. In the following different types of adsorption are roughly described.

2.8.1 Physisorption

In the case of physisorption both the geometrical structure and the electronic structure of the particle and the surface do not change. There is a weak interaction described by van-der-Waals forces between adsorbate and surface. The potential of the interacting particles can be approximated by a two particle potential, which includes an attraction term and a repulsive term. Attraction of the particles is due to electrostatic effects.

The Lennards-Jones Potential describes this two-particle potential.

$$E_{pot} = E_{attr.} + E_{rep} \propto 4\varepsilon \left[-\left(\frac{d}{r}\right)^6 + \left(\frac{d}{r}\right)^{12} \right] \quad \text{Eq. 2-14}$$

Where, d : distance between the interacting particles and ε : depth of potential.

In the case of chemisorption and ionosorption the strength of bonding between adsorbate and surface is stronger.

2.8.2 Hydrogen Bonding

When a covalently bound hydrogen atom forms a second bond to another atom, the second bond is referred to as a hydrogen bond. The hydrogen bond is usually presented as $A-H \cdots B$ where B is any σ or π electron donor site (Lewis base) and A is an atom with electronegativity greater than that of hydrogen (C, N, P, O, S, F, Cl, Br). The bond can be asymmetrical, so that the proton more strongly bound to one atom than to another, or it can be symmetrical where the proton can tunnel between the two equilibrium positions.

The intermolecular force of hydrogen bonds is composed of a van-der-Waals term and a covalent part. The magnitude of the force of this type of bond is between physisorption and chemisorption (~ 0.1 eV). The potential energy of this type of bond can be described with a function similar to the Lennard-Jones potential (Figure 2.6). The difference to the physisorption is the power of the repulsive term.

$$E_{pot} = E_{attr.} + E_{rep} \propto 4\varepsilon \left[-\left(\frac{d}{r}\right)^6 + \left(\frac{d}{r}\right)^9 \right] \quad \text{Eq. 2-15}$$

2.8.3 Chemisorption

A strong interaction between adsorbate molecules and surface dominates in the case of chemisorption, which is much stronger than physisorption (>5 eV for H_2). Through the chemisorption of the molecules, the surface construction is changed due to the strong interaction with the adsorbates.

Chemisorption can take place molecularly or atomically. The latter one proceeds through the dissociation of the molecules on the surface. By the chemisorption on semiconductors, the oxidation or reduction states of the adsorbate molecules are adjusted. Also, chemisorption changes the electronic structure of the adsorbate and the surface, as a chemical bond is created, if the electrons are captured in the adsorption complex or they are transferred from the adsorption complexes into the conduction band of the semiconductors. The corresponding concentration changes of the free charges can be measured via changes in conductivity.

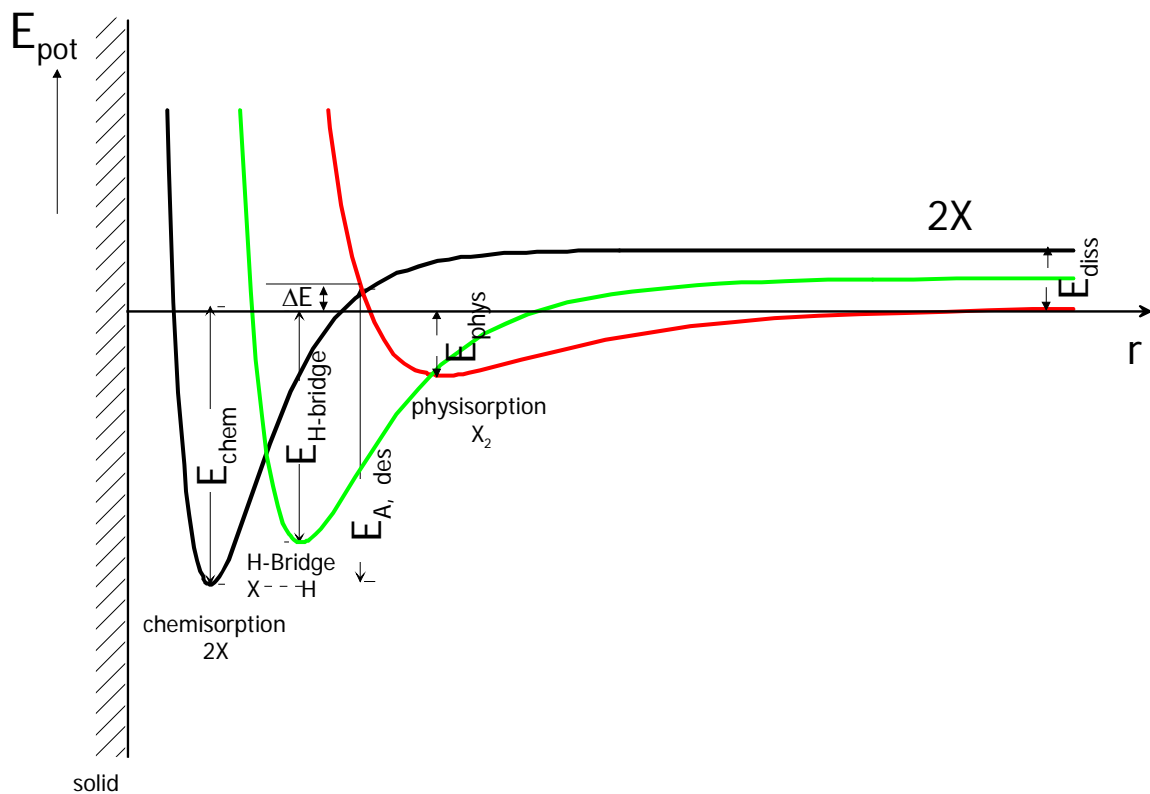


Figure 2.6: Potential diagram for chemisorption, hydrogen bonding and physisorption on the surface.

Figure 2.6 depicts the potential curves for physisorption, hydrogen bonding and chemisorption. As can be seen, the chemisorption takes place after physisorption, if the corresponding activation energy is applied. Usually this takes place through thermal activation. Therefore, physisorption is usually preferred at low temperatures.

2.8.4 Ionosorption

Ionosorption is a special type of chemisorption. By the ionosorption atoms or molecules are ionised through capturing of an electron from the bulk (conduction band) during the adsorption process. Therefore ionosorption can be seen as delocalised chemisorption.

As a consequence of the charge transfers between molecules and surface, the chemical reactivity of the molecules, as well as their electronic and geometrical structures, are strongly influenced.

2.9 Electronic Structure of Semiconductors

The electronic effect of the adsorption of different gases on the metal oxide surfaces can be described by the band model. The fundamental conduction model of metal oxide has been discussed in details in [18, 19]. In the following, the electronic structure of the semiconductor and changes of its band structure by adsorption processes will be described. For simplification, the influence of the adsorption processes on the electronic band structure will be shown on the basis of oxygen adsorption.

On the surface of solids, the periodicity of the structure is broken; thus, unsaturated sites are created called coordinatively unsaturated sites ("cus") or dangling bonds. With the building of these "cus" new energy levels are generated, which can act as a donor or acceptor. A surface charge is built up which leads to a space charged layer. This effect is particularly strong in the case of adsorption of oxidizing or reducing gases. As an example, oxygen adsorption will be illustrated: Oxygen detracts electrons from the bulk which causes a broadening of the depletion layer of the free charges in the n-type semiconductors near the surface. The broadness of this band bending can be calculated using the Schottky model. However, the oxygen adsorption is limited due to the band bending. The chemisorption cannot take place anymore, if the Fermi level of the bulk is equal to the energy of the highest occupied surface states. For the maximal coverage of the

surface with oxygen results of the Weisz limitation 10^{12} to 10^{13} molecules per cm^2 [20].

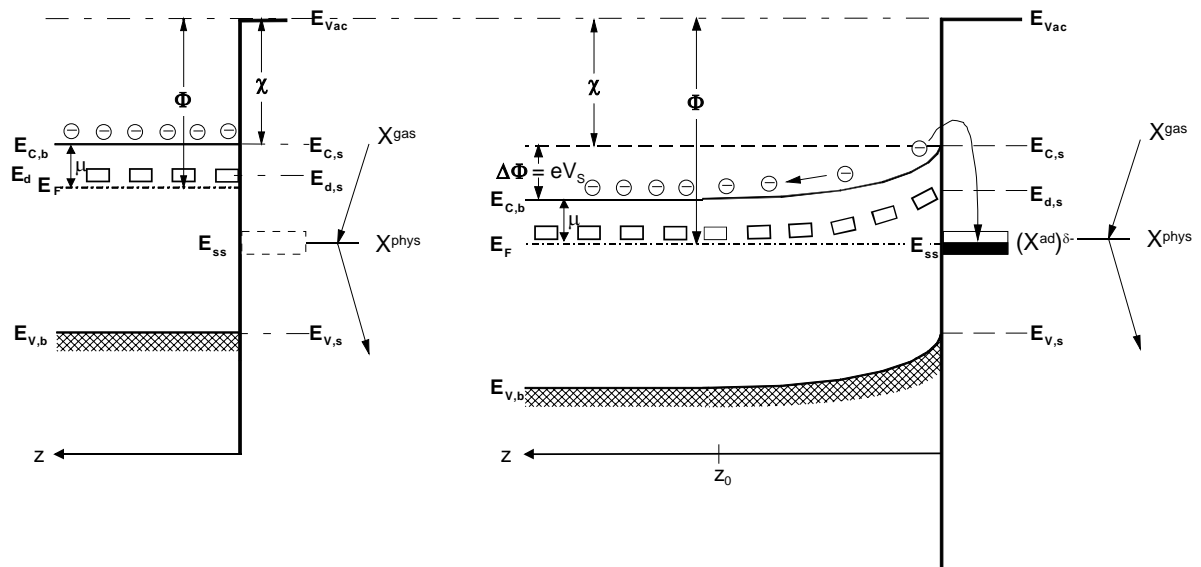


Figure 2.7: Electronic structure of semiconductor before and after gas adsorption on the surface. Band bending of a n-type semiconductor.

Initial point for the calculation of the Schottky barrier (potential barrier induced by the band bending) is the one dimensional Poisson equation:

$$\frac{\delta^2 \Phi}{\delta x^2} = \frac{e \cdot N_i}{\epsilon \cdot \epsilon_0} \quad \text{Eq. 2-16}$$

where,

Φ : electrical potential,

e : elementary charge,

N_i : number of ions in the space charge area,

ϵ : permittivity of the semiconductor

ϵ_0 : permittivity of free space (8.853×10^{-12} As/Vm)

Integrating the Poisson equation twice results with the substitution

$$V_{(x)} = \Phi_b - \Phi_x$$

where,

Φ_b : potential in bulk and

Φ_x : potential in the edge layer:

$$V(x) = \frac{e \cdot N_i \cdot (x - x_0)^2}{2 \cdot \epsilon \cdot \epsilon_0} \quad \text{Eq. 2-17}$$

From this follows directly the height of the Schottky barrier for $x=0$:

$$V_s = \frac{e \cdot N_i \cdot x_0^2}{2 \cdot \epsilon \cdot \epsilon_0} \quad \text{Eq. 2-18}$$

The number of charges N_s placed on the surface can be determined from the number of charge carriers which migrate from the region between $x=0$ and $x=x_0$ towards the surface:

$$N_i \cdot x_0 = N_s \quad \text{Eq. 2-19}$$

This leads to:

$$V_s = \frac{e \cdot N_s^2}{2 \cdot \epsilon \cdot \epsilon_0 \cdot N_i} \quad \text{Eq. 2-20}$$

The Schottky barrier V_s describes the potential between the surface and the inside of the semiconductors which electrons have to overcome during the free charge exchange. N_s describe the number of the free charges on the surface which is created due to adsorbed and charged molecules. The charge density in the conduction band (in the case of a n-type semiconductor) depends on the Fermi distribution or rather in the first approximation on the Boltzmann distribution which takes the height of the potential barrier into consideration. For the n type semiconductor is applied in the case of fully ionised donors:

$$n_s = N_C \exp\left(\frac{-(e \cdot V_s + E_C - E_F)}{k \cdot T}\right) = N_D \cdot \exp\left(\frac{-e \cdot V_s}{k \cdot T}\right) \quad \text{Eq. 2-21}$$

where:

- n_s : The density of the free charges on the surface
- N_C : The density of the free charges in the conduction band
- N_D : Ionised donor density
- E_F : Fermi energy
- E_C : Lower edge of conduction band energy

T : Temperature

k : Boltzmann constant

An expression for a free charge density on the surface can be obtained, when in equation 2-21 V_s is substituted the expression equation 2-20

$$n_s = N_D \cdot \exp\left(\frac{-e^2 \cdot N_s^2}{2 \cdot \varepsilon \cdot \varepsilon_0 \cdot k \cdot T \cdot N_i}\right) \quad \text{Eq. 2-22}$$

2.10 IR Characterisation of Metal Oxide Surfaces

Due to the defects in the crystalline structure in the surface layer of metal oxides, the surface structure differs from the bulk structure. The presence of surface vacancies leads to forces on atoms in the surface layer that are different from those on atoms in the bulk. Therefore, additional absorption bands corresponding to the metal-oxygen vibrations on the surface layer appear in the spectrum, since the frequency of the IR bands in the spectrum is proportional to the square root of the force constant.

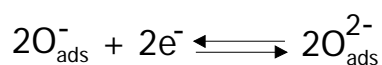
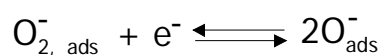
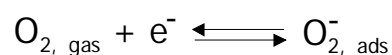
Table 1: Literature overview of metal-oxygen vibration modes of different metal oxides in and above the fundamental spectral region.

Metal oxide	Fundamental frequencies [cm ⁻¹]	Region above fundamental frequencies [cm ⁻¹]	Reference
Cr ₂ O ₃	407, 435, 550, 625	820, 890, 980, 995, 1015	[23]
TiO ₂	347, 525-700	730, 770, 870, 950	
SnO ₂	610, 670	970, 1060	[21, 24]
Co ₂ O ₃	560, 665	800-1200	
V ₂ O ₅	600, 800 (broad)	1000-1020	[25, 26]
WO ₃	330	600-950	[27]
		1100-800	[28]

The vibration frequencies of the metal oxygen bond on different metal oxides are described, discussed extensively and summarized in [21, 22] and

references therein. Table 1 shows a small overview and gives frequencies of metal-oxygen bonds detected by different IR experiments.

The fundamental frequency is defined as the frequency of the metal-oxygen bond in the bulk. The metal-oxygen vibration in the bulk appears in the IR spectrum mostly between 200 and 800 cm^{-1} . The metal-oxygen vibration in the surface lattice differs from that in the bulk and appears usually at higher wavenumbers. The formation of metal-oxygen groups of an ionic nature on oxide surfaces [21 and references therein] is equivalent to oxygen ions adsorbed on metallic cations. Ions of this type can form on surfaces of oxide semiconductors as a result of the transfer of oxide electrons to the adsorbed oxygen:



These oxygen species belong to the surface lattice and their frequencies differ from those of M-O bonds in the bulk, because the surface O^{2-} is bound to a lower number of metal atoms on the surface. Accordingly, the bond between the metal cations and O^{2-} anion is stronger, which causes the higher frequency of this band in the IR spectrum. In the literature in this spectral region, called "region above fundamental frequencies", several band maxima assigned to metal-oxygen vibrations were observed. The reason for this is the different faces and fractures in various planes of the lattice of real polycrystalline samples, where the surface metal cation has different coordinative saturation values (with respect to oxygen). Accordingly, the strengths of the oxygen bonds differ from each other. The coordination number of the metal atom influences the frequency of the vibration. The lower the coordination number of the metal cation at

constant valency, the smaller are the interatomic distances, which causes an increase in bond multiplicity.

The spectroscopic features of the metal-oxygen bonds at the surface are summarized in [23]. Metal-oxygen bonds present following individual features:

- a. Bands are restored by high temperature oxidation treatment
- b. Bands disappear or shift on adsorption of other molecules
- c. Isotopic exchange by exposing to O^{18} leads to band shifting
- d. On reacting gases with hydrogen and carbon monoxide the bands disappear, due to the creation of surface hydroxyl and carbonate groups, respectively.

Although isotopic exchange experiments with O^{18} were performed neither on powder nor on sensors, other features of the surface metal-oxygen bonds listed above were observed in the measurements conducted on SnO_2 powder and sensors in this work.

The role of all individual surface oxygen species in the sensing mechanism of tin dioxide sensor is not clear. The influence of different oxygen atoms (bulk, bridging, in-plane oxygen) on the conduction was studied theoretically and experimentally by different authors [29, 30]. Investigations on SnO_2 using UPS (Ultraviolet Photoelectron Spectroscopy) and ISS (Ion Scattering Spectroscopy) showed that removal of the oxygen atoms in the bridging position leads to the creation of energy levels near the valence band. These levels are too deep to be ionised even at high temperatures and therefore they do not have any influence on the conductance. This result is confirmed by the theoretical study by Rantala et al. [29]. However, the same spectroscopic measurements showed that the removal of the in-plane oxygen causes the creation of energy levels which are located slightly below the conduction band and thus would contribute to the conduction. However, a theoretical calculation was not reported in the literature for this case. The reactivity and the role of different oxygen

species in the sensing mechanism will be discussed in detail in chapters 2.13 and 4.1.4.

2.11 Adsorption Mechanism of Selected Molecules on MOX Surfaces

Up to now a large number of studies were attempted using different methods to understand the adsorption mechanism of different gases on metal oxide surfaces. In the following an overview of relevant IR studies for the adsorption of oxygen, water and CO onto the surface of gas sensitive layers will be presented and discussed. The focus is on the adsorption behaviour as a function of temperature. The vibrational frequencies of the surface species are summarised in Figure 2.8, Figure 2.16 and Figure 2.19.

2.11.1 Oxygen Adsorption

It has been reported several times that the interaction of oxygen with the sensitive layer plays a central role in gas sensing and catalysis due to its reactivity. On the metal oxide surfaces, various oxygen species were characterized by several different methods e.g. IR (Infrared), TPD (Temperature Programmed Desorption), EPR (Electron Paramagnetic Resonance) etc.

Results obtained by TPD, IR, EPR have shown the form of the different oxygen species on the surface as a function of temperature.

Figure 2.8 [9, references therein] depicts the adsorption of the oxygen species as a function of temperature obtained by IR, TPD and EPR experiments.

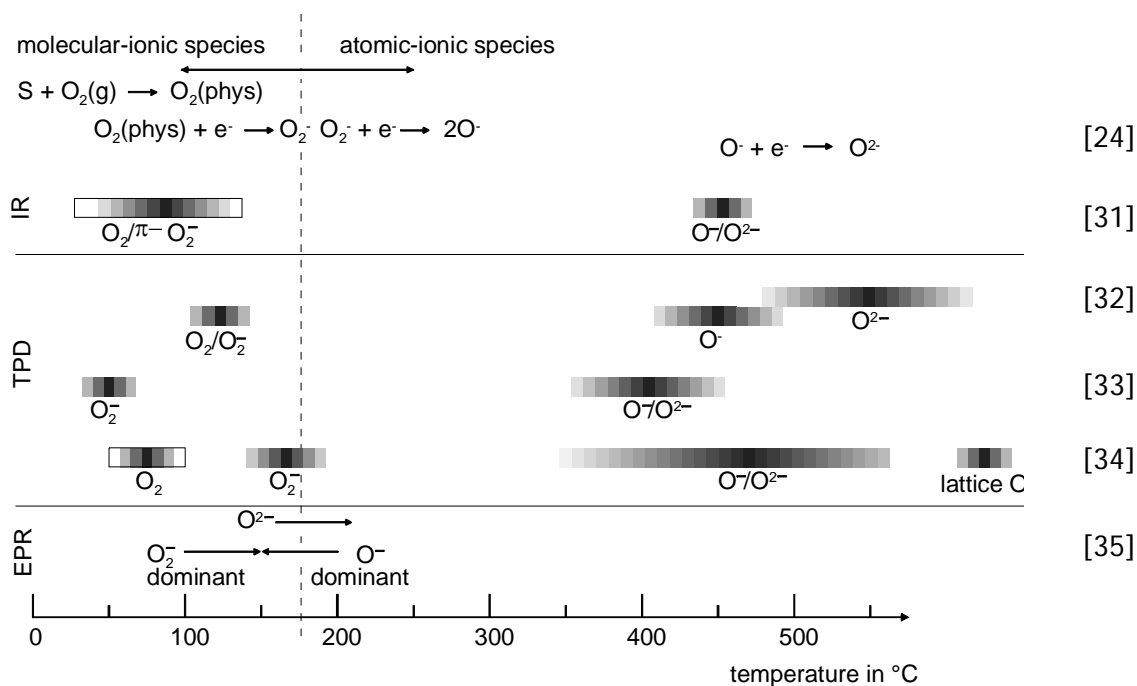


Figure 2.8: Oxygen species detected at different temperature on tin oxide surfaces with IR (infrared analysis), TPD (temperature programmed desorption), EPR (electron paramagnetic resonance).

By these investigations it was found, depending on the temperature (pre-treatment), that oxygen adsorbs on the surface in several forms like O_2 , O_2^- , O^- , O^{2-} . According to investigations, molecular species (O_2^-) are present on the surface below 200°C and above this temperature the atomic species in form of O^- and O^{2-} are present. Especially several oxygen experiments with isotopic exchange of $^{16}\text{O}/^{18}\text{O}$ helped to characterize the ν_{O-O} vibration modes of O_2^- and M-O. For the characterization of the molecular radical form of oxygen (O_2^-) additional to IR measurements EPR measurements were carried out. However, systematic experiments for the full characterisation of adsorbed oxygen species (O_2^- in radical form) by isotopic exchange experiments on different metal oxides are rare in the literature. For example, oxygen related species on SnO_2 were extensively examined only by Davydov et al. [36], Lenarts et al. [37], Zecchina et al. [23, 38], Harrison et al. [39], although SnO_2 is one of the most widely investigated materials by infrared spectroscopy.

Molecular charged oxygen (O_2^-) is found on the metal oxide surface at low temperatures after the exposure of oxygen to the surface of oxide catalysts using IR spectroscopy [21, 36, 38 and references therein]. The O_2^- molecules are stable up to 200°C. Figure 2.9 shows the molecular energy diagram of the oxygen molecule and the interactions between the d orbital of the metal and the p orbital of the oxygen molecule.

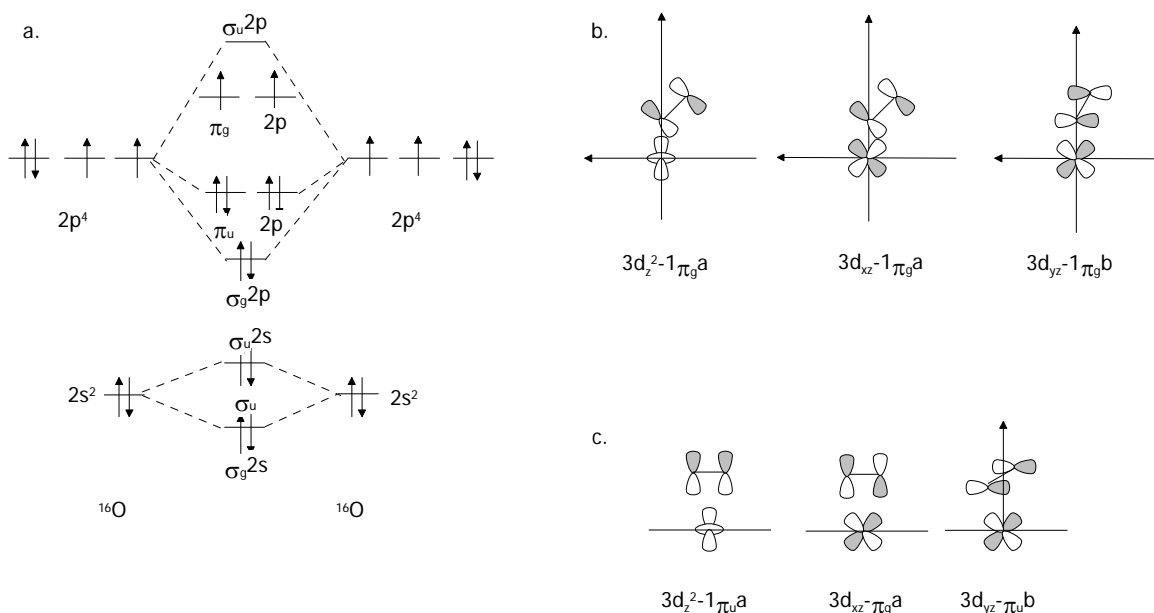


Figure 2.9: a. The molecular energy diagram for O_2 . b. Interaction of molecular oxygen with the d orbitals of the metal cation for bent structures c. Interaction of molecular oxygen with the d orbitals of the metal cation for side-on structures

Table 2 shows the selected oxygen species of type O_2^- and their vibration frequencies on metal oxide surfaces detected by IR spectroscopy. As it can be seen from Table 2 the frequency of the vibration depends on the pre-treatment of the materials.

Table 2: Different oxygen species detected on different metal oxide surfaces by infrared transmission measurements at various temperatures following different pre-treatments.

Metal oxide	Pre-treatments	Species	ν [cm^{-1}]	Reference
Cr_2O_3	Evacuated at RT/ O ₂ exposure CO exp. At 673 K/O ₂ exp.	O ₂ ⁻ (radical)	985	[22]
		M=O	1000	
TiO_2	Pre-treated in reduction condition	O ₂ ⁻ (radical)	1060-1180	[21]
SnO_2	Heated in vacuum, then reduction of the surface, finally O ₂ adsorption	O ₂ ⁻ (radical)	1045, 1190	[21, 36]
	Heated in O ₂ atm., then reduction of the surface, finally O ₂ adsorption	O ₂ ⁻ (radical)	1140, 1120, 1100, 1090	[21, 36]
	O ₂ /N ₂ exposure, at RT	Different oxygen species, no concrete assignment	1370, 1266, 1140, 1068, 1020, 970, 930, 885	[24, 37]
CeO_2	At 1000 K heated	Super oxide O ₂ ⁻	1126	[40]
	At 673 K heated in H ₂ atm	Super oxide O ₂ ⁻ Peroxide	1128 883	
Co_2O_3	At 77 K		1162, 1152, 1132, 1098, 1090	[38]
	At 293 K		1132, 1012	
NiO	Reduced oxide surface	O ₂ ⁻	1070	[22]

With the help of combined methods, e.g. IR with EPR run after different pre-treatments it was possible to depict the form of molecular oxygen on the surface. Giamello et al. [38] reported that the interaction or coupling of the O_2^- ions with different hydroxyl groups depends on the pre-treatment (dehydroxylation) temperatures. The authors observed a shifting of the IR bands corresponding to the surface hydroxyl groups and changing of the band intensity and structure in the ν_{O-O} spectral region with pre-treatments of increasing temperature

Figure 2.10 depicts the different O_2^- molecules adsorbed on the surface.

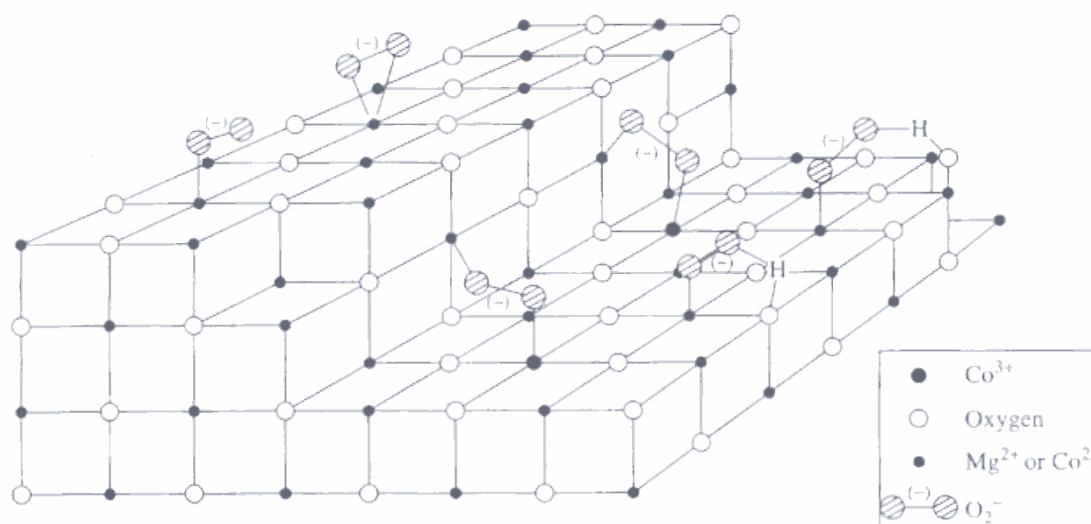


Figure 2.10: Different adsorbed molecular oxygen ions (O_2^-) and their interaction with other surface species on Co_2O_3 oxide surface [38].

The reactivity of the different oxygen species (mononuclear and molecular oxygen species) was examined by several methods, e.g. EPR [41, 42], IR [36]. According to these reactivity experiments, the reactivity of the molecular form of oxygen depends on the metal oxide, analyte gas and measurement conditions. For example, reactions with CO or alkanes were observed only at RT and not at very low temperatures on MgO. At RT, a reaction between molecular oxygen on ZnO surfaces and propylene and no reactions with CO, H_2 , and ethylene were observed.

In this work, absorption bands appearing in the spectral range between 1200 and 850 cm^{-1} were determined on the basis of two experiments: 1) different dependence of band intensities on CO content in the time resolved spectra; 2) the evolution of the absorption bands during temperature cycles (RT-350°C, see chapter 4.1.3). Additional experiments such as D₂O and ¹⁶O/¹⁸O (for the characterisation of the hydroxyl groups, surface metal-oxygen and O₂⁻ species, respectively) exposure to sensors at working conditions are recommended to check the assignments.

2.11.2 Water Adsorption

Since water occurs as an interfering gas in the application of gas sensors, the sensor surface interaction with water is of great interest.

Infrared spectroscopy is a powerful method for the detection of water related species. IR data for adsorption of molecules and their chemical properties are summarized in several books and reviews [21]. The adsorption of water generates three types of hydroxyl groups on the metal oxide surfaces;

- Chemisorbed terminal hydroxyl groups (M-OH),
- Chemisorbed rooted hydroxyl groups which include the lattice oxygen (O_{lat}-H),
- Hydrogen bridged hydroxyl groups (associated hydroxyl groups).

The vibrations of the terminal and rooted hydroxyl groups appear in the IR spectra as discrete absorption bands. A hydrogen bond leads to broadening and shifting of the absorption bands assigned to terminal hydroxyl groups to lower wavenumbers in the IR spectra.

On most metal oxide surfaces, several absorption bands with different full width at half maximum (fwhm) corresponding to hydroxyl groups were detected. A reason for the appearance of several bands due to surface hydroxyl groups is the local surrounding structure of these groups and their chemical nature.

In the literature, the denotation of the hydroxyl group of form M-OH is not unique; isolated, free, terminal etc. were used for this groups. In this work, terminal hydroxyl groups are used for the M-OH groups (Figure 2.13). The word "isolated" expresses that there is no interaction with the neighbouring surface molecules. Accordingly, rooted OH groups are isolated as well.

The sol-gel prepared SnO₂ surface was extensively investigated by Harrison and Guest [43] using infrared spectroscopy (transmission measurements) and X-Ray measurements. The authors reported that the crystalline tin (IV) oxide exhibits (110), (101) and (100) planes in the ratio 3:1:1. In the case of the totally hydroxylated (110) plane, two types of hydroxyl groups exist on the surface, unidentate hydroxyl groups whose Sn-O bond axis is orthogonal to the plane (in this work they are defined as terminal OH-groups) and geminal pairs of hydroxyl groups (Figure 2.11).

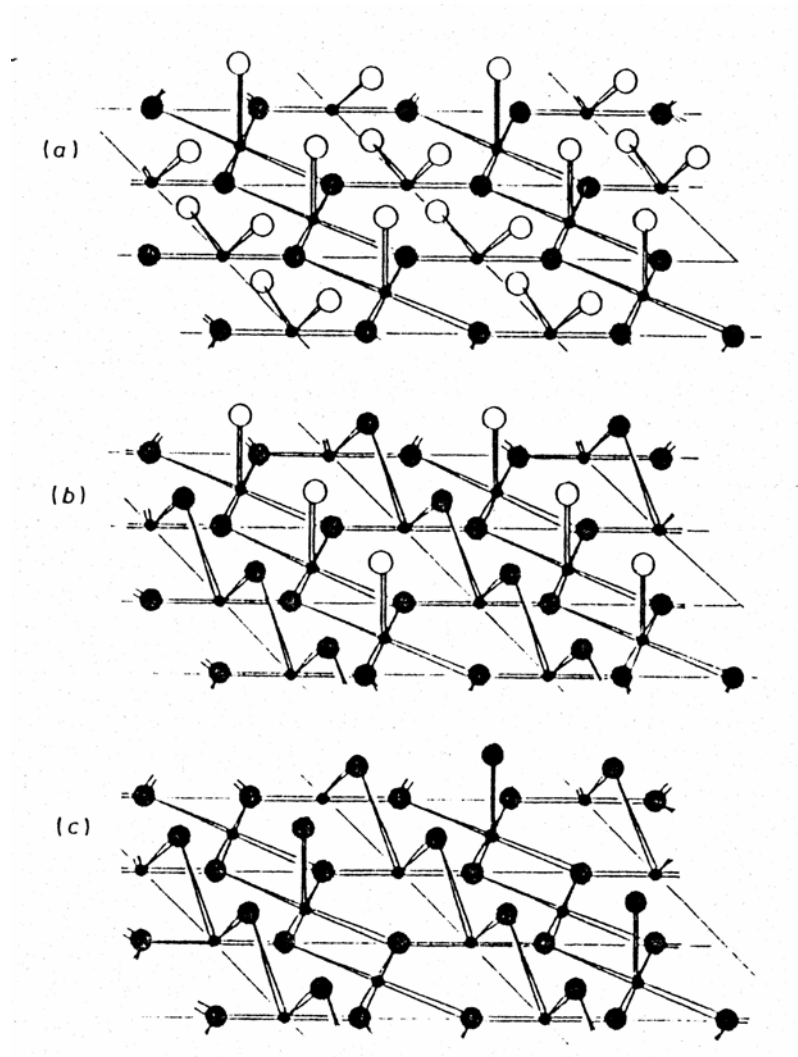


Figure 2.11: (110) plane of the rutile structure of SnO₂ surface. (a) totally hydroxylated surface, (b) partially dehydrated surface, (c) totally dehydrated surface. Surface hydroxyl groups are shown as open circles, surface oxide atoms by shaded circles. Small shaded circles represent the surface tin atoms.

The totally hydroxylated (101) and (100) planes show similar surfaces, and comprise triple clusters of hydroxyl groups attached to each tin atom in the surface (in Figure 2.12 (100) plane of SnO₂ surface). The degree of surface hydroxylation will be increased if a large number of edges and corners are present on the surface.

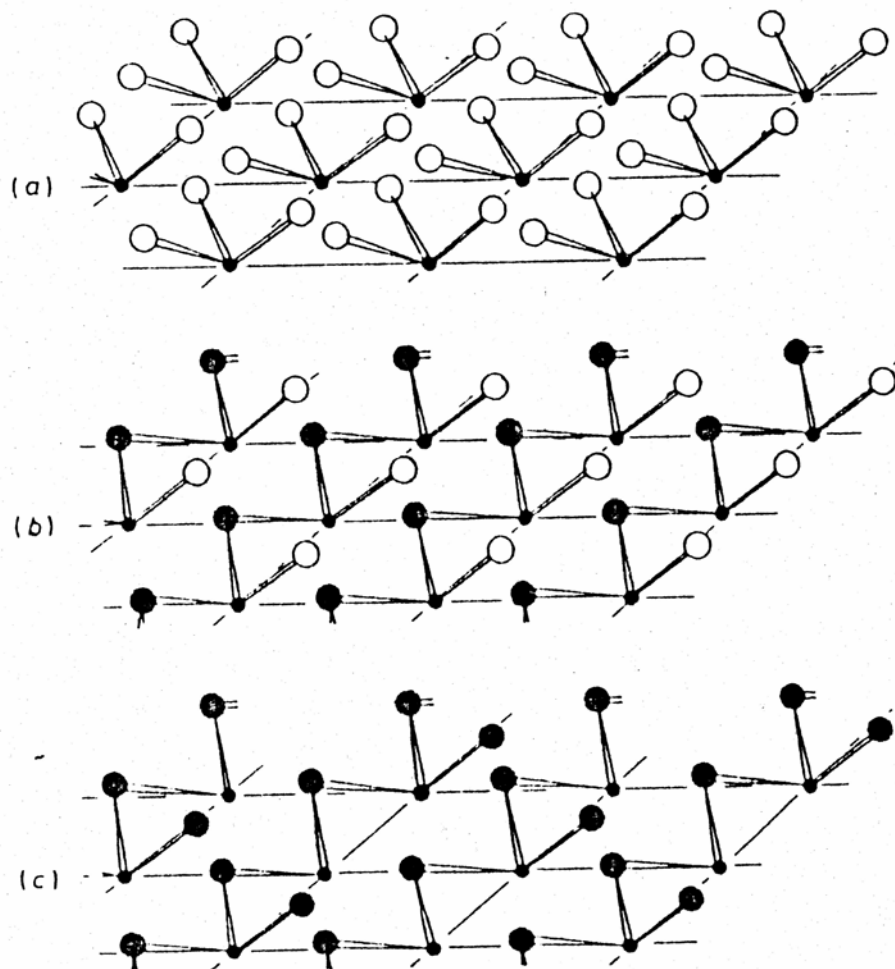


Figure 2.12: (100) plane of the rutile structure of SnO₂ surface. (a) totally hydroxylated surface, (b) partially dehydrated surface, (c) totally dehydrated surface. Surface hydroxyl groups are shown as open circles, surface oxide atoms by shaded circles. Small shaded circles represent the surface tin atoms

In some metal oxides it was found that the oxygen atom of the hydroxyl group interacts with a number of immediate neighbouring metal atoms, which causes different vibration frequencies. Figure 2.13 shows different hydroxyl groups.

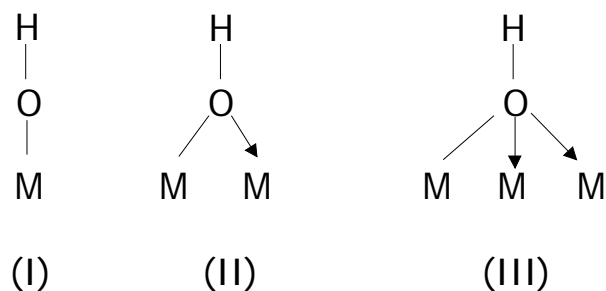


Figure 2.13: Schematical picture of different hydroxyl groups.

The nature of the surface terminal bound hydroxyl groups on metal oxide surfaces were studied by several authors [44, 45, 46, 47]. One of the goals of these studies was to find a correlation between the spectral features of hydroxyl groups and the crystallochemical properties of the oxides.

A systematic study and a review on Al_2O_3 is given by Tsyganenko et al. [46 and references therein]. Accordingly, the total number of the hydroxyl group types depends on the number of surrounding metal atoms, which is the cause for the different frequencies of the bands in the spectra. The formation of a coordination bond decreases the frequency of the stretching vibration. Of course, different pre-treatments of the sample cause the appearance of the additional absorption bands which can be assigned to hydrogen bonds between adjacent hydroxyl groups, for example, if the temperature of pre-evacuation is not so high or in the case of different coordination of surface aluminum ions. On the different modifications of alumina (γ , η , χ , θ) more discrete bands (up to nine) were obtained. Such heterogeneity can be explained, for example, by the presence of a surface cation vacancy, the presence of edges and corners on the surface.

Figure 2.14 is presenting the role of the edges and corners for the hydroxyl structures. An un-dissociated water molecule can adsorb on the edge of an already hydroxylated surface, when this is cleaved (Figure 2.14a). Attachment of the H and OH groups on the edge metal atom leads to creation of geminal hydroxyl groups (b). Since the proton affinity of such a hydroxyl type (b) would not be high, in case the water dissociation is energetically favourable, the proton could be trapped in the cation vacancy (c). The degree of surface hydroxylation will increase if a large number of edges and corners are present on the surface.

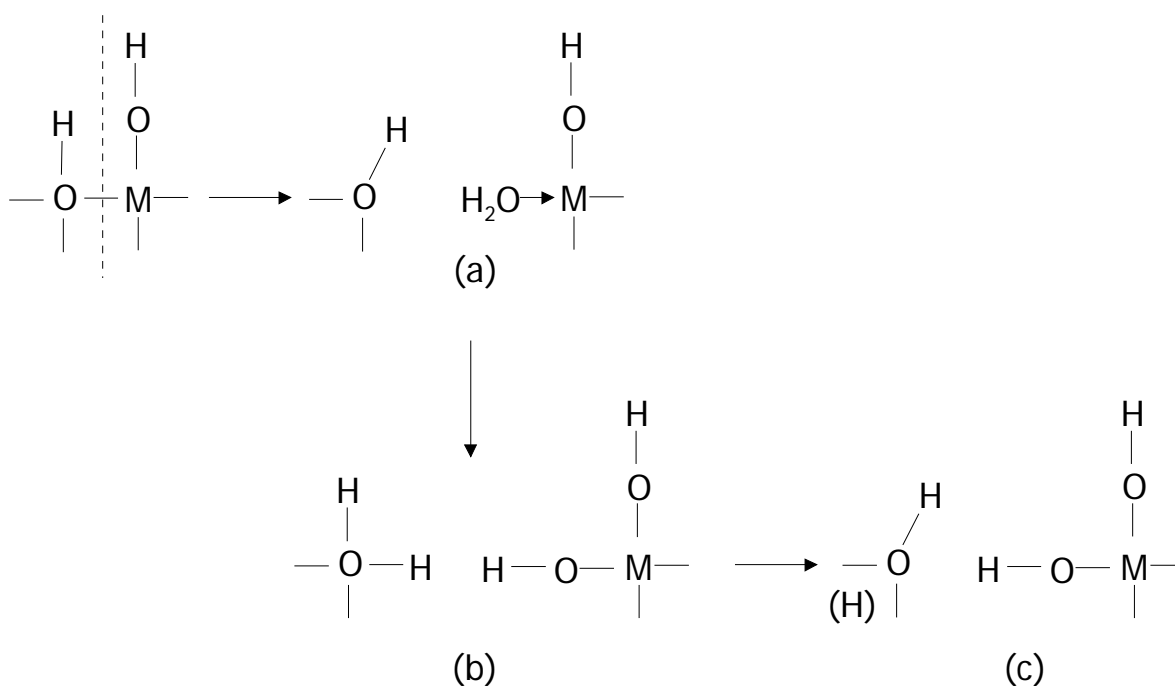
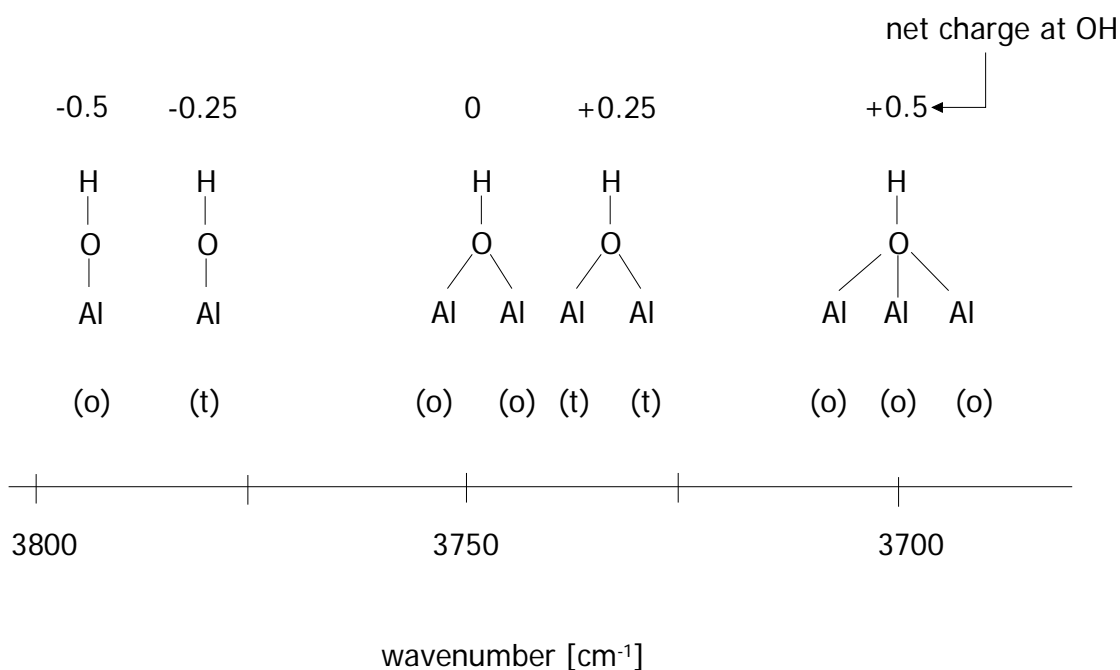


Figure 2.14: The role of edges and corners on the hydroxyl groups structures on the surfaces

It must be noticed that the presence of edges and corners influences the creation of the hydrogen bond and the reactivity of the surface species. For example, the proximity of the hydroxyl groups in the geminal pairs would facilitate extensive hydrogen bonds, which appear in the infrared spectra as a broad band.

Zaki and Knözinger studied the chemical nature of the surface hydroxyl groups on Al_2O_3 [45, 47]. The authors were able to distinguish acidic and basic hydroxyl groups by employing CO as an adsorbate on the basis of a model calculation proposed by [45]. Depending on the coordination of the surface cation (Al^{3+} octahedral or tetrahedral) and the anion (O^{2-} , terminal or bridging) the authors were able to calculate net charges, which give the acidity of the hydroxyl groups. According to this study OH groups with higher coordination number are more acidic (higher positive net charges, low frequency). The results of this model are shown in Figure 2.15.



(o): octahedral configuration

(t): tetrahedral coordination

Figure 2.15: Correlation of the vibrational frequency of the hydroxyl groups with the net charge and coordination of the Al_3^+ and O_2^- ions [48].

Another example for the acidic/basic nature of hydroxyl groups is the formation of ammonium ions on zeolites in which the most acidic group, characterised by the frequency in the $3620-3650\text{ cm}^{-1}$ region [21], is involved. Chemical properties of the surface species from the acidic/base point of view play a role in the interaction with the exposed gases.

Table 3 gives an overview of the stretching vibration modes of the hydroxyl groups detected on different metal oxides using infrared spectroscopy.

Adsorption Mechanism of Selected Molecules on MOX Surfaces

Table 3: Frequencies of hydroxyl groups detected on different metal oxide surfaces.

Metal oxide	Pre-treatments	$\nu_{(\text{OH})}$ [cm^{-1}]	Reference
Cr_2O_3		3720	[22]
TiO_2 [mainly anatase]		3717, 3693, 3668, 3640	[49, 51, 52, 53, 54] [55]
TiO_2 (rutile)		3685, 3655, 3410	[53]
SnO_2	Dehydrated at 350°C under vacuum	(3729), 3655, 3636, 3603, 3555, 3522, 3480	[5, 56, 57, 58,]
CeO_2		3689, 3664, 3600, 3517	[52]
CoO		3673, 3651	[59]
NiO		3735, 3680, 3630	
ZnO	RT 300°C 400°C 450°C	3677, 3657, 3638, 3620, 3556, 3443 3670, 3638, 3620, 3567, 3561, 3443 3690, 3624, 3595, 3577 3624	[50]
Ga_2O_3		3720, 3653, 3476	[60]
ZrO_2 (monoclin+triclin)	Activation at 400°C in O_2 atm., than evacuated at 300°C and cooled to RT.	3776, 3740, 3679, (3668)	[51]

On SnO₂ using TPD and IR transmission measurements it was found that the interaction with water vapour results in molecular water adsorbed as physisorbed or hydrogen bonded and as hydroxyl groups, depending on the temperature (see Figure 2.16). According to these studies, above 200°C no molecular water is present on the surface, whereas OH groups were still detected above 400°C (IR measurements).

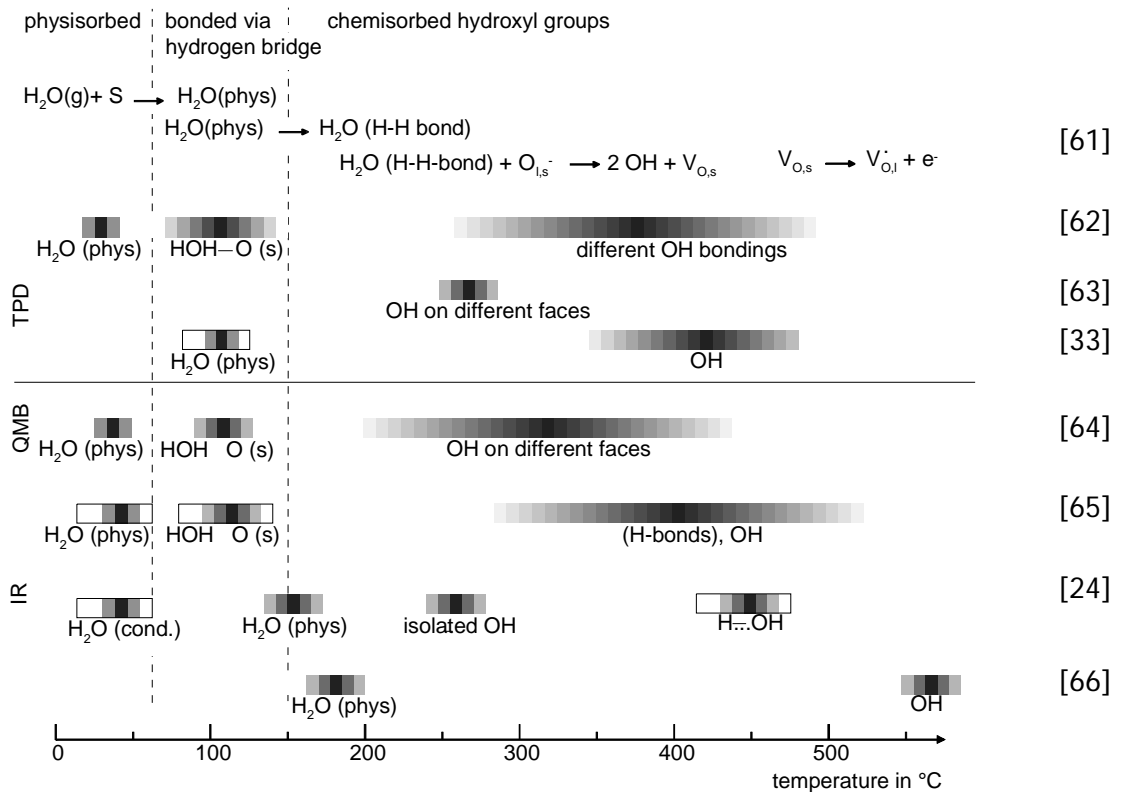
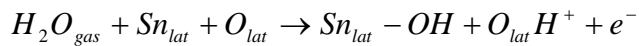


Figure 2.16: Overview of water related species detected by IR and TPD methods at various temperatures on SnO₂ surfaces.

However, the adsorption mechanism of water and the position of the hydroxyl groups are still unclear. By electrical measurements a reversible increase of the surface conductance in the presence of water was observed. The increase of the conductance is not affected by the molecular water but by the disappearance of hydroxyl groups. These findings lead to the assumption that the conduction could be related to the presence of hydroxyl groups [20]. Several mechanisms have been suggested to explain water adsorption. Heiland and Kohl proposed two direct mechanisms [20]. The

first mechanism attributes the role of electron donors to the "rooted" hydroxyl group, which include the lattice oxygen according to:



The second possible reaction takes place between the proton and the lattice oxygen forming hydroxyl groups bonded to tin atoms. The resulting oxygen vacancy produced additional electrons by ionisation:



Other authors [67, 68] proposed a reaction between chemisorbed oxygen and water resulting in two hydroxyl groups linked to tin atoms.

Another consideration is the interaction between H^+ and OH^- with an acid-base group. The co-adsorption of water with another adsorbate, which could be an electron acceptor, may change the electron affinity of the latter. Heinrich and Cox [69] suggested that pre-adsorbed oxygen could be displaced by water adsorption. In addition, others found hints for an influence of water vapour on oxygen chemisorption. They assume that water blocks the adsorption site for oxygen [70, 71, 72]. TPD and isotopic tracer studies showed a rearrangement of the oxygen adsorbates, due to water vapour, depending on the surface doping [62].

In this study, only the influence of water on the CO reaction mechanism is presented. In order to clarify the water adsorption on metal oxide surfaces, additional IR measurements at different temperatures are needed.

2.11.3 CO Adsorption

Up to now several studies were carried out in order to understand the reaction mechanism of CO adsorption. The adsorption mechanism depends on the measurements conditions, *e.g.* temperature. Infrared spectroscopy was used for identifying the CO related species and surface sites. The results showed that CO interacts with different surface sites and species, since CO can act both as acid and as base ($\delta^- |C \equiv O| \delta^+$), which allows it to react with both acidic sites of a surface, *e.g.* with metal cations acting as

Lewis acid adsorption sites and oxygen anions acting as Lewis / Brönsted bases. For example, at low temperatures CO undergoes an interaction with the surface cations and different surface oxygen groups and in some cases an interaction between CO and surface hydroxyl groups was observed. In the next chapter, the interaction of CO molecules with different surface species like cations, hydroxyl groups and surface oxygen species is described in detail.

2.11.3.1 CO Interaction with Cations

At low temperatures, CO adsorbs differently on the surface cations. Adsorption of CO on the surface leads to a shifting of the CO stretching vibration frequency (gaseous CO absorbs at 2143 cm^{-1}), usually, to lower but also to higher frequencies. A shifting of the vibration frequencies in the spectral range above and below the CO in the gas phase were explained as follows.

Two features of the molecular orbitals of CO the adsorption bands in the spectral region below the gas phase of CO are explained by organometallic chemistry [73]. The highest-energy occupied molecular orbital (HOMO) has its largest lobe on carbon. It is through this orbital, occupied by an electron pair, CO exerts its σ -donor function, donating electron density directly towards an unfilled p, d or hybrid metal orbital. At the same time, CO has two empty π^* orbitals (LUMO), which also have larger lobes on carbon than on oxygen. This localization of π^* orbitals on carbon causes carbon to act as the principle site of the π -acceptors of the ligand. A metal atom having electrons in a d orbital of suitable symmetry can donate electron density to these π orbitals (π acceptance). These σ -donor/ π -acceptor interactions are illustrated in Figure 2.17. Both σ -donation (electron transfer from the weakly antibonding 5σ orbital of CO to the empty orbital of metal) and π acceptance (electron transfer from the d orbital of the metal ion to the

antibonding orbital of the CO) would be expected to weaken the C-O bond and to decrease the energy (frequency) necessary to stretch that bond.

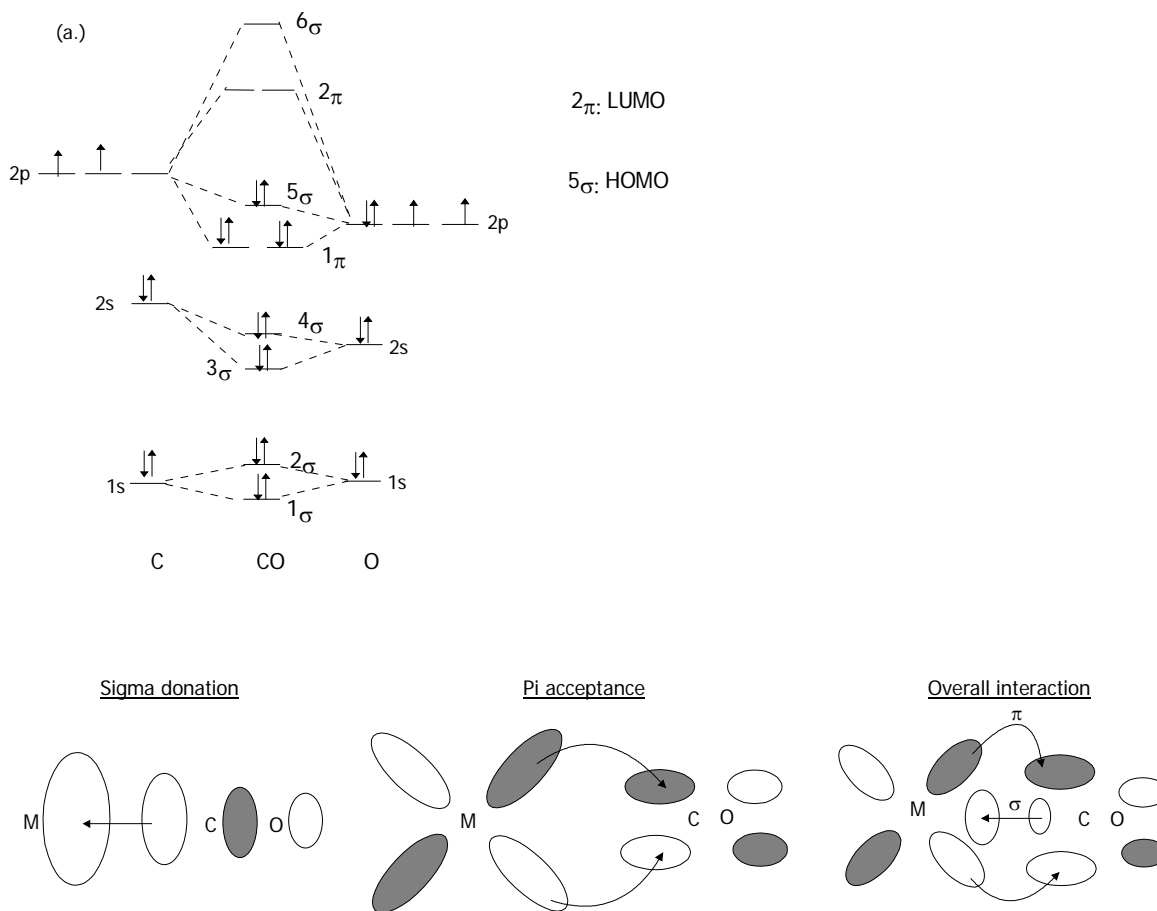


Figure 2.17: Molecular orbitals of CO (top), σ and π interactions between CO and metal atom [73].

The reason for the shift of the CO vibration to higher frequencies is not clear. It is suggested by several authors that metal atoms without d electrons cannot transfer their electrons from the d orbital into the anti bonding orbital of the CO, therefore a back donation is not possible, which would also cause a shifting of the band maximum to higher frequencies. In this case only σ donation exists, which strengthens the bond. Therefore the CO absorption can be detected at a higher wavenumber. These complexes are unstable and already removed by evacuation at room temperature. They are usually formed only under CO atmosphere after high temperature treatment in vacuum. Scarano et al. [74] explain the shifting of the CO vibration to higher frequencies additionally to the effect of σ donation

mainly due to the Stark effect, which is induced in the CO molecule by the axial electric field created by a metal atom (Zn^{2+}). According to Knözinger et al. [47], purely electrostatic models may well describe the adsorption interaction of CO with a cationic surface site, if π -back donation does not contribute to the coordination bond and the carbonyl stretching frequency is observed at values higher than the stretching frequency of the free CO molecules. The authors suggested that the carbonyl stretching frequencies of the adsorbed CO is influenced by several simultaneously occurring effects. Mechanical coupling between M-CO and MC-O modes (M indicates the coordination site) can lead to significant high frequency shifts of the MC-O mode. In addition, lateral interaction between CO oscillators may occur, if the coordination sites are located on metal and metal oxides are located in close proximity (kinematic coupling). The same authors have observed absorption bands in the presence of CO on TiO_2 (rutile) at 2133, 2150, 2174 cm^{-1} . The bands at 2133 and 2150 cm^{-1} were assigned to physisorbed CO due to their thermal stability. The authors reported that the band at 2174 cm^{-1} shifted to 2178 cm^{-1} with increasing temperatures and is present up to RT. Due to thermal stability of this band they assumed that the band belongs to $Ti^{x+} \leftarrow CO$ complex.

Table 4 gives a literature overview of adsorbed CO on different oxides and detected CO frequencies.

Table 4: *Vibration frequencies of CO molecules adsorbed on the various oxide surfaces. A literature overview.*

Metal oxide	$\nu_{(\text{CO})}$ [cm^{-1}]	Reference
Cr ₂ O ₃	2185	[75]
TiO ₂	2131, 2192, 2209	[76]
SnO ₂	2203, 2200	[5, 28]
CeO ₂	2169	[47]
Co ₃ O ₄	2190, 2180	[22]
NiO	2190	[21]
Ga ₂ O ₃	2167	[47]
Fe ₂ O ₃	2170	[22]
Al ₂ O ₃	2195	[47]
ZnO	2190	[74]
Pt/ZnO	2138, 2100, 2095, 2087, 2062	[77]

2.11.3.2 CO Interaction with Surface Oxygen and Hydroxyl Groups

In addition to adsorption on cations, CO can interact with different surface oxygen species and hydroxyl groups. Forms of adsorbed oxygen with different reactivity interact with CO to create surface complexes. As reaction products differently bond carbonate species were found (see literature in Figure 2.19) like unidentate, bidentate carbonates ($\text{CO}_3^{(2-)}$), carboxylates (CO_2^-). These carbonates, as well as carboxylate complexes decompose to CO_2 at the temperature of the catalytic reaction in the presence of oxygen in the gas phase. Therefore, these complexes are intermediate products of the CO oxidation. Figure 2.18 shows carbonate related species, their structure, as well as their absorption frequencies in the IR spectra.

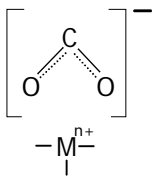
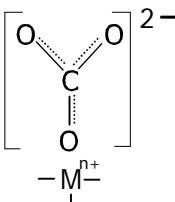
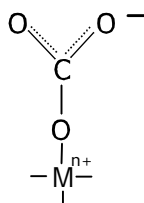
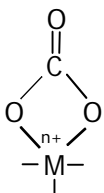
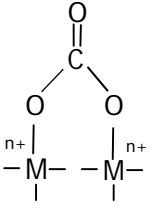
Species	Structure	Freq. [Lit]	Freq. [obs]
carboxylate ion		1560-1630 ($\nu_{as}COO^-$)	1650
		1350-1420 (ν_sCOO^-)	—
carbonate free ion		1450-1420 ($\nu_{as}CO_3^{2-}$)	
		1090-1020 ($\nu_sCO_3^{2-}$)	
monodentate carbonate		1530-1470 ($\nu_{as}COO^-$)	
		1300-1370 (ν_sCOO^-)	
		1080-1040 ($\nu C-O$)	
chelating bidentate carbonate		1530-1620 ($\nu C=O$)	
		1270-1250 ($\nu_{as}COO$)	
		1030-1020 (ν_sCOO)	
bridging bidentate carbonate		1620-1670 ($\nu C=O$)	1750
		1220-1270 ($\nu_{as}COO$)	—
		980-1020 (ν_sCOO)	—

Figure 2.18: Structure of differently bound carbonate carboxylate species and their characteristic frequencies in the IR spectra.

The summary of results on tin oxide obtained by IR spectroscopy is presented in Figure 2.19. Gaseous CO_2 was detected as reaction product between 200 and 400°C. Experiments summarized in Figure 2.19 were performed on a O_2 preconditioned SnO_2 surface in the temperature range between 150 and 400°C.

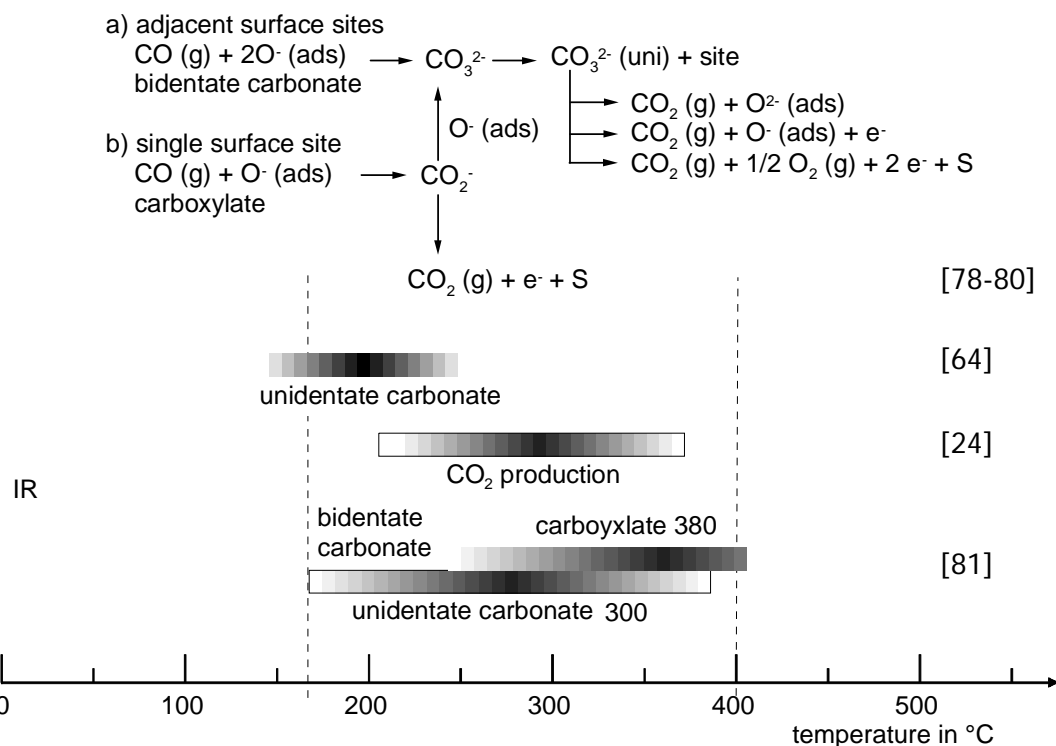


Figure 2.19: Literature survey of CO related species found using infrared spectroscopy at various temperatures on O₂ preconditioned SnO₂ surfaces.

Additional to the results summarised in Figure 2.19, investigations on zinc oxide using infrared spectroscopy showed that, depending on the temperature, the oxidation of CO can take place via two mechanisms [21 and references therein, Figure 2.20]. At low temperatures, the reaction proceeds via a concerted mechanism; i.e. the reaction of CO with surface oxygen ions and formation of the products occur at the same time. At high temperatures, a stepwise mechanism with alternative oxidation takes place. A schematic drawing of both proposed reaction mechanisms is shown in Figure 2.20.

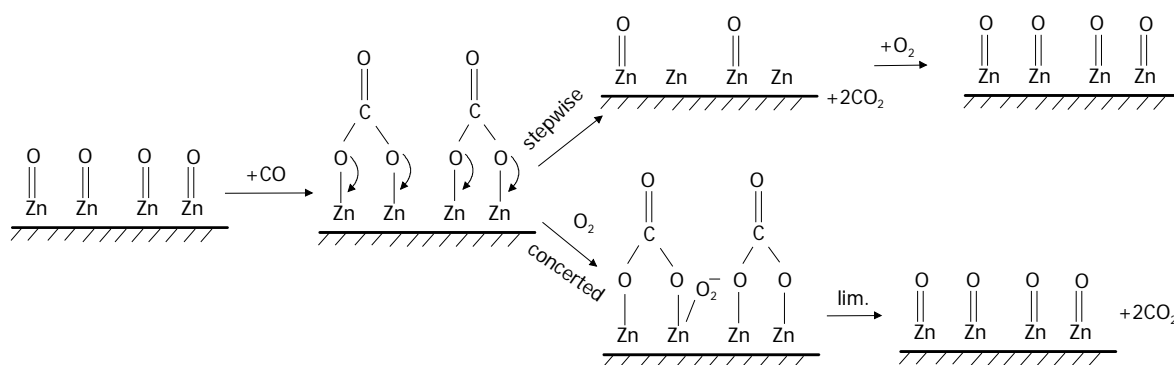
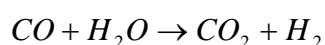


Figure 2.20: Step wise and concerted reaction mechanism for CO-oxygen interaction on ZnO. Stepwise reaction mechanism is proposed at high temperatures, concerted reaction mechanism is proposed at low temperatures [21].

It has several times been pointed out that water presence enhances the reactivity of CO [68, 82]. For the explanation of the CO reaction mechanism in the presence of humidity, various models were proposed: One of the assumptions was that water increases the reactivity with oxygen [62]. An increase of humidity causes an increase of oxygen vacancies. Through filling of oxygen vacancies by chemisorption specific oxygen sites are formed. The increase of available oxygen for CO enhances the sensor signal. The other important assumption is the reaction between CO and surface hydroxyl groups [9, 68, 83, 84, 85], which was proved by the work function and conduction measurements performed on Pd-doped sensors. Accordingly, CO reacts with surface terminal hydroxyl groups, which release H atoms in order to form CO₂. Released hydrogen atoms combine with lattice oxygen (rooted hydroxyl groups) and provide donors, *i.e.* free charge carriers. This mechanism would have been supported by an increase of the intensity of the absorption bands belonging to rooted OH groups in the DRIFT measurements.

Another reaction mechanism called "Water-Gas shift" reaction (WGS) is proposed by means of IR investigations on different metal oxide surfaces.



Occurrence of this reaction depends on the catalyst and temperature [22]. The reaction product of the WGS reaction is H₂ in the gas phase

additional to CO₂ with formates groups as intermediate product in addition to other carbonyl groups of various types. For a detailed description see reference [22] and references therein.

2.12 Influence of Surface Additives on the Sensing Mechanism

The functionality of the catalyst is either to increase the concentration of reactants at the surface or to lower the activation energy for the reaction, or both. Dopants are added to semiconductor materials, in order to: increase the charge density in the bulk, obtain grains with well defined grain sizes [86], enhance the sensing properties [87, 88, 89, 90], gain faster response and recovery time, get better reproducibility.

The effect of dopants on semiconductor surface is explained by two alternative models. Both models assume that the doping particles are located at the surface of much bigger grains of tin oxide and are homogeneously distributed on the surface.

1. Spill-over or catalytic effect: The spill-over effect is described schematically in Figure 2.21. Catalyst particles on the surface are able to activate certain gas molecules, e.g. dissociation of oxygen or hydrogen. The spill-over effect can accelerate the reaction, which results in shorter response times and higher sensitivities. Well known for this effect is the spill-over effect of hydrogen and oxygen from metal catalyst (Pt) onto the semiconductor support [91, 92, 93, 94]. Since the bonding energy of Pt atoms to the hydrogen or oxygen atoms is not so different from the bonding energy one hydrogen or oxygen atom to the other, only little energy is needed to dissociate hydrogen or oxygen molecules. Consequently, the catalyst reduces the energy normally needed for dissociation to a great extent. The subsequent spill-over onto tin oxide is possible after breaking the rather weak bond between hydrogen and/or oxygen and Pt. Hence the catalyst lowers the activation energy needed for the dissociation process and increases the probability of a reaction.

2. Fermi energy control: By this effect the sensor signal is determined mainly by the electronic contact of the semiconductor with the catalyst. Oxygen species at the surface of the catalyst trap electrons from the semiconductor. Since the density of electrons in the bulk has changed by this process, a depletion layer is created and band bending occurs. The catalyst particles become oxidised in the ambient gas atmosphere. The stoichiometry of the catalyst (MO_{2-x}) depends on the composition of the ambient air and so does the position of its Fermi level. At equilibrium, the Fermi level of the catalyst and the semiconductor are at the same height. Since the gas reacts with the semiconductor via the catalyst, the chosen catalyst can strongly change the selectivity of pure tin oxide.

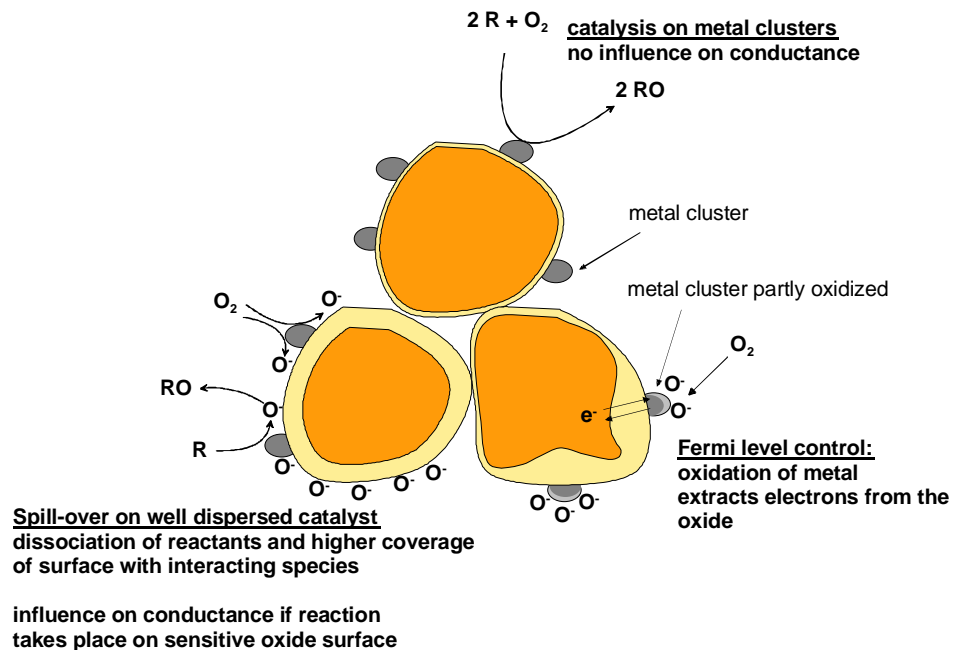


Figure 2.21: Different effects of doping. spill-over effect (left bottom), Fermi level control (right bottom).

2.13 Correlations between Spectroscopic and Electrical Data

The adsorption of gases leads to changes in the conductance of metal oxides, and to the occurrence of new absorptions or changes in existing bands, shifting of the already existing absorption bands in the infrared spectrum. The change in the conductance is associated with changes of the free carrier concentration which can also be detected by means of infrared

spectroscopy. Figure 2.22 shows a spectrum obtained through comparison of the spectrum recorded at 150°C in dry air with the spectrum recorded in the presence of 500 ppm CO.

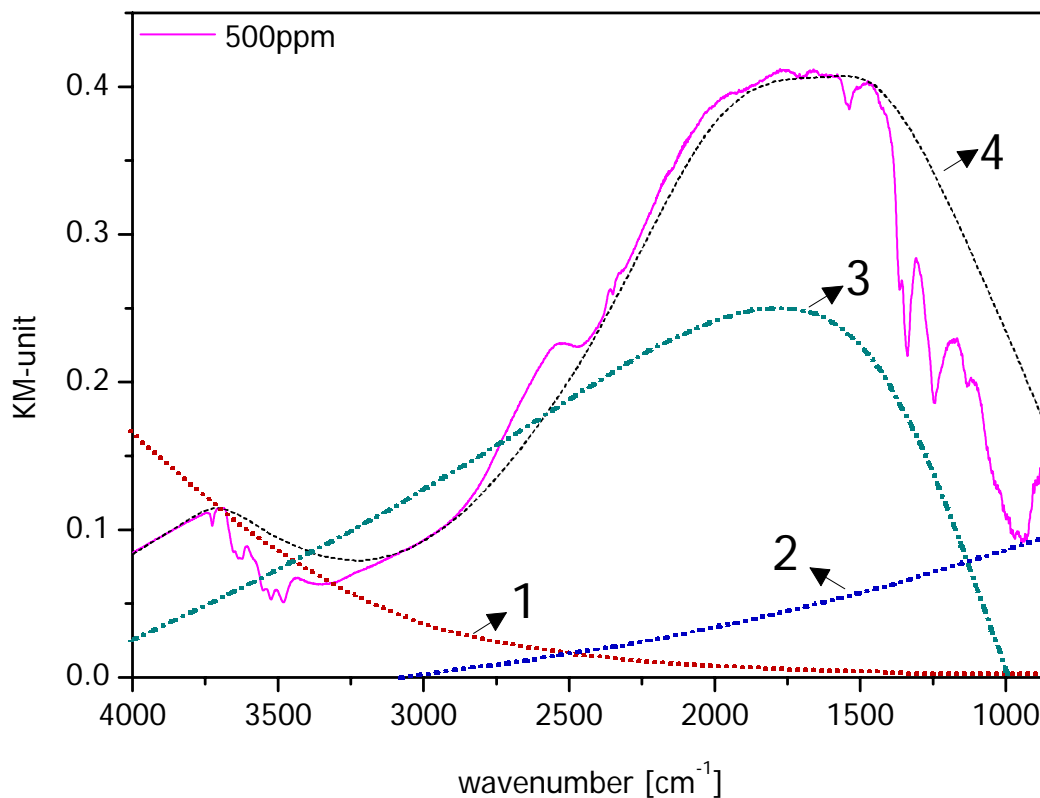


Figure 2.22: Spectrum of an un-doped sensor in the presence of 500 ppm CO at 150°C in dry air. Curve 1, roughly determined Rayleigh scattering from the particle; curve 2, scattering from the electrons; curve 3, broad absorption due to electronic transition from shallow levels in the gap to the conduction band; curve 4, roughly determined course of the baseline resulting from the above mentioned effects.

Changes in the difference spectrum are correlated in two different ways with the changes in conductance. Changes in the fine structure caused by adsorption and chemical reactions occur on the surfaces which often result in a change in the concentration of free charges. Furthermore a broad absorption over the total MIR spectral range appears in the difference spectra. In the literature, this broad band absorption so called X-Band was observed in several infrared investigations performed under different conditions (temperature, humidity, different background gas atmosphere etc.) [4, 37, 95, 96].

Chiorino et al. studied the broad absorption in detail and separated it into three parts as shown in the Figure 2.22, curve 1, presents the scattering effect due to the particle size which does not appear in the measurements presented in this work, since this was eliminated through the comparison of spectra originated from the same sensor. The second effect which contributes to the shape and intensity of the broad absorption is scattering of electrons in the conduction band (curve 2).

The X-Band was (roughly shown in Figure 2.22, curve 3) observed in infrared spectra of several metal oxide materials (SnO_2 , Ga_2O_3) where the oxygen content diminishes, because of either a temperature effect, the adsorption of another species or a surface reaction of adsorbed oxygen species with reducing gas molecules. This broad absorption is interpreted by the authors through the absorption of the second donor ionisation energy by electrons in the neighbourhood of the oxygen vacancies in the bulk of the tin dioxide domain. In the presence of oxygen, the transmission of the metal oxide material increases because of the electron capture by all kinds of adsorbed oxygen species. Upon a decrease in the surface-charge density the transmission decreases because the captured electrons return to their position around the oxygen vacancies where they absorb the donor ionisation energy for the $V_{\text{O}}^{\cdot} \rightarrow V_{\text{O}}^{\cdot\cdot} + e^-$ transition (electronic transition from shallow levels into the conduction band, Figure 2.23). The distance of donor levels to the conduction band determines the absorption edge in the IR spectrum and the density of these levels is proportional to the intensity of the absorption band (e.g for the choice of the photoconductive detectors in suitable spectral range).

The maximum and the absorption edge as well as the shape of the broad band absorption depend on the measurement condition. For example in our measurements, the cut off of the spectra was approximately at 850 cm^{-1} corresponding to 0.106 eV.

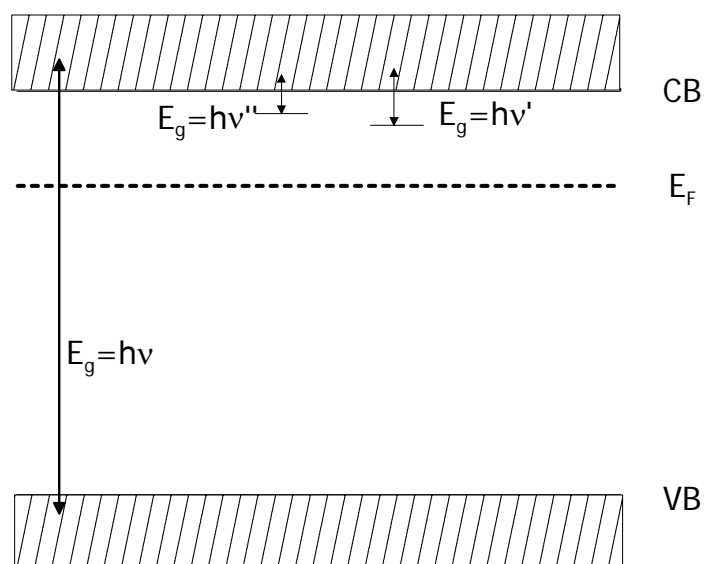


Figure 2.23: Graph of the semiconductor band structure. The absorption edge gives the distance between donor level and the conduction band. The density of the level gives the intensity.

On the other side, this interpretation is in contradiction with the results obtained by other investigators. It is well known that the donors of singly and doubly ionised oxygen vacancies with the donor levels located around 0.03 and 0.15 eV below the conduction band edge are completely ionised in the temperature range for sensor operation (200-400°C).

In the measurements performed for this study the broad absorption is reproducibly detected. Its maximum and intensity depends on the measurement conditions. Furthermore, a rough correlation between the intensity of the broad absorption and the sensor signal was observed.

However, in this work it is avoided to interpret this broad absorption. Characterisation and origin of the broad band absorption are not in the frame of this work. For a better understanding of this broad absorption additional studies are needed. The focus of this work is the analysis of the spectra and by means of changes in the molecular levels and the proposal of the reaction mechanisms.

3 Experimental Section

3.1 IR Spectrometer

DRIFT spectra were recorded with an FTIR spectrometer (Bruker, IFS 66v), which is evacuable up to 10^{-3} mbar. The quality of the vacuum depends on the airflow, which is required for the stabilisation of the moveable mirrors in the Michelson-Interferometer. The air is dry and CO₂ free.

Since the absorption of the surface species, especially bands corresponding to surface OH groups, appear in the same spectral region as water in the gas phase, and is very small, it is important to evacuate the whole spectrometer until it is void of water and CO₂. For the measurements in this work, the spectrometer was evacuated at least 60 minutes before the first spectrum was recorded. Spectra were recorded with the resolution of 2 cm^{-1} and in order to get a good signal noise ratio with 1024 scans.

A schematic drawing of the set-up which allows parallel spectroscopic and electrical measurements is shown in Figure 3.1.

For the spectroscopic characterisation of the sensors different conditions (dry/humid air, CO+air mixtures) are prepared. For measuring the Diffuse Reflectance a special DRIFT-unit and for positioning of the sensor a special home made sensor chamber were used.

A gas mixing bench allows for the exposure to different gas mixtures. For heating the sensors a power supply was used. The humidity level of gases was controlled using humidity sensors. Two different humidity sensors were used for measuring the humidity in low and high concentration ranges.

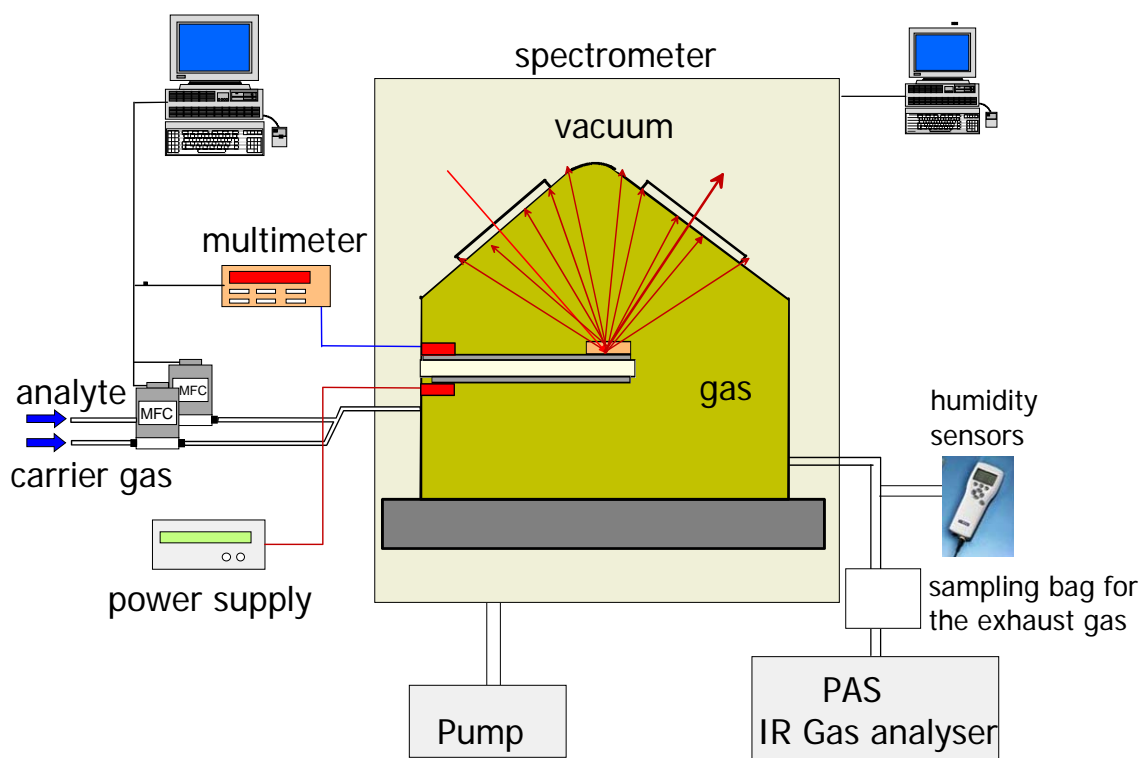


Figure 3.1: Schematic experimental set-up: It allows the parallel measurements of IR absorbance and electric resistance. While the sensor is exposed to gases using a gas mixing station, the spectrometer is evacuated. The sensor holder is connected to the power supply for heater and multimeter. The humidity of the gases was monitored with two humidity sensors, one of them for small humidity levels, the second one for higher humidity levels. The gas in the exhaust is collected in a special bag and analysed with a IR gas analyser based on photoacoustic detection.

3.2 DRIFT-unit

A photograph of the DRIFT unit "Praying Mantis" from Harrick with the sensor chamber is shown in Figure 3.2. It has six mirrors; two of which are ellipsoid mirrors. This mirror arrangement is based on the "off-axis" principle [97], it means these ellipsoid reflectors are for the collection of the diffuse reflectance. They have a gap in the "specular direction" (in respect to the sample surface), which minimizes the specular or direct reflection.

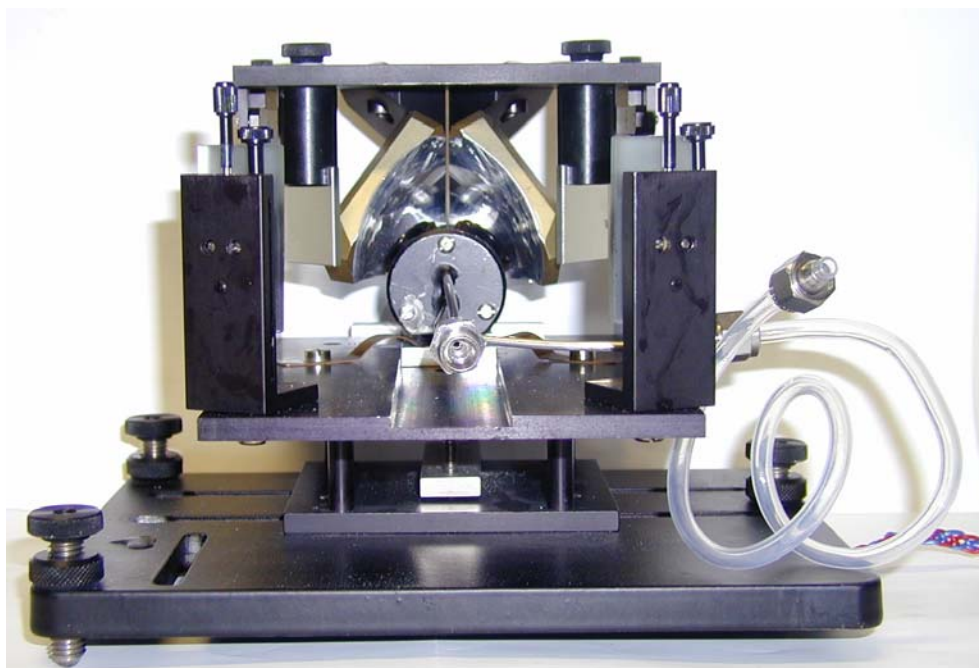


Figure 3.2: DRIFT-unit "Praying Mantis" with sensor chamber. Two ellipsoidal mirrors collect diffuse reflection. These two ellipsoidal mirrors are positioned on the principle of "off axis" which minimizes direct reflection.

3.3 Sample Chamber

Figure 3.3 shows the sample chamber for sensors with the sensor holder.

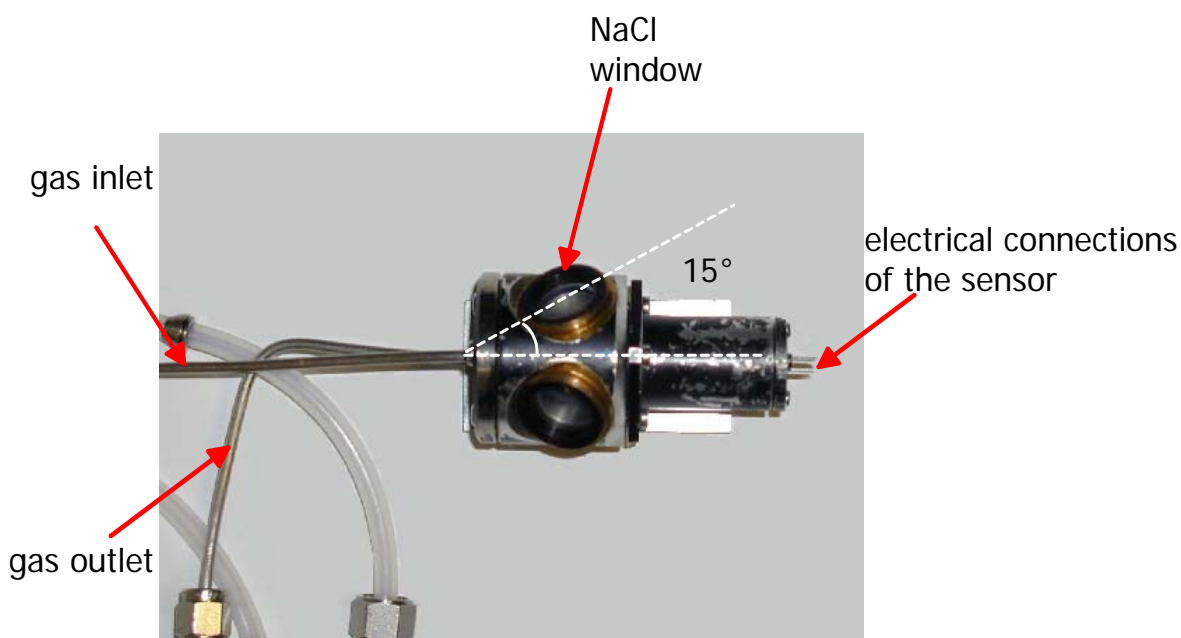


Figure 3.3: Sensor chamber with sensor holder.

It is out of black painted aluminium, mounted on an aluminium plate and provided with two NaCl windows of a diameter of 20 mm and a thickness of

2 mm, which allows for the maximum gain of the diffuse reflectance. The windows are placed in the sensor chamber at an angle of 15° (see Figure 3.3) which is perpendicular to the incident radiation, in order to avoid the refraction. For the inlet and outlet of the gas, two metal tubes are connected to the chamber. The sensor holder is provided with the electrical contacts for heating the sensor and resistance read out.

3.4 Gas Mixing Bench

For testing of the sensors under gas exposures corresponding to the specific application atmosphere of the sensor the required gas mixtures were obtained using a home made gas mixing bench shown in Figure 3.4.

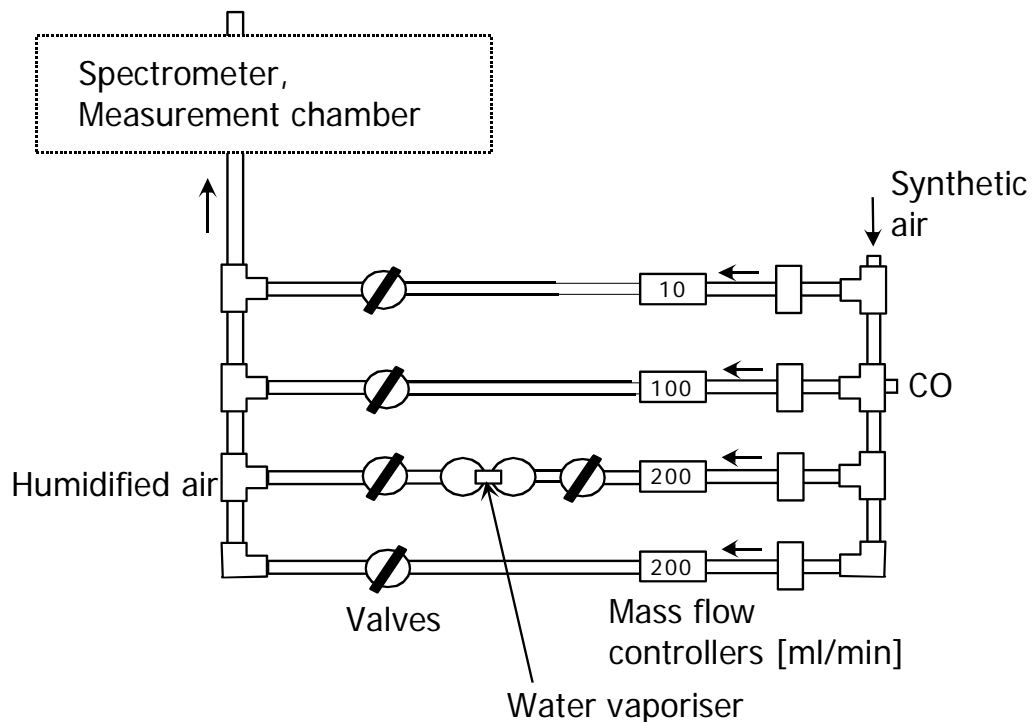


Figure 3.4: Schematic picture of a four-channel gas mixing bench. Test gas is introduced either from gas cylinders or added by flowing synthetic air through vaporisers. The latter is used to adjust the relative humidity.

The gas mixing bench provided with four computer-controlled mass flow controllers and valves can combine up to two test gases with dry and water vapour saturated synthetic air. It is operated by a home-made software programme called "POSEIDON". The mass flow controllers and the solenoid

valves are controlled via a D/A card. The tubing of the gas channels consists mainly of (electrical polished) stainless steel pipes; vacuum tight teflon FEB tubes were used for the rest of the tubing, i.e. the connections between the sensor chamber and the connections soldered in the sample chamber of the spectrometer.

3.5 Sensor Heating

For heating of the sensor a stabilised power supply (Hewlett Packard DC power supply E3610 A) was used. The temperature calibration of the sensors was made by using an infrared pyrometer (Maurer KTR 2300-I). The pyrometer detects the infrared emission from a measurement spot of about 1 mm^2 and calculates, using the specific emission coefficient ε ($\varepsilon_{\text{SnO}_2} = 0.75$) of the material, the temperature of the sensitive layer.

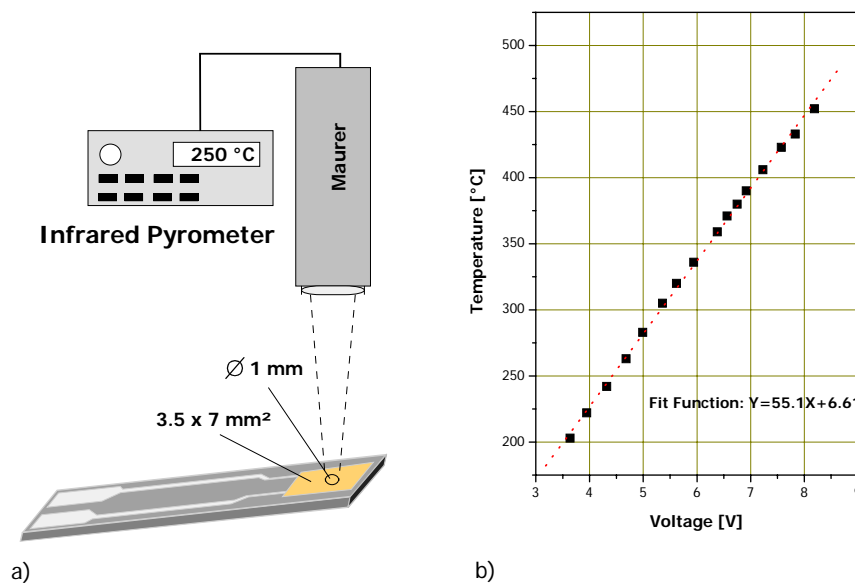


Figure 3.5: Calibration of the Pt heater: a) measurement set-up, b) calibration curve.

A pictorial sketch of the set-up is presented in Figure 3.5a. The relationship between the applied voltage and resulting temperature is shown in Figure 3.5b. An almost linear relationship between the applied voltage and temperature was obtained.

3.6 Samples

The commercial powder was bought from the company “Merck” in Germany. According to the information obtained from Merck the powder was obtained by direct oxidation of tin at 1200°C. However, they did not disclose the exact description of the preparation method.

Figure 3.6 shows the flow chart of a home-made sensor fabrication consisting of two main parts: 1. Preparation of the powder used as sensitive layer, 2. Fabrication of the sensor based on these powders using the screen printing method. A detailed description of the sensor preparation including optimisation of the sensor can be found in [85].

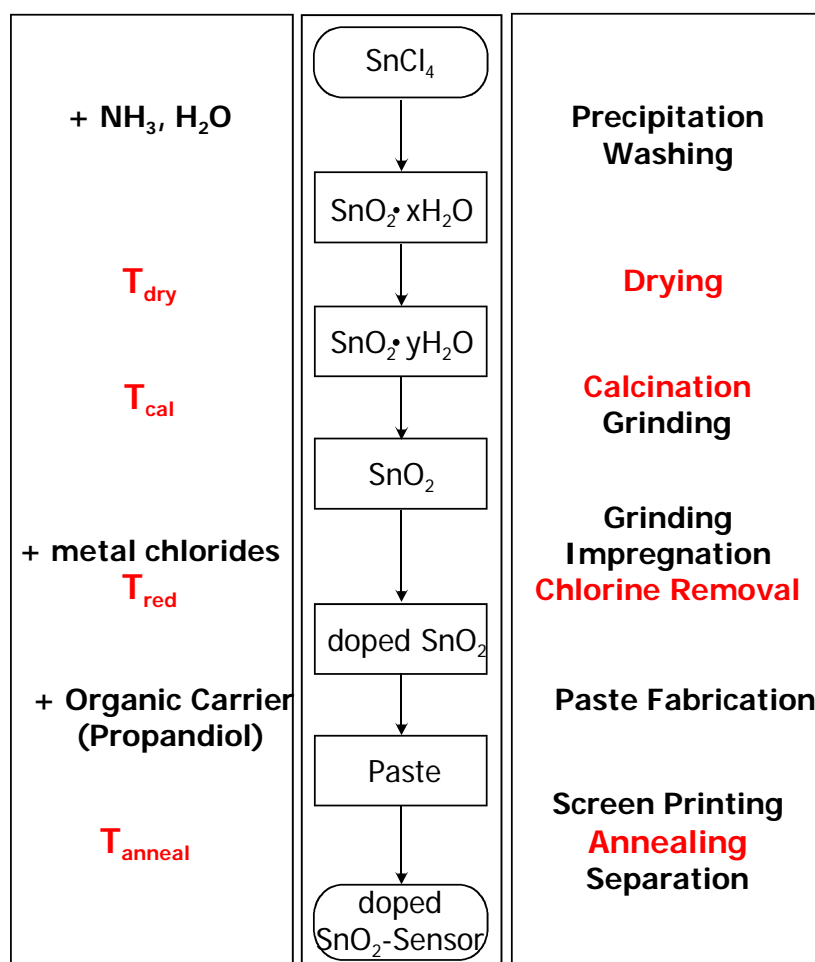


Figure 3.6: Flow chart summarising the preparation of SnO₂ thick film sensors based sol-gel method [85].

Figure 3.7 (top) shows SEM pictures of powders with grain sizes of 10 nm and 100 nm. Both powders are polycrystalline porous materials. Out of the

phenomenological measurements it is known that the powder with the grain size of 10 nm is very sensitive to CO. Both powders are greatly suitable for DRIFT measurements due to their polycrystalline properties and rough surfaces.

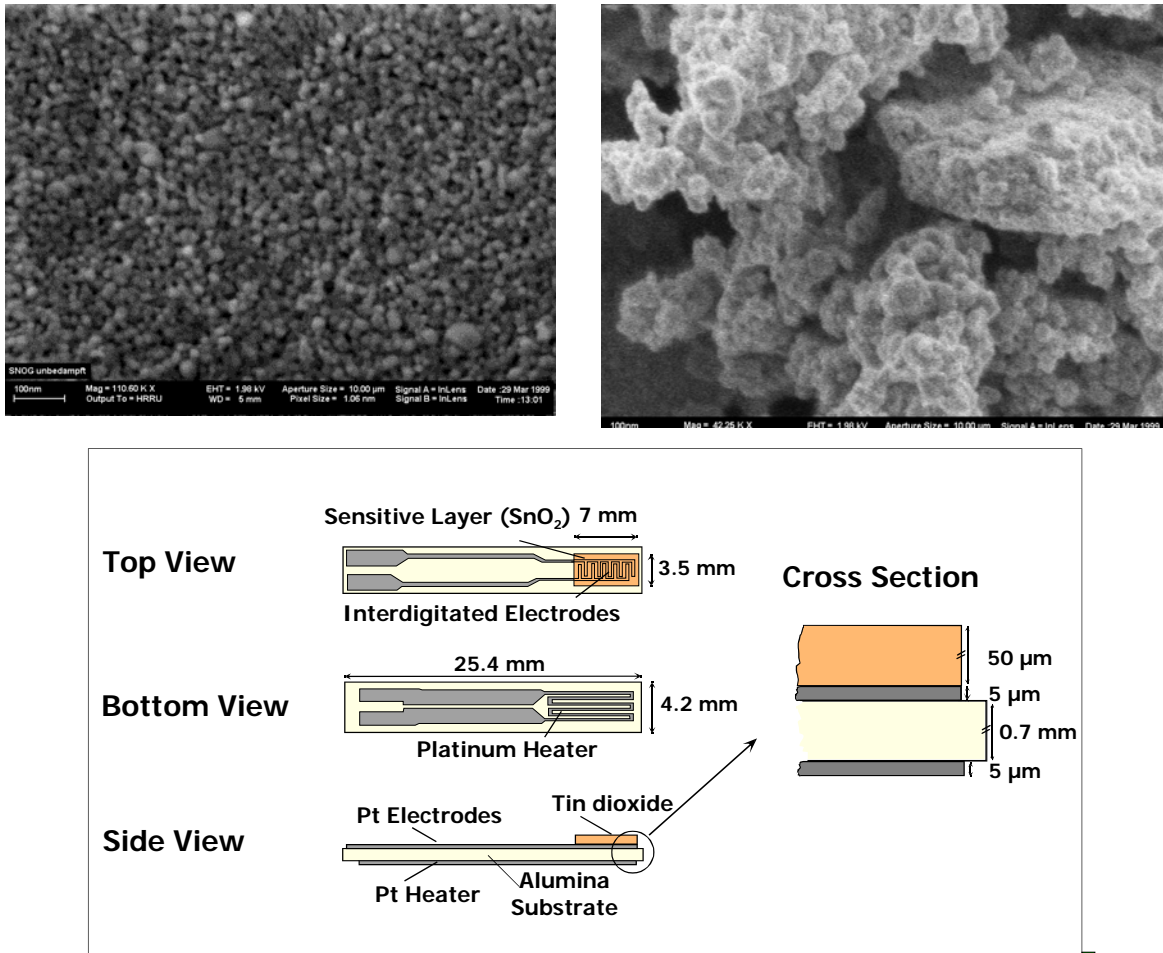


Figure 3.7: Sol-gel prepared tin oxide powder. Top, left: Tin oxide powder with the grain size of 10 nm. Top, right: Tin oxide powder with the grain size of 100 nm. Bottom: Sensor layout from different side views.

Figure 3.7 (bottom) shows the sensor layout with dimensions from different views. Pt electrodes for heating of the sensor are on the backside of the alumina substrate and Pt electrodes with interdigital structure located on the top side of the substrate. The sensitive layer is screen printed on the interdigital structure.

3.7 Drying and Thermal Activation of the Sensors

After screen printing, the substrate stays at room temperature for 1h allowing the paste to settle. Subsequently, the substrate is placed in a drying oven set at 80°C. Finally, the substrate is inserted into a moving belt oven. During the final annealing "firing", the organic binders of the film are removed. The moving belt oven (Centrotherm Centronic DO 1600-60-D5) has four individual heating zones. The temperature of each heating zone, the speed of the moving belt and the gas flow inside each heating zone creating the ambient gas atmosphere around the substrate can be individually regulated. The firing profile was adjusted in such a way that a gradual heating from room temperature to the maximum temperature (500-700°C), and a gradual cooling back to room temperature was achieved (Figure 3.8). The velocity of the moving belt is adjusted to allow the substrate to stay in the maximum temperature zone for 10 minutes. Filtered, compressed air was chosen as the gas atmosphere for the firing step.

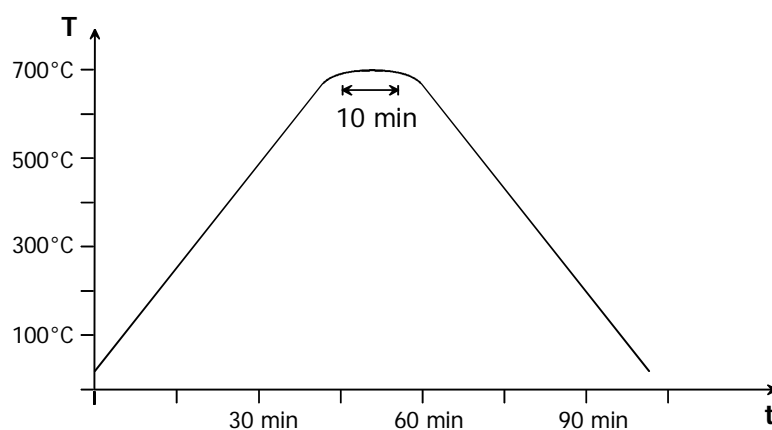


Figure 3.8: Temperature/time profile for annealing and thermal activation of the sensors.

Before the DRIFT measurements on the sensor were performed, the sensors were heated in the belt oven with the above described heating procedure, in order to eliminate the water content originating from ambient air. Besides this the sensor were kept heated at 300°C under laboratory conditions.

3.8 Sampling of Gases in the Exhaust for the Photoacoustic IR Spectrometer

In order to analyse the gases in the exhaust a FTIR spectrometer (Innova 1301) based on photoacoustic detection was connected to the sensor chamber.

A pump system is integrated into the Innova 1301 instrument for the defined and reproducible purging of the PAS (Photoacoustic Spectroscopy) cell. The purge cycle is divided into several steps:

1. The sampling tube is purged at a high rate (30ml/s) with the test gas. The flush valve is open, the inlet and outlet valves are closed. The length of the step can be selected depending on the length of the sampling tube.
2. The PAS cell is purged at a low rate (5 ml/s) with the test gas. The flush valve is closed; the inlet and outlet valves are open. The lower purge rate is achieved by opening a shunt valve, so that the pump works in recirculating air operation. The length of this step is fixed to 10 s.
3. The inlet and outlet valves as well as the shunt valve are closed, the pump is turned off and the photoacoustic measurement of the sample is started.

The flow rate of test gas through the PAS cell is 50 ml/min. The exchange of an old sample with a new one is only achieved through the dilution effect (50 ml/3 ml), i.e. the cell volume is purged 16 times.

To avoid memory effects, all surfaces in contact with the sample are made of inert materials as Teflon (PTFE), viton or stainless steel. For the protection of the PAS cell against particles, a Teflon membrane filter with 10 µm pores is built in the gas pathway. This is needed as intruding particle contamination could possibly clog the capillaries to the microphones and also decrease the reflectivity of the cell.

3.9 Measurement Protocol

All spectra were recorded as single channel spectra (without reference). For the characterisation of the samples at different temperatures, the sample was heated at the desired temperatures in synthetic dry or humid air until the value of the sensor resistance was stable. For CO measurements, the sensors were exposed alternately to air and a CO+air mixture for one hour each.

The measurement procedure is schematically presented in Figure 3.9. A spectrum was recorded ten minutes before switching the conditions.

For the calculation of the $-\log$ Reflectivity ($-\log I/I_0$) or Kubelka-Munk function a pair of spectra recorded just before and during gas exposure were used.

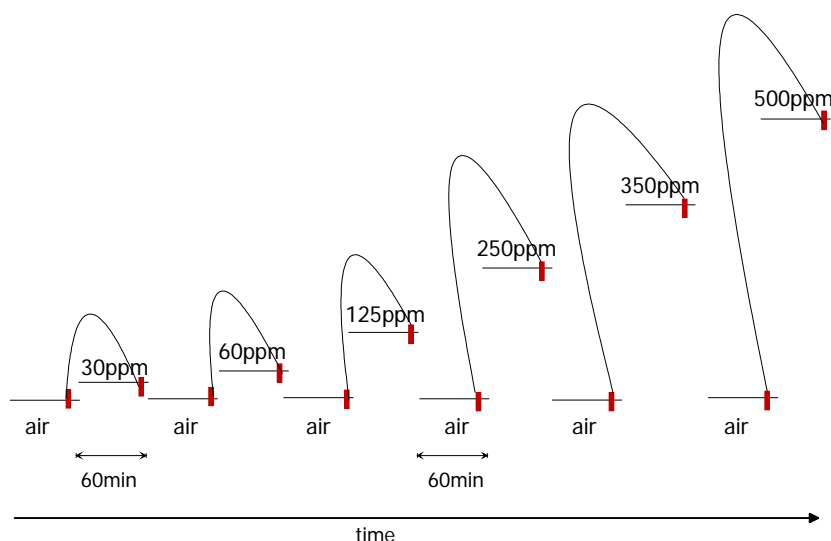


Figure 3.9: Schematical presentation of the measurements route. Spectra were recorded 10 minutes before switching the valves. As reference spectra, a spectrum recorded before the respective CO concentration was used.

3.10 Band Analysis

The bands in the IR spectra can be fitted by Lorenz, Gauss or Voigts functions. The latter one consist of a Gauss and Lorenz part and is the most suitable function for the bands obtained in an IR spectrum, since the curve form of the IR bands are influenced by homogeneous and heterogeneous band broadening. Homogeneous broadening (broadening through the

impulse) correspond to a Lorenz profile, heterogeneous broadening corresponds to a Gauss profile.

In this work, the best results were obtained by applying Lorenz and Voigt functions. For most of the bands a Lorenz function was used. The Voigt function is applied only for the broad band belonging to the hydrated proton species.

For the curve fitting a small spectral range is selected and on this spectral range a baseline correction was performed. Through the baseline correction the wings of the Lorenz curve are cut. The error is calculated and can be found in the literature. The error is between 10 and 20%. In this work the error bars are calculated for 10%.

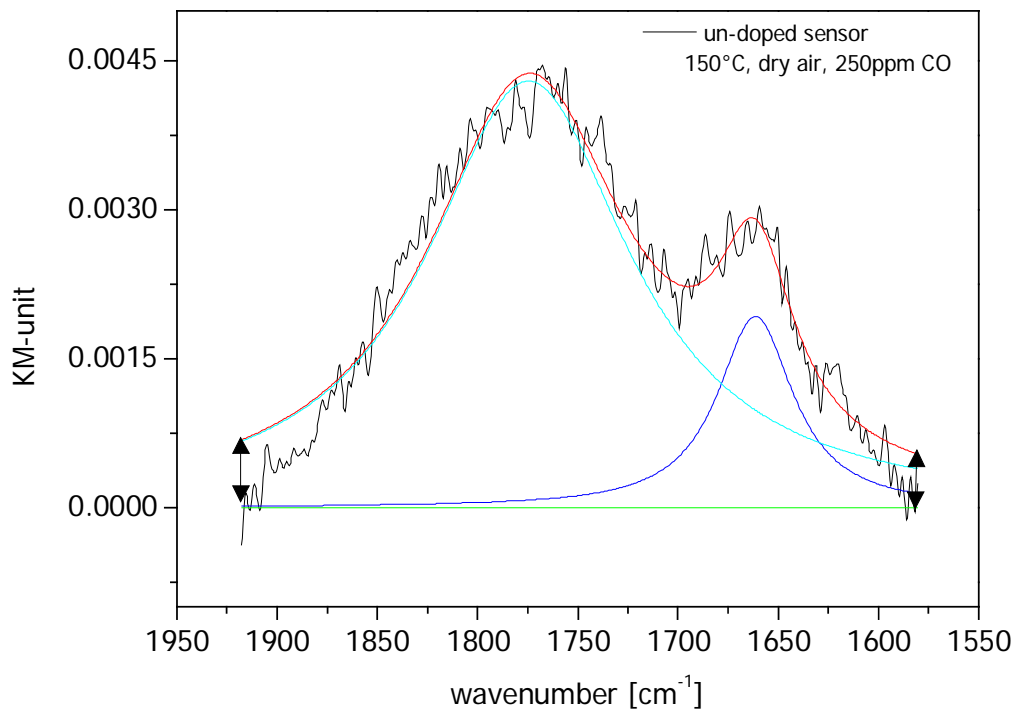


Figure 3.10: Schematical presentation of the band analysis. By the baseline manipulation the wings of the curves are cut. The difference between the theoretical and experimental curve is shown in the picture with the arrows.

4 Results and Discussion

The main focus of this chapter is the characterisation of tin dioxide thick film sensors under different conditions like temperature, humidity and different gas atmospheres using diffuse reflectance infrared spectroscopy. Electrical DC measurements conducted in parallel to the DRIFT measurements will also be presented in this section. Parallel recording of the sensor resistance acts as reference data in this study.

In the previous work [98] differently prepared powders with different grain sizes (freshly bought and old commercial powders, sol-gel prepared powders with a grain size of 100 and 10 nm) were measured by DRIFT-spectroscopy. These results obtained on powders at room temperature under vacuum conditions are roughly included here, because they are very helpful for the characterisation of the sensor surface and understanding of the sensing mechanism of the thick film sensors, and can be compared with the results obtained on the sensor.

DRIFT and resistance measurements were performed on two types of homemade thick film SnO₂ sensors (un-doped and Pd-doped). The reason for the selection of these types of sensors is their high sensitivity towards carbon monoxide. For the characterisation of the surfaces, spectra were recorded in dry air between RT and 350°C in steps of 50°C. CO measurements were performed at three temperatures (150, 300 and 350°C), and at five different relative humidity levels (0, 4, 10, 20 and 50% r.h.).

For the RT measurements performed on the SnO₂ powders a spectrum of potassium bromide (KBr) was used as a reference. Since the texture of potassium bromide is strongly changing at elevated temperature and humidity, alkali halides cannot be used as a reference for the sensor measurements. Therefore, spectra recorded in air at the respective temperature and humidity directly prior to CO exposures were used as a

reference. The spectra recorded at different temperatures are presented as single channel spectra (raw data). For the CO measurements spectra are presented in KM-units.

4.1 Characterisation of the Samples

4.1.1 Characterisation of Differently Prepared SnO₂ Powders at RT

Figure 4.1 shows two spectral ranges in the spectra of four differently prepared tin dioxide powders; 1) commercial powder stored for a long time in laboratory atmosphere, denoted as old commercial powder, 2) freshly bought commercial powder 3) homemade powder with small grain size (10 nm, denoted with sg1) prepared by sol-gel method, and 4) homemade powder with large grain size (100 nm, denoted with sg2) prepared by sol-gel method. In order to eliminate contaminants on the surface, powders were heated under vacuum prior to the measurements and measured at RT under vacuum without contact to atmospheric air. Potassium bromide (KBr) powder was used as reference. KBr powder was pre-treated in the same way as the tin dioxide powders.

Freshly bought commercial tin oxide powder:

The IR spectrum shows several well-defined bands in the OH range (4000-3000 cm⁻¹) with various intensities (see Figure 4.1, top, solid line). Five main bands with different intensities were observed at 3655, 3638, 3602, 3558, 3520 and 3479 cm⁻¹. They are characteristic for the OH stretching modes of different types of surface hydroxyl groups [43]. The cause of different frequencies of these groups lies in their surroundings and their coordination number to the neighbouring atoms. In this work two types of hydroxyl groups were identified. These are terminal hydroxyl groups and rooted hydroxyl groups.

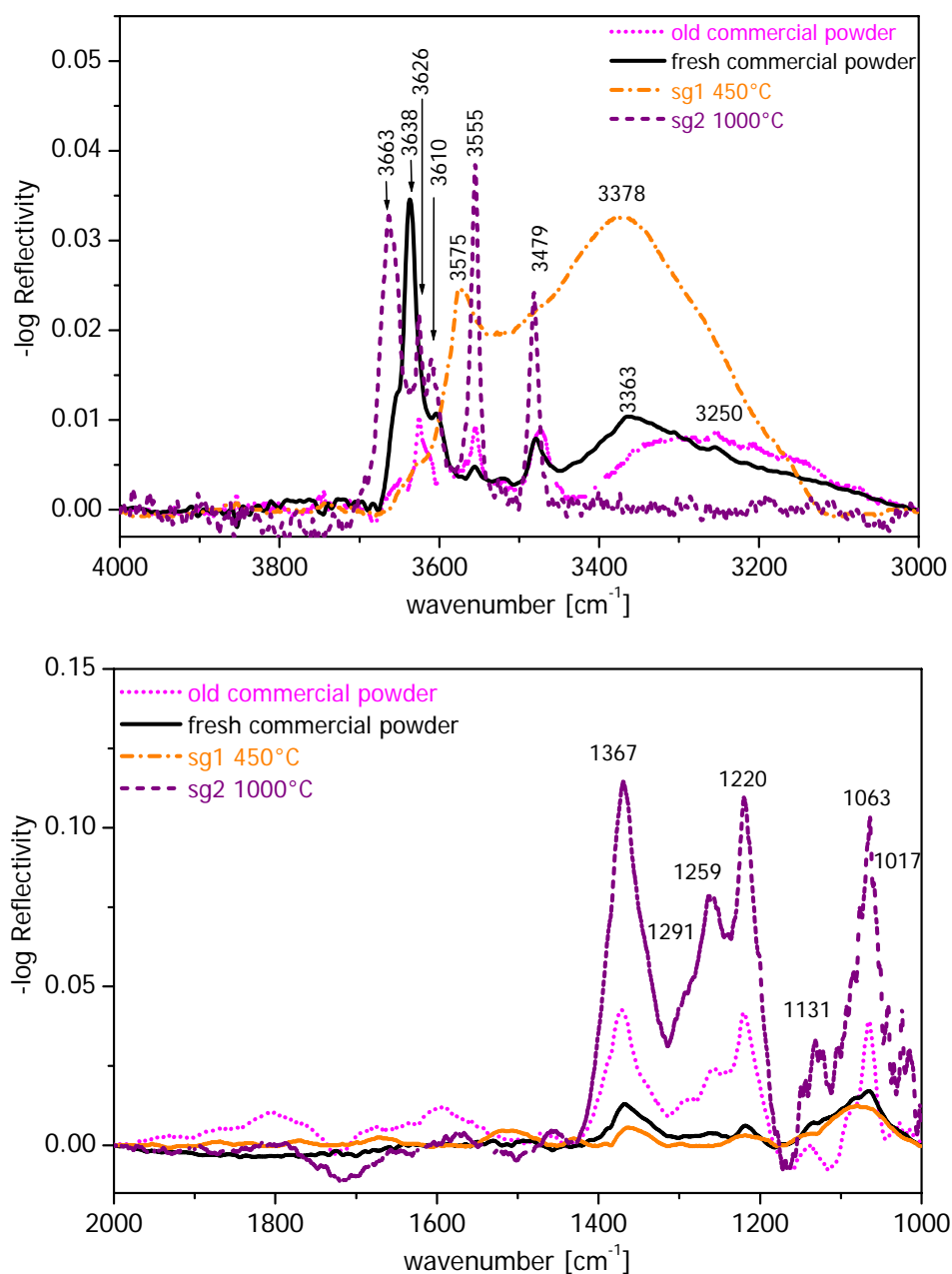


Figure 4.1: Different spectral regions of the differently prepared SnO_2 powders recorded at RT under vacuum, after heating up to 350°C under vacuum. Commercial tin dioxide powders (stored a long time in the lab atmosphere and freshly bought), tin oxide powders prepared by sol-gel method (denotation sg1: tin oxide powder calcined at 450°C , grain size 10 nm, sg2: tin oxide powder calcined at 1000°C , grain size about 100 nm)

Sharp bands at 3655 , 3638 and 3602 cm^{-1} are identified as surface terminal hydroxyl groups, which are defined as hydroxyl group bound to surface tin atoms. The bands at 3555 , 3520 and 3479 cm^{-1} are assigned to the rooted OH groups. Rooted OH groups are formed through bonding of

the hydrogen to a lattice oxygen atom. In a cartoon presentation, all types of hydroxyl groups on the metal oxide surface are shown in Figure 4.2.a.

Both kinds of chemisorbed surface hydroxyl groups (terminal and rooted) are created by the dissociation of water molecules on the surface. In this work, the assignment of the two types of hydroxyl groups on SnO₂-powder is based on the frequency shift caused by the isotopic exchange reaction (for the terminal OH group the frequency ratio is $\nu_{\text{OH}}/\nu_{\text{OD}} = 1.355\text{-}1.357$, for the rooted OH group 1.351 and for coordinated water 1.344) and by means of the results of other phenomenological measurements [9, 20, 98].

As described in chapter 2.11.2 the surface hydroxyl groups and water exhibit several interesting properties from the chemical nature and crystallochemical point of view, which influence the sensing reaction. These properties will be discussed in conjunction with CO measurements on powder and on sensors presented in chapter 4.1.4.

In the spectrum a very broad band corresponding to coordinated water, H-bonded Sn-OH species [43,57] or hydroxyl groups multiply bonded to adjacent Sn sites [57, 99, 100, 102] were also detected in the spectral range between 3400 and 3000 cm⁻¹. The band intensity of this absorption band decreased after storing in vacuum for two hours. In order to remove these bands, the sample had to be evacuated for a longer time and/or be heated to a higher temperature.

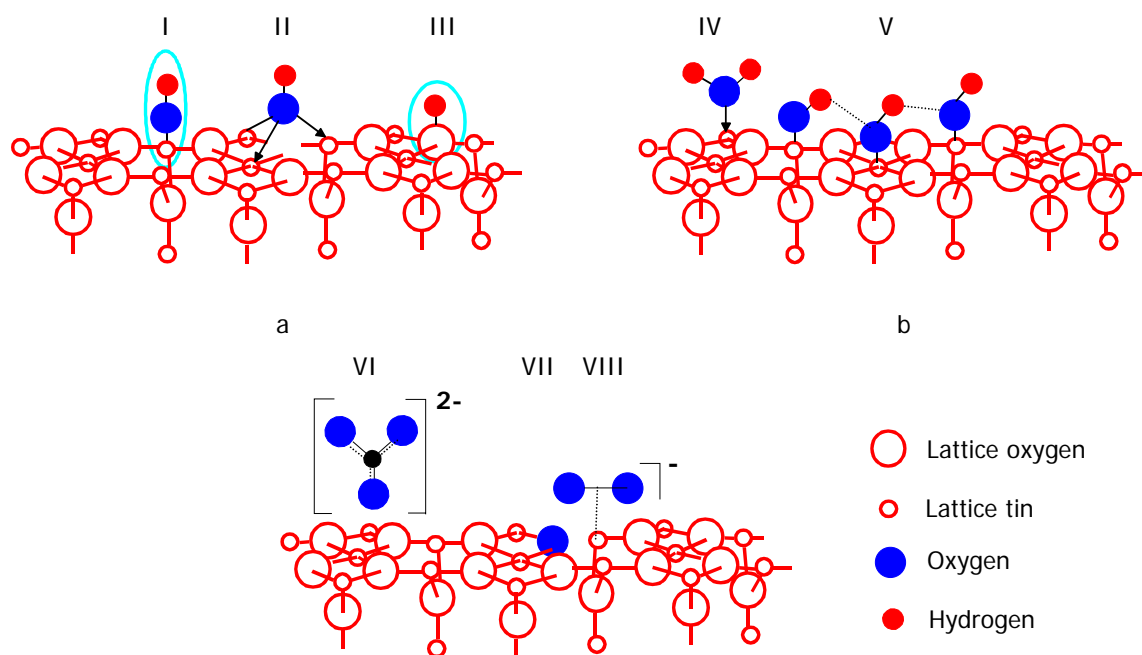


Figure 4.2: Pictorial presentation of different species on the tin oxide surface.
 a) I and II. Differently coordinated terminal hydroxyl groups; III. Rooted hydroxyl groups; b) IV. Coordinated water; V. Associated hydroxyl groups; c) VI. Free carbonate-ions VII. Chemisorbed oxygen in the lattice; VIII. Oxygen ion stabilised on tin atom.

In the range between 2700 and 2000 cm^{-1} in the spectrum (not shown here) a very broad band was observed. According to [6], the band with the band maximum at 2350 cm^{-1} corresponds to a Zundel structure, H_5O_2^+ ions, (from the literature, the vibration modes of H_5O_2^+ ions are: $2990\text{-}2850\text{ cm}^{-1}$, $2250\text{-}2200\text{ cm}^{-1}$, $1705\text{-}1660\text{ cm}^{-1}$, $1000\text{-}900\text{ cm}^{-1}$). The positions of these bands depend on the counter ion (anion). According to the same reference, H_3O^+ ions show a broad band around 2600 cm^{-1} which is also detected here on the various SnO_2 powders (the vibration modes of H_3O^+ ions are: $3380\text{-}3150\text{ cm}^{-1}$, $2650\text{-}2468\text{ cm}^{-1}$, $1705\text{-}1670\text{ cm}^{-1}$, 1125 cm^{-1}).

In the low wavenumber region (between 2000 and 1000 cm^{-1}) of the spectrum one finds several absorption bands at 1814 , 1644 , 1367 , 1293 , 1256 , 1217 , 1067 cm^{-1} . These bands are attributed to surface carbonate species, the deformation mode of hydrated proton species, the deformation mode of hydroxyl groups and metal-oxygen vibrations on the surface.

In the following, different vibrations of various oxygen species will be discussed in detail, since they play different roles in the sensing mechanism. Many oxygen experiments were conducted on different metal oxides in different conditions, in order to characterise possible surface oxygen species, described in the literature (Davydov [36] and Lenarts [24] on SnO₂, Zecchina on Cr₂O₃ [23]). After oxygen exposure, in all studies several bands were obtained between 1400 and 850 cm⁻¹ depending on the treatment and oxide structure. For example, Lenarts et al. reported the exposure of the SnO₂ surface to O₂/N₂ resulting in bands at 1370, 1266, 1222, 1140, 1068, 1020, 970, 930, 885 cm⁻¹. Davydov et al. performed their oxygen experiments on a tin oxide surface reduced with CO. In the infrared spectra they detected three absorption bands at 1045, 1133 and 1190 cm⁻¹.

According to these investigations, three kinds of oxygen vibrations were found in the IR spectra. One vibration is between metal and oxygen in the lattice (bulk). The frequency of this vibration is in the so called "fundamental frequency region" of the spectra. The corresponding absorption bands occur in the spectrum at 670, 610, 312 cm⁻¹ (not observed in our work because of the detector limitation, cut-off of the MCT detector is at 630 cm⁻¹). The second vibration is between metal and oxygen at the surface. Since there are defects on the surface the frequency of the vibration shifts to higher wavenumbers, in the so called "region above the fundamental frequency", namely at 1060 and 970 cm⁻¹ [21, 23, 36]. Bands at 1060 and 970 cm⁻¹ were assigned to metal-oxygen groups of an ionic nature on oxide surfaces which are equivalent to oxygen ions adsorbed on metal cations. The frequency of the surface M-O vibration depends on the coordination number of the metal atoms. The decrease of the coordination number of the metal atoms at constant valence causes the reduction of the bond distances and increases the number of valence electrons per single bond (increase of the bond multiplicity) and accordingly, bond strength and frequency increase.

The third type of vibration results from the adsorption of the molecular form of oxygen [21, 36]. Davydov demonstrated the detection of molecular radical-ion forms of oxygen adsorption on the reduced oxide surfaces using IR and ESR method. According to these investigations, the frequencies of ν_{O-O} in molecular charged ions (O_2^-) appear in the spectral region between 1190 and 1045 cm^{-1} , which overlaps with the absorption band at 1060 cm^{-1} corresponding to the M-O vibration on the surface, and the O_2^- ions are stable up to 200°C. Above these temperatures O_2^- transforms to chemisorbed O^{2-} , building a vibration of M-O bonds as described in chapter 2.10 and shown in Figure 4.2-VII. The bands at 1190 and 1045 cm^{-1} were assigned to O_2^- -ions stabilized on Sn^{2+} atoms ($\nu_{O-O}=1045\text{ cm}^{-1}$) and O_2^- -ions stabilized on Sn^{4+} ($\nu_{O-O}=1190\text{ cm}^{-1}$). The same CO experiments were performed on a defectless tin oxide sample. The spectrum was much more complex than the spectrum of the reduced one. Several absorption bands were detected between 1140 and 1090 cm^{-1} which were assigned to either molecular forms of O_2^- stabilised on Sn^{3+} or more complex oxygen species like O_3^- , O_4^-).

In the experiments for this research performed on various tin oxide powders absorption bands at around 1045 cm^{-1} (a broad absorption including several absorption bands) and at 1133 cm^{-1} (as shoulder) were detected. These absorption bands are in very good agreement with the absorption bands observed in the literature [23, 36, 37]. Thus the assignment of these absorption bands are taken from the literature, since no oxygen experiments on tin dioxide powder were performed in this work and our spectra show similar spectral features. A further indication for a true assignment of this band was found by the recording of the time resolved spectra on powder in the presence of CO at RT (see Chapter 4.1.4.1).

Old commercial tin oxide powder.

The spectrum of the commercial powder, which was stored for months under laboratory atmosphere, shows the same absorption bands but with different intensities (see Figure 4.1, top, short dotted line). Between 4000 and 3000 cm^{-1} , the intensities of different OH groups are lower than that of the OH groups on the fresh commercial powder. In the spectra of this powder mainly coordinated water was observed, the amount of which is low. The broad band between 2700 and 2000 cm^{-1} and the bands in the low wavenumber region (2000-1000 cm^{-1}) are more intensive than in the case of the fresh commercial powder. The long storage time of the samples accounts for more hydrated proton species and carbonates.

Sg1 powder.

The spectral characteristics of sg1 are very different in the region between 4000 and 3000 cm^{-1} (Figure 4.1, top, the "short dashes-dots" line). Here, very broad bands of liquid water, ordered layers of water molecules and coordinated water were observed between 3500 and 3000 cm^{-1} ($\nu_{\text{water}} = 3400\text{-}3500 \text{ cm}^{-1}$). The broad band at 3572 cm^{-1} corresponds to two dimensional hydrogen bonded hydroxyl groups (see Fig. 3, dash-dotted line). Their intensity was not affected by evacuation.

In the other regions, the bands observed for the carbonate ions and the different vibration modes of the hydrated proton are also present at the same positions as for the fresh commercial powders but with much lower intensities.

Sg2 powder.

In contrast to sg1 (Figure 4.1, top, the "short dashed" line), the spectrum of sg2 shows very intense and sharp OH group bands nearly at the same frequencies as in the case of the fresh commercial powder. Only the intensity distribution is different. Bands corresponding to coordinated water, ordered layers of water molecules or liquid water are not present in the spectrum.

The bands of hydrated protons are the most intensive. The broad band between 2600 and 2000 cm^{-1} is visibly well separated in single bands with the maxima at about 2400 and 2200 cm^{-1} (not shown here). The band at about 1050 cm^{-1} corresponds to the broad band consisting of more than one component (ν_{defH3O^+} , ν_{defH5O2^+} , ν_{CO_3} , etc.). Also the bands between 1400 and 1200 cm^{-1} are more intensive than in the case of other samples.

4.1.2 Characterisation of Un-doped and Pd-doped Sensors at RT

In order to avoid artefacts, single channel spectra are presented in this chapter. The reason for this presentation is the difficulty of finding a reference, since alkali halides could not be put on the substrate by screen printing. It was attempted in this work, but at high temperatures the surface structure was completely destroyed. For a good comparison of the spectra of the sample and the reference the same surface texture is needed. Nevertheless, all expected bands can be seen in the single channel spectra.

Figure 4.3 shows the single channel spectra of un-doped and Pd-doped sensors recorded at RT in dry air in the full spectral range (4000-850 cm^{-1}). Several sharp absorption bands can be seen in the spectral range between 4000-3000 cm^{-1} and 1500-850 cm^{-1} . The spectral range between 3000 and 2000 cm^{-1} discussed on the powder is not presented here, since the background caused by the optics dominates the single channel spectrum.

The single channel spectra of both materials at RT are very similar. Only the intensity distribution of the bands is different and bands in the spectrum of the un-doped material are sharper than in the case of the Pd-doped one. In the following, for a better characterisation and understanding, individual spectral ranges will be presented and discussed.

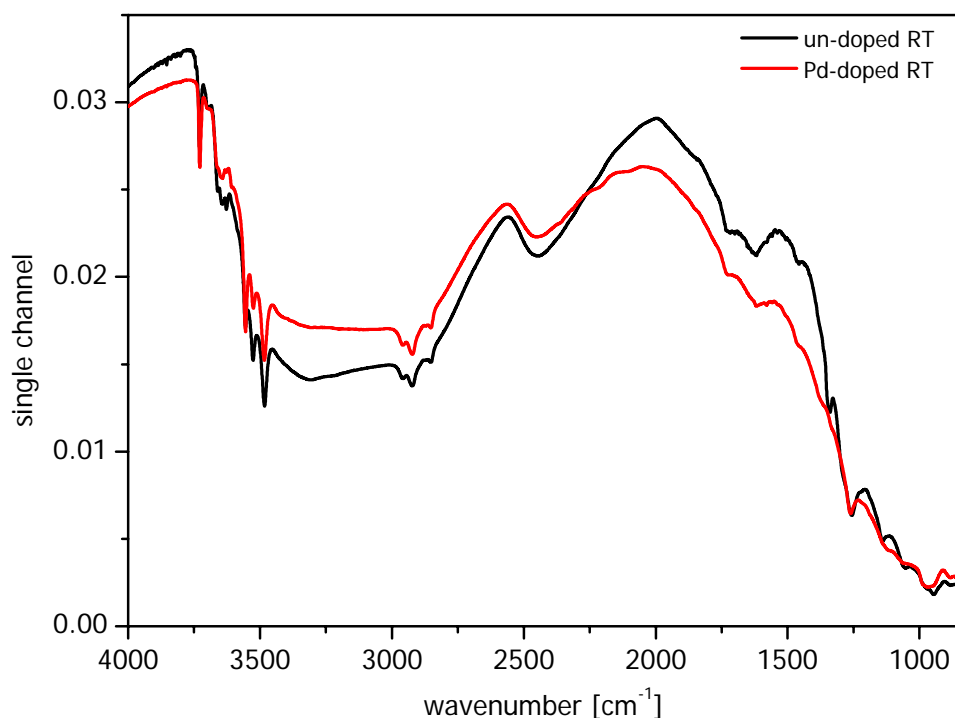


Figure 4.3: Single channel spectra of an un-doped and a Pd-doped sensor recorded at RT in dry air in the full spectral range (4000-850 cm^{-1}).

Spectral range between 4000 and 3000 cm^{-1} :

In this spectral range bands at 3659, 3644, 3628 cm^{-1} are assigned to terminal hydroxyl groups and bands at 3555, 3527, 3483 cm^{-1} are assigned to rooted OH groups on the basis of powder measurements (Figure 4.2 a). Comparing the spectra of sensors (sensing layer with 10 nm grain size) with the spectra of the sol-gel prepared powder of the same grain size, one can see that the structures of the spectra, especially in the 4000-3000 cm^{-1} range, differ strongly from each other, whereas, the spectra of the sensor with the grain size of 10 nm are in very good agreement with the spectra of the sol-gel powder with the grain size of 100 nm (sg2). Only the band at 3729 cm^{-1} observed on both kinds of sensors was not seen on any of the investigated powders (Figure 4.4).

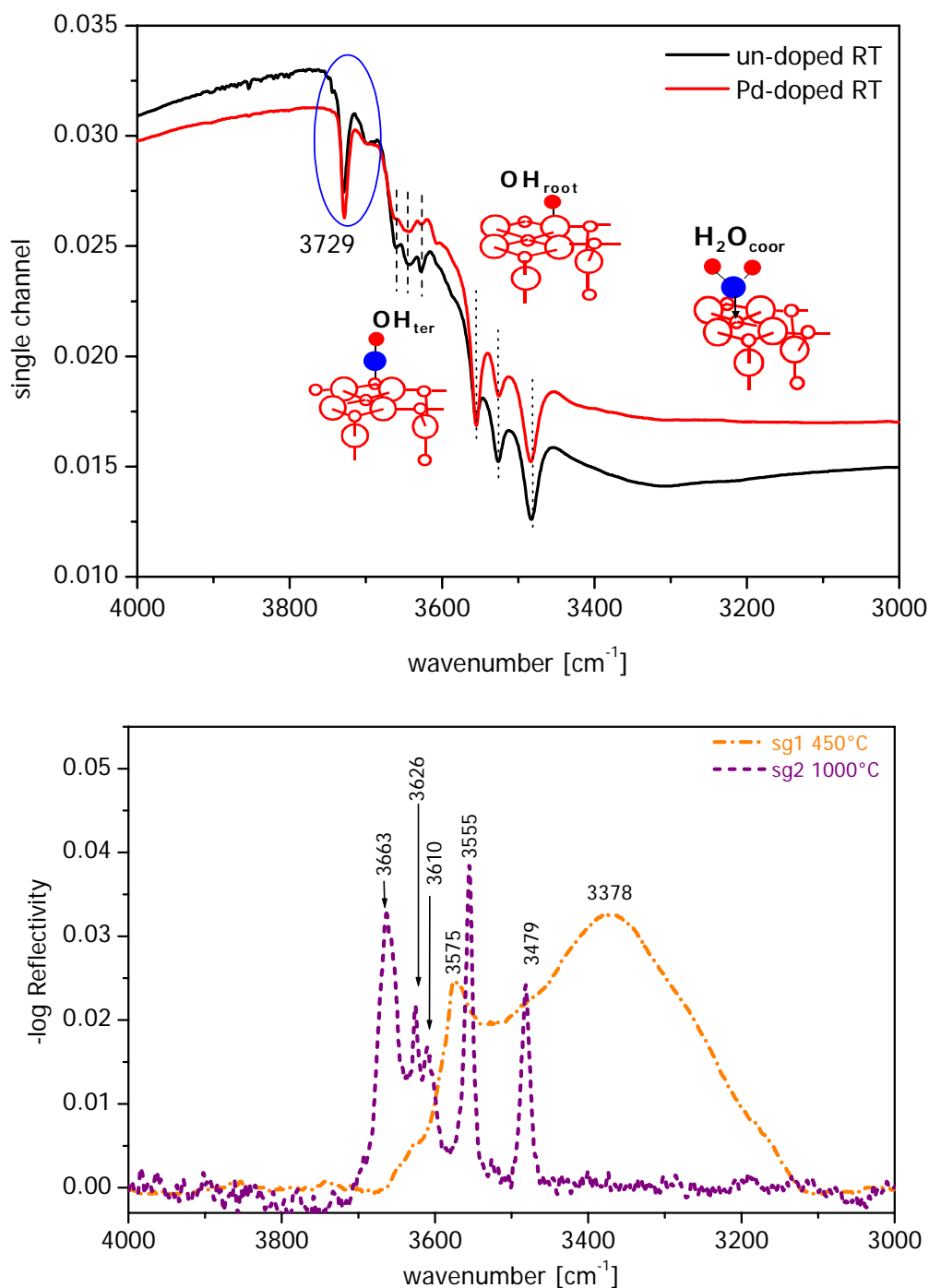


Figure 4.4: Spectra of un-doped and Pd-doped sensor recorded at RT in synthetic air in the spectral range between 4000 and 3000 cm⁻¹ (top). Spectra of sol-gel prepared powder with the grain size of 10 nm (sg1) and with the grain size of 100 nm (sg2) recorded at RT under vacuum in the spectral range between 4000 and 3000 cm⁻¹ (bottom).

The band at 3729 cm⁻¹ assigned to terminal OH groups (Sn-OH) was observed in the literature only on SnO₂ powders prepared by a very specific preparation method using hydrazin. By this preparation the average grain

size is about 3 nm [57, 58]. On the other hand, in several studies bands between 3800-3635 cm^{-1} were observed on Al_2O_3 [46, 101]. However, in the spectra recorded on the bare alumina substrate (see below) no bands in the OH range were detected. Therefore, this band must be created either in the interface between substrate and sensitive layer by the screen-printing process or the sensitive layer contains grains of a size smaller than the average of 10 nm.

The broad band between 3420 and 3000 cm^{-1} is assigned to coordinated water molecules and ν_{OH} vibrations corresponding to either H-bonded Sn-OH species [57, 43] or hydroxyl groups multiply bonded to adjacent Sn sites [57, 99, 100, 102].

Spectral range between 2000 and 850 cm^{-1} :

In the spectrum of the un-doped sensor the bands in this spectral region are sharper than in the case of the Pd-doped one. In the spectral range between 2000 and 850 cm^{-1} several bands at 1461, 1340, 1285, 1260 1141, 1054, 979 and 943 cm^{-1} were detected (Figure 4.5).

Especially, the band with the maximum at 1340 cm^{-1} in the spectrum of the un-doped material is hardly observable in the spectrum of the Pd-doped sensor. Since in this spectral range different modes of several compounds are overlapping, it is difficult to make an assignment of the bands. Bands at 1340, 1285, and 1260 cm^{-1} are assigned to the deformation mode of the different hydroxyl groups. A broad band with the maximum at around 1620 cm^{-1} is the deformation mode of water [43].

The absorption band at 1461 cm^{-1} is characteristic for the vibration of free carbonate [76, 81, 112].

Bands at 1141, 1054 cm^{-1} were assigned to the molecular adsorbed form of oxygen in form of radicals stabilised on Sn^{3+} and Sn^{2+} ions. Bands at 979 and 943 cm^{-1} were assigned to surface oxygen ($\text{Sn-O}_{\text{surf.}}$).

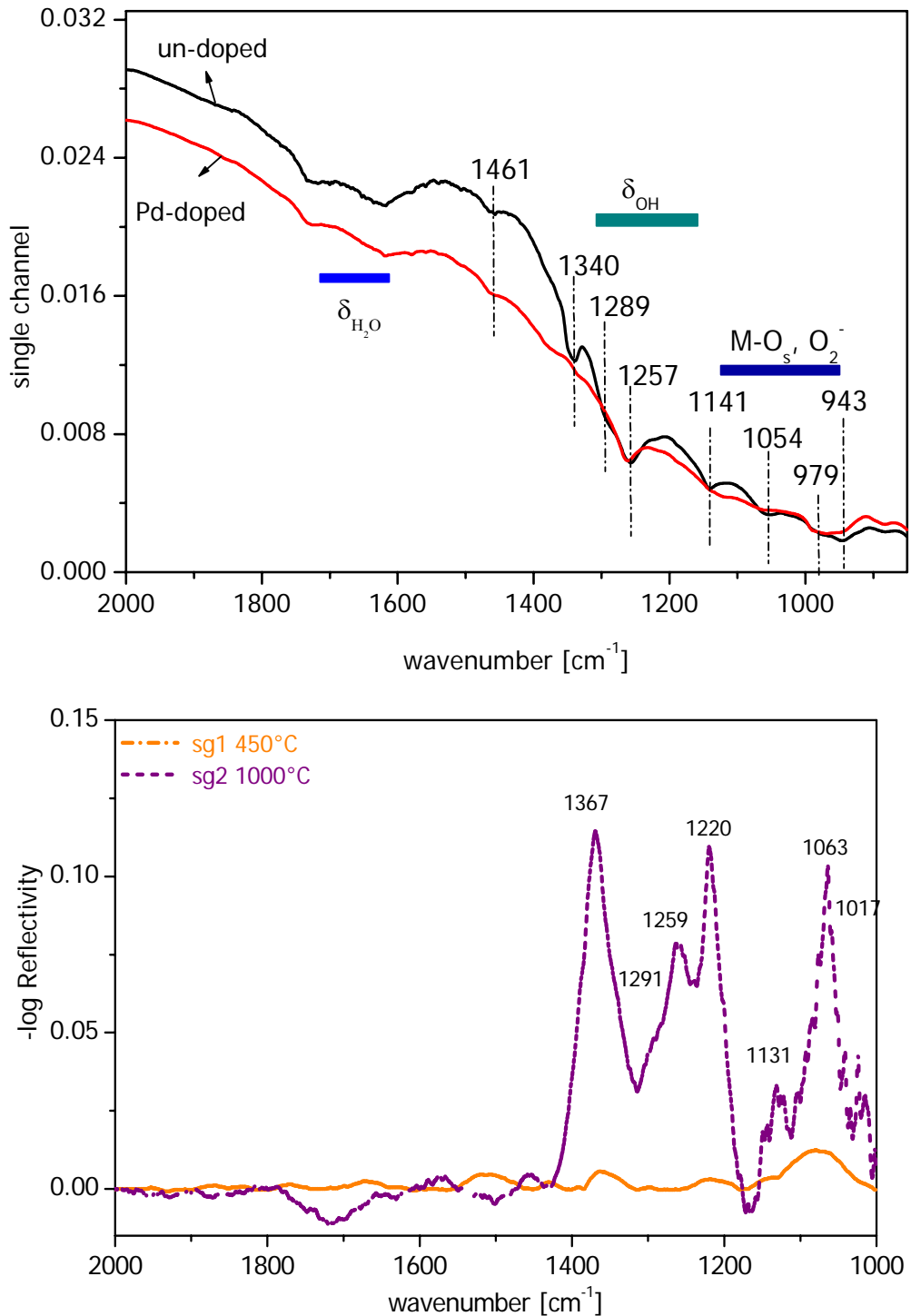


Figure 4.5: Spectra of un-doped and Pd-doped sensor recorded at RT in synthetic dry air in the spectral range between 2000 and 850 cm⁻¹ (top). Spectra of sol gel prepared powder with the grain size of 10 nm (sg1) and with the grain size of 100 nm (sg2) recorded at RT under vacuum in the spectral range between 2000 and 1000 cm⁻¹ (bottom).

4.1.3 Temperature Effects

Heating and cooling ramps in dry air were applied between RT and 350°C for both sensors, in order to determine the influence of the temperature on the surface structure. The temperature steps were 50°C with equilibrium time period of one day between successive steps. Before the temperature ramp the sensor was thermally treated in the oven (see chapter 3.7) and heated for about one week at 300°C in air in the laboratory.

4.1.3.1 Un-doped Sensor

Figure 4.6 shows the single channel spectra recorded at different temperatures (RT, 150, 300 and 350°C) in dry synthetic air. With increasing temperature a dramatical change of the spectra was observed over the complete spectral range. Looking over the total spectral range general changes in the band structure and intensities are observable.

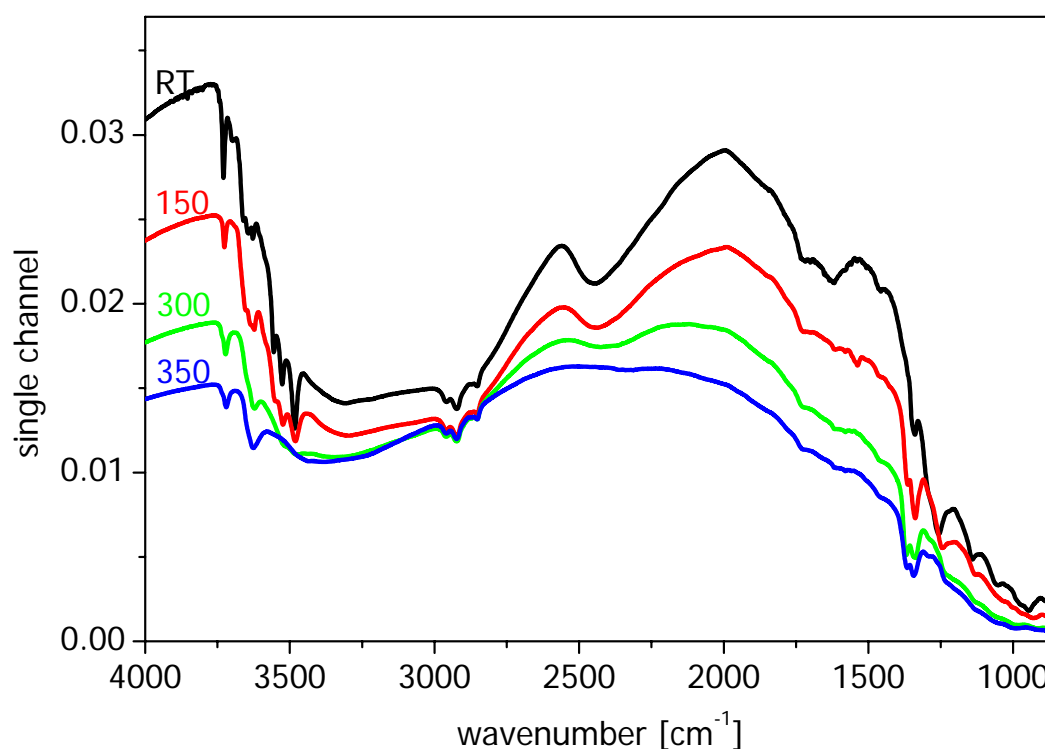


Figure 4.6: Single channel spectra of un-doped sensor at different temperatures (RT, 150, 300, 350°C) in dry air in the spectral range between 4000 and 850 cm⁻¹.

In the following two spectral ranges, namely 4000-3000 cm^{-1} and 2000-500 cm^{-1} will be shown and discussed in detail for a better observation of the changes on the molecular level. Figure 4.7 presents these two spectral ranges of the un-doped sensor at different temperatures in dry air.

Increasing the temperature leads to the following changes in each spectral range:

In the spectral range between 4000 and 3000 cm^{-1} :

- The absorption at 3729 cm^{-1} shifts to lower wavenumbers (at 350°C, 3719 cm^{-1}), becomes broad and the intensity of this band decreases;
- Terminal OH groups lose their intensity very slowly. Starting at about 200°C a new terminal OH group forms at 3623 cm^{-1} ;
- The band intensities of the rooted OH groups decrease continuously. Around 200°C the triplet structure is not identifiable and at 350°C they vanish (or shift to lower wavenumber) completely. At 350°C a very broad band at about 3400 cm^{-1} appears in the spectra assigned to ν_{OH} vibrations corresponding to either H-bonded Sn-OH species [43, 57], or hydroxyl groups multiply bonded to adjacent Sn sites [57, 99, 100, 102]. The intensity of the differently bonded water (coordinated, molecular water) also decreases. However, rebuilding of the surface rooted hydroxyl groups (at 3481 and 3555 cm^{-1}) was detected during the CO measurements on sensors in the presence of humidity and at higher temperatures (300 and 350°C, see 4.1.4.2.2).

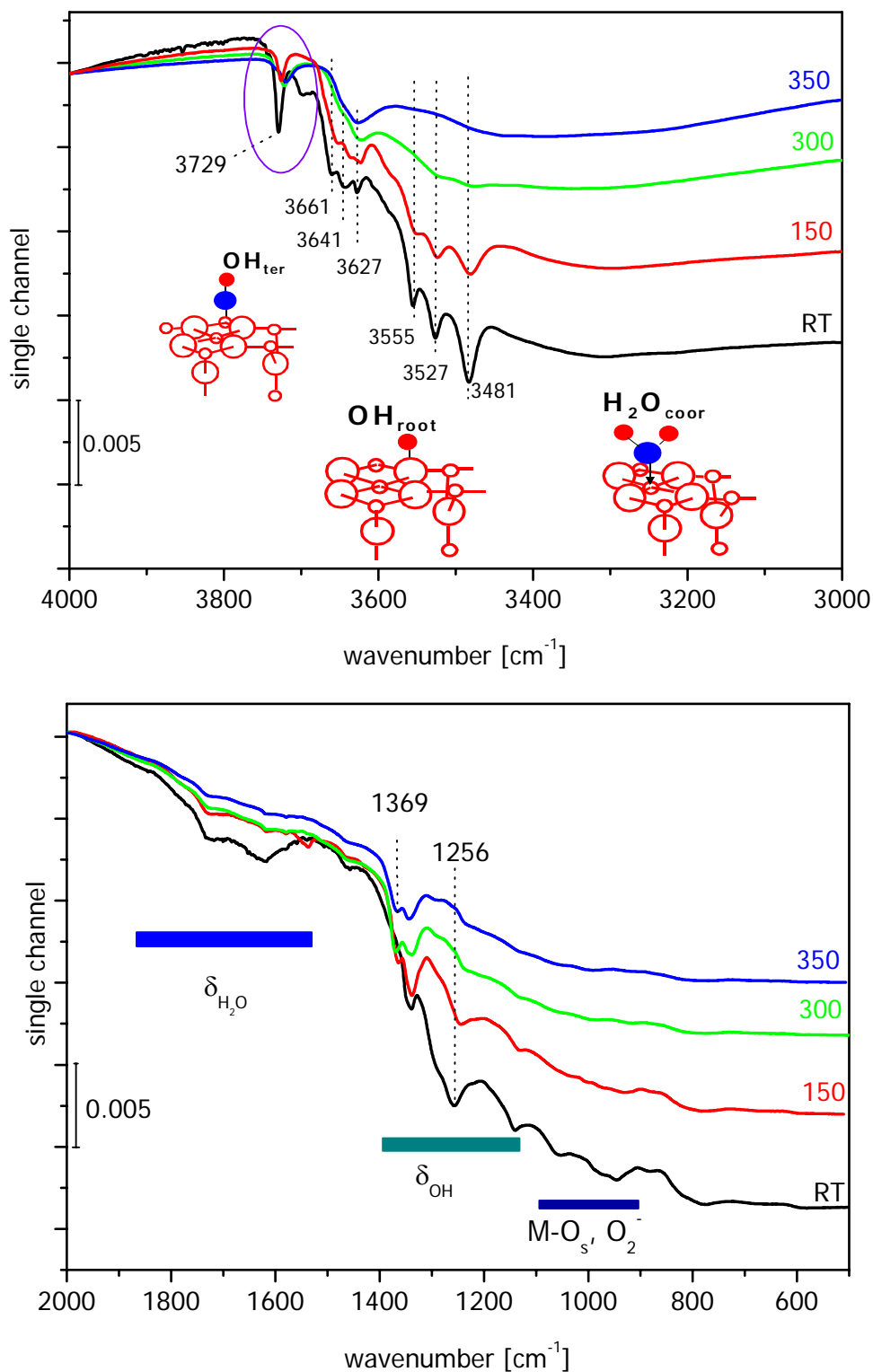


Figure 4.7: Two spectral ranges of un-doped sensor recorded at various temperatures in dry air (RT, 150, 300, 350°C). Top: Spectral range 4000-3000 cm⁻¹. Characteristic vibration of hydroxyl groups and water related species appear in this region. Bottom: Spectral region 2000-500 cm⁻¹, where bands corresponding to bending mode of OH/H₂O, carbonate like species and surface oxygen species appear.

In the spectral range between 2000 and 850 cm⁻¹:

- The intensity of the band corresponding to the deformation mode of water decreases;
- In the spectral range between 1400 and 1200 cm⁻¹, the band with the maximum at 1369 cm⁻¹, which was existing probably as shoulder can be clearly seen in the spectrum. Comparing the evolution of the absorption bands in this spectral range with the OH spectral range shows parallels, which leads to the assignment that these bands present the deformation mode of the hydroxyl groups;
- First a shifting, then a broadening of the bands corresponding to different oxygen species (1200-850 cm⁻¹) was observed. As mentioned above the deformation mode of the hydroxyl groups and the stretching vibration mode of the oxygen molecular ion are partly overlapping. Therefore, the exact assignment of the absorption bands is very difficult and additional measurements (like oxygen ¹⁶O, ¹⁸O and D₂O measurements) are needed for correct assignments.

Shifting of the bands (between 4000 and 3000 cm⁻¹) to lower wavenumbers with the increasing temperatures might be caused by the interaction of hydroxyl groups with the molecular adsorbed form of oxygen ions (see Figure 2.10), since a broadening of the bands was observed in the spectral range where the molecular adsorbed oxygen appears (in the range between 950-1300 cm⁻¹).

In the cooling ramp, all bands were redetected, but with much lower intensities. At the moment, the reason of this reproducible rearrangement of the surface species, especially absorption bands corresponding to the surface hydroxyl groups, depending on the temperature is unclear.

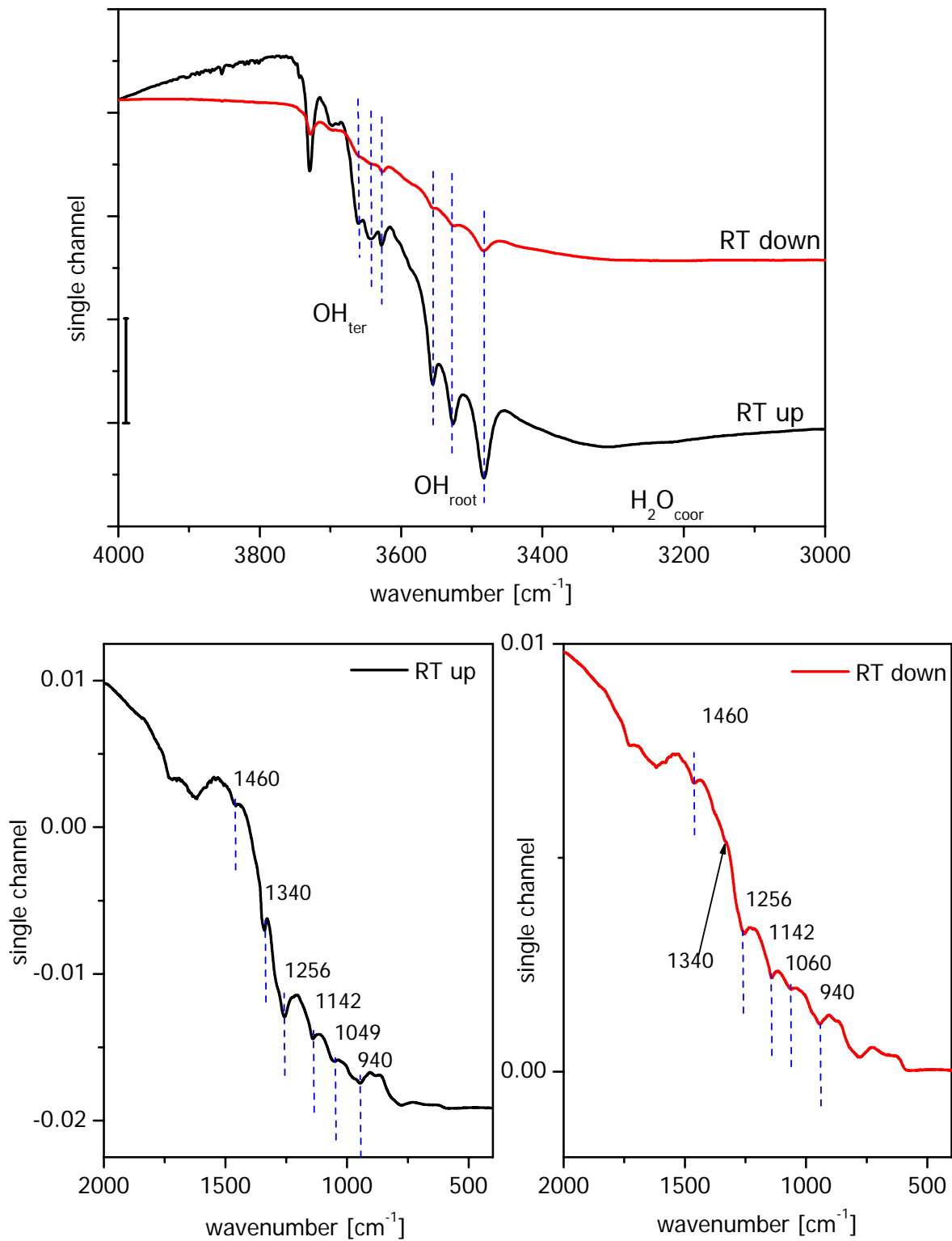


Figure 4.8: Effect of temperature cycle on the surface species. Spectra of un-doped sensor at RT in dry air before heating up to 350°C and after cooling down to RT.

4.1.3.2 Pd-doped Sensor

Figure 4.9 shows some selected single channel spectra of Pd-doped sensor recorded at various temperatures between RT and 350°C in dry air.

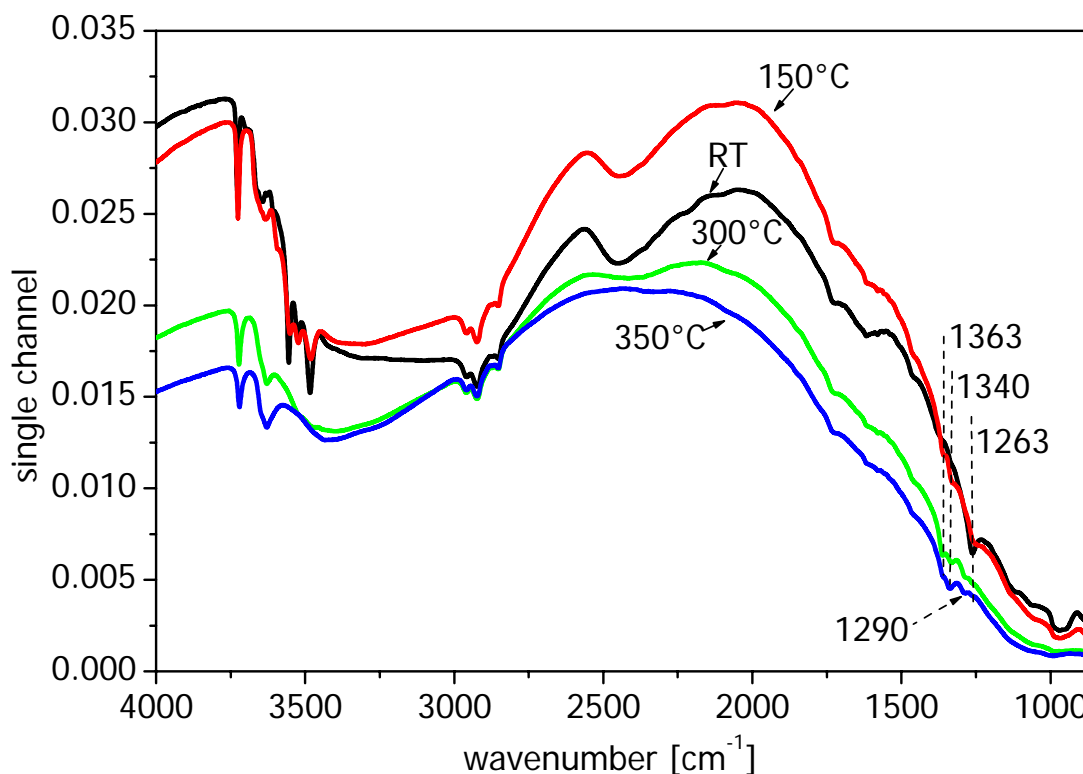


Figure 4.9: Single channel spectra of the Pd-doped sensor at different temperatures in dry air.

During the temperature cycle, very similar changes in the spectra of the Pd-doped sensor were observed during the temperature cycle like on the un-doped sensor. With increasing temperature, both bands detected at 1340 and 1365 cm^{-1} at RT on the un-doped sensor appear also on the Pd-doped sensor.

Over the full spectral range, no Pd related signal was detected.

4.1.3.3 Substrate

Additional to SnO_2 thick film sensors the Al_2O_3 substrate provided only with a Pt-electrode was characterised at different temperatures (Figure 4.10).

In the single channel spectrum of the substrate recorded in dry air the asymmetric vibration mode of gaseous CO₂ was observed. Since the presence of gaseous CO₂ in the sample chamber and spectrometer is out of the question, the gaseous CO₂ must be in the pores of the substrate.

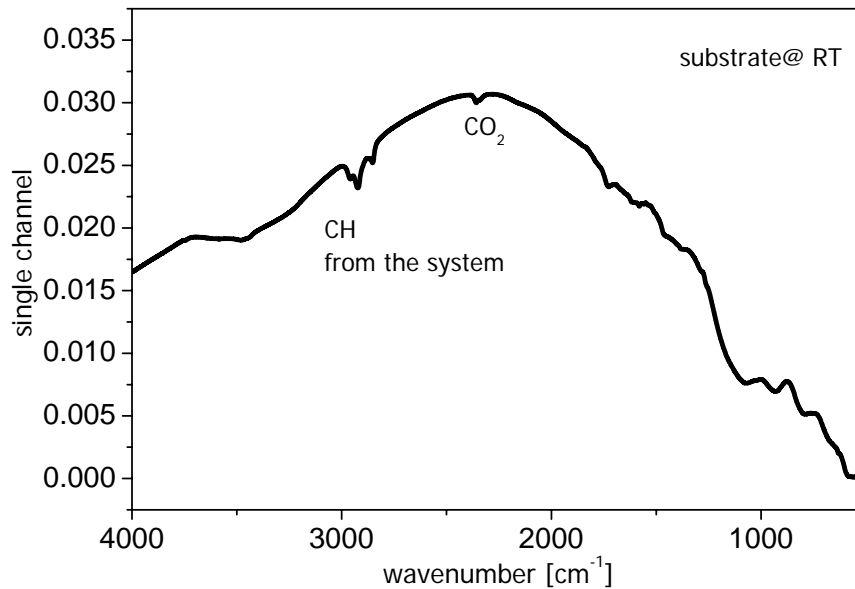


Figure 4.10: Single channel spectrum of Al₂O₃ substrate at RT.

Investigations at higher temperatures show an increase of the PR distances (Figure 4.11, left) due to the Boltzmann statistics, but no changes of the rotational constant B. Gaseous CO₂ was also observed on the sensor. The PR distances in the spectrum of substrate and sensor are different (Figure 4.11 right). By means of PR distances, the temperature of the surface is:

$$T_{cal} = \frac{h \cdot c \cdot (\tilde{\nu}_R - \tilde{\nu}_P)^2}{8 \cdot k \cdot B}$$

Whereby:

h : Planck constant,

c : speed of light ,

k : Boltzmann constant,

B : rotational constant,

$\tilde{\nu}_P, \tilde{\nu}_R$: maxima of the P and R rotation vibration bands.

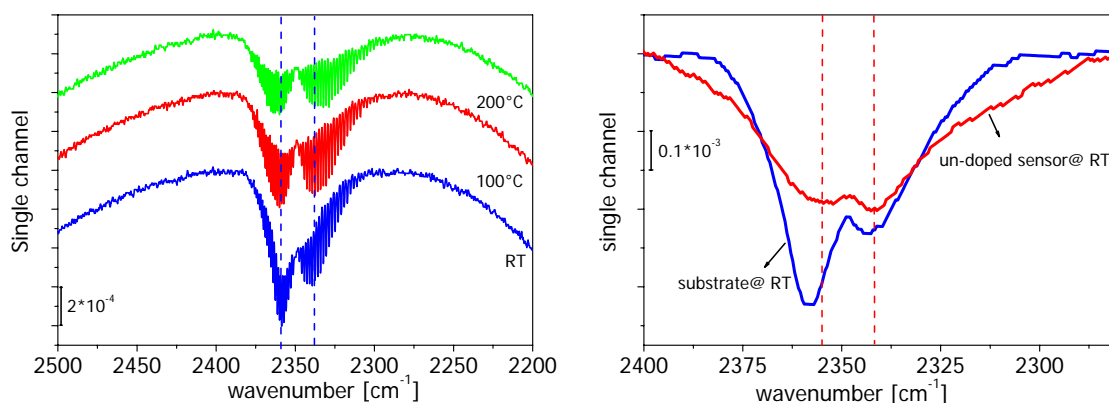


Figure 4.11: Left: DRIFT-spectra of the alumina substrate with higher resolution in the spectral range between 2500 and 2200 cm⁻¹. Right: Comparison of the spectra of the substrate and sensor in the CO₂ spectral range.

Table 5 shows the PR distances of CO₂ and calculated temperatures of the substrate, sensor and in the gas cell (at RT) [103].

Table 5: PR distances in the vibration rotation spectra of CO₂ at RT and at 498 K measured on SnO₂ sensor, Al₂O₃ and in a gas cell. The calculated temperatures deviate from the set temperatures.

Sample	T _{set} [K]	ΔPR [cm ⁻¹]	T _{cal} [K]
SnO ₂	298	12	67
Al ₂ O ₃	298	20	184
Gas	298	25.5	298
Al ₂ O ₃	498	29	385

One can see in Table 5 that the PR distances on the sensor and substrate at RT differ from that of CO₂ measured in the gas cell. Accordingly, at higher temperatures, the calculated temperature is much lower than the set temperature. The calculated temperature is an *apparent* temperature. The PR distances vary also in SnO₂ and the substrate, probably because of the different pore sizes (Figure 4.11 right) of the material. One can imagine that the rotation of the molecules is hindered like in viscous media. This hindrance becomes especially noticeable in the occupation of higher excitation states. These states are not as strongly occupied at higher

temperatures as expected. Therefore, the distance between the maxima of the PR branches are smaller than in the case of free CO₂ in the gas cell, corresponding to a lower temperature.

It should be noted that DRIFT measurements on several Al₂O₃ substrates and SnO₂ sensors were performed. Although the synthetic air used in the measurements was of the same quality (even the same bottle), gaseous CO₂ was not detected on all samples. Most probably it depends on the history of the sample (storage atmosphere).

Gaseous CO₂ and H₂O in the pores or channels were identified also in other studies using high temperature infrared spectroscopy on minerals like beryl and cordierite. Rossman et al. [12] reported that structurally bound water in the pores starts to partition into an unbound state with the characteristics of a gas above 400°C. The authors found that the process is fully reversible and the dehydration occurs after most of the water is in the unbound state. Another observation was that whereas all water molecules were released, 40% of CO₂ remained after heating to 800°C. This result confirmed our interpretation, since measurements in this study were performed between RT and 350°C.

A second explanation for our assumption, the CO₂ being in the pores, is that the concentration of CO and CO₂ is too low to be detected in such a small sensor chamber. In order to detect low concentration of gases, long gas cells (20-25m pathway) are generally needed.

4.1.3.4 Summary of Characterisation

Un-doped, Pd-doped sensors and alumina substrate were characterised at different temperatures (RT-350°C) over the middle infrared spectral region (4000 and 850 cm⁻¹). On both sensor types different types of isolated hydroxyl groups (terminal and rooted), associated hydroxyl groups, water and different oxygen species were detected. The intensity distribution of the surface species on both sensors is different. Except for the band at

3729 cm^{-1} all bands could be assigned. On the sensors, no bands corresponding to carbonate like species were detected, which were observed on differently prepared tin dioxide powders at RT. On the substrate only CO_2 in the gas phase as surface impurities in the pores of the material was detected. Although the results obtained on sg1 and on the sensor (the sensitive layer of the sensor is the sg1 powder) show a very different structure, in general the results obtained by direct measurements on the sensor at room temperature are largely in agreement with the results obtained on powders in earlier experiments conducted for this research and those found in the literature.

With increasing temperature a rearrangement of the surface species on the tin oxide surface of both types of sensors was observed, which is the cause for the changes in the sensor resistance. An exact description of this rearrangement (especially in the OH spectral range) could not be drawn. Additional in-situ measurements are needed for a better understanding of the rearrangement. Anyhow, obviously this easy reorganisation of the surface species is favourable for the CO reaction, which causes changes in the sensor resistance. During the cooling process the same bands detected in the heating-up process are returning to the same position with the same structure but with lower intensity and different intensity distributions. During the temperature experiments, the sensor resistance - determined by the surface net charges due to surface species - changes due to the changes of the surface structures (rearrangement of the surface species). On the other hand, in the cooling step the sensor resistance has a different value than at the heating steps, which is caused by the concentration of the net charge changes during the thermal treatment.

4.1.4 CO Measurements

4.1.4.1 CO Measurements on the Commercial Tin Dioxide Powder at RT

The fresh commercial powder was brought in contact with pure (99.8%) CO for 50 minutes (the valve was closed, and afterwards the sample was kept in the same conditions for another hour). Immediately after the exposure the following changes in the spectra were observed:

- A continuous decrease of the bands at 3638 and 1217 cm^{-1} corresponding to the stretching and bending mode of hydroxyl groups;
- An extremely fast decrease of the bands at 1367 and 1067 cm^{-1} corresponding to the free carbonate and surface oxygen species (the band at 1067 cm^{-1} has not completely vanished);
- An increase of the broad band corresponding to hydrated protons;
- The formation of new bands at about 2200 cm^{-1} ; and
- The formation of bands at 1584, 1512, 1268 and 1224 cm^{-1} .

Figure 4.12 shows the intensity changes of water related species appearing in the spectrum between 4000 and 3000 cm^{-1} in the presence of CO. The top diagram shows the spectra in equilibrium situations and the bottom one shows the spectra recorded during the CO exposure (time-resolved spectra). The time resolved spectra and a quantitative band analysis revealed that only the band corresponding to terminal OH groups at 3638 cm^{-1} was influenced quite dramatically in the presence of CO while the intensity of other hydroxyl groups was not influenced. This species was also proved to be a very active surface site in the experiments dealing with exposure to deuterated water [50], not shown here. Furthermore, CO exposure to the SnO_2 surface leads to a reduction of the band intensity of the broad band (3362 cm^{-1}) assigned to the associated hydroxyl groups and coordinated water and one observes a shift of the band maximum to lower wavenumbers (3280 cm^{-1}).

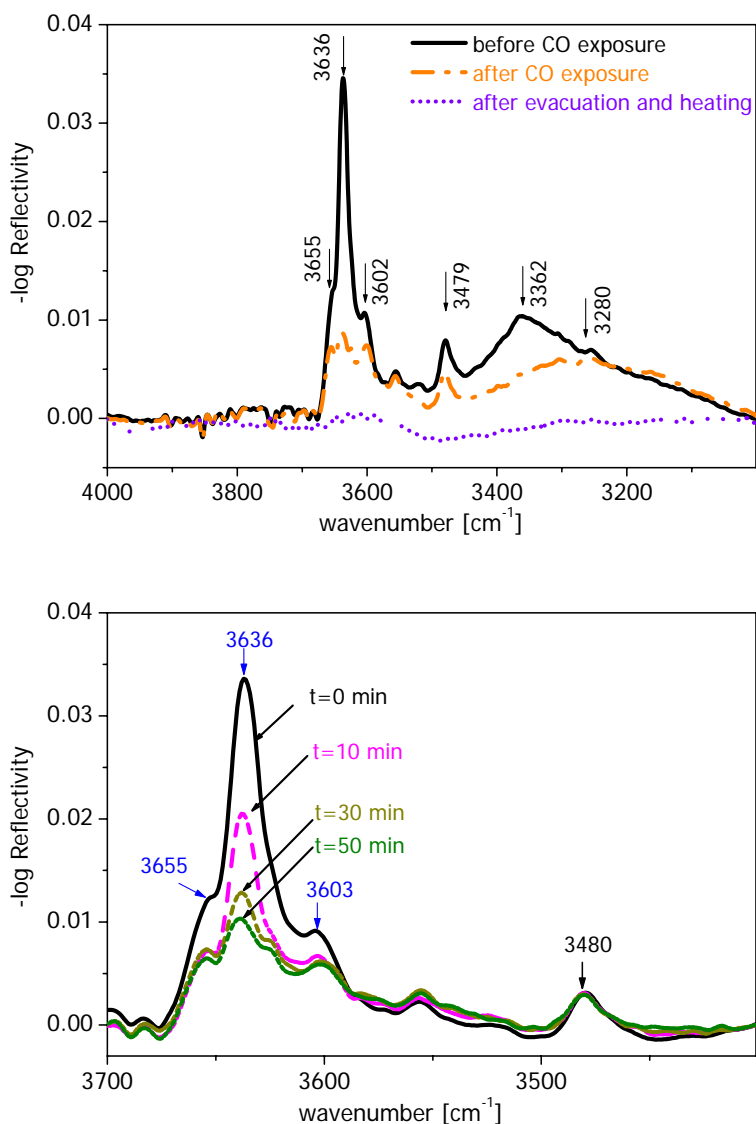


Figure 4.12: Top: Spectra in OH spectral range recorded before CO exposure, after one hour of CO exposure and after heating in vacuum. Bottom: Time resolved spectra during CO exposure.

In the intermediate wavenumber range, at about 2200 cm^{-1} , a new band was formed, which vanished after evacuation (Figure 4.13, top). Since this band vanishes by evacuation, it can be ascribed to physisorbed CO. The time resolved spectra (Figure 4.13 bottom) show changes in both the band structure and the position of the band maximum during the CO exposure. By the studies of CO adsorption on pure $\text{Al}_2\text{O}_3\text{-TiO}_2$ surfaces, Knözinger [104] reported an increase of CO concentration leads to a shift of the band maximum and the creation of new bands. The bands at 2203, 2193 and

2180 cm^{-1} can be assigned to CO coordinated to Sn^{4+} acid sites having differing acidities. The band analysis shows that CO adsorbs on the surface according to a Langmuir isotherm and the process stabilizes after 25 minutes (Figure 4.14).

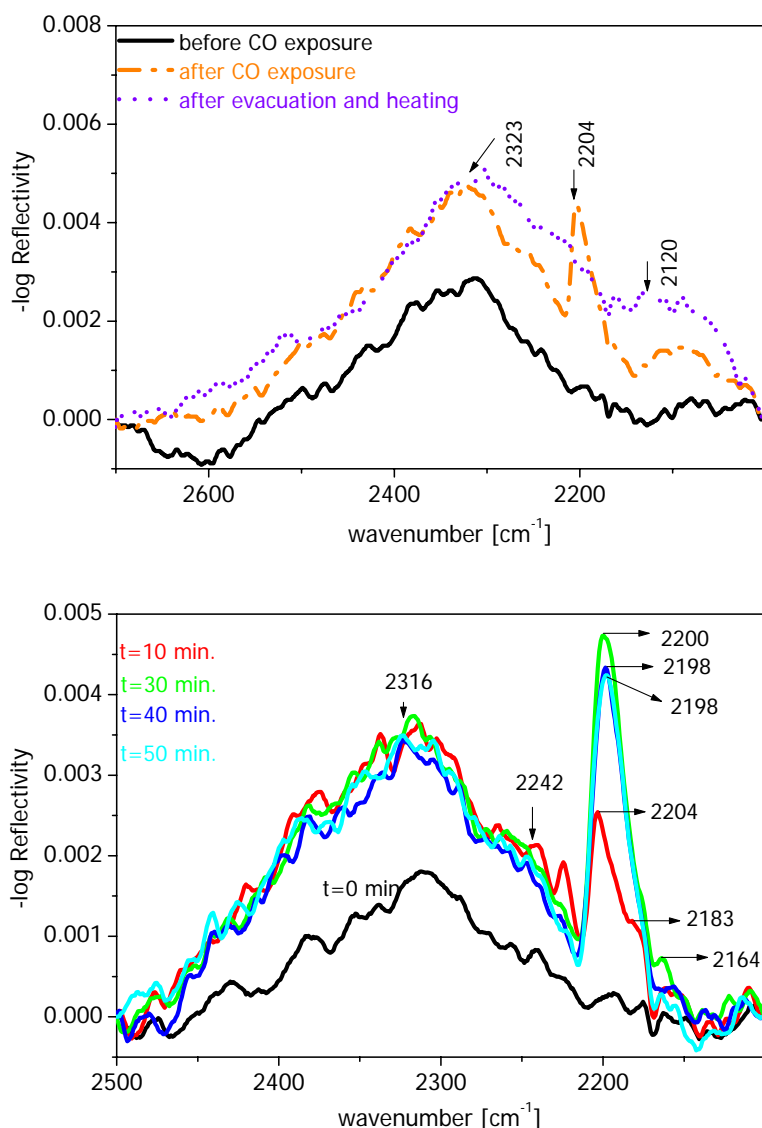


Figure 4.13: Top: Middle spectral range before and after one hour of CO exposure. Bottom: Time resolved spectra during CO exposure.

During the CO exposure the half width at half maximum (hwhm) and the structure of the very broad band between 2600 and 2000 cm^{-1} assigned to hydrated proton species show an extreme increase during the first 10 minutes. Afterwards, the band structure and the intensity do not change significantly. In parallel to this increase of the H_3O^+ concentration, the

bands present at 1367 , 1050 cm^{-1} decrease in the same time scale. After 10 minutes of CO exposure the band at 1367 cm^{-1} was nearly eliminated, while the band with the maximum at 1067 cm^{-1} was still present with a clear decrease of its intensity.

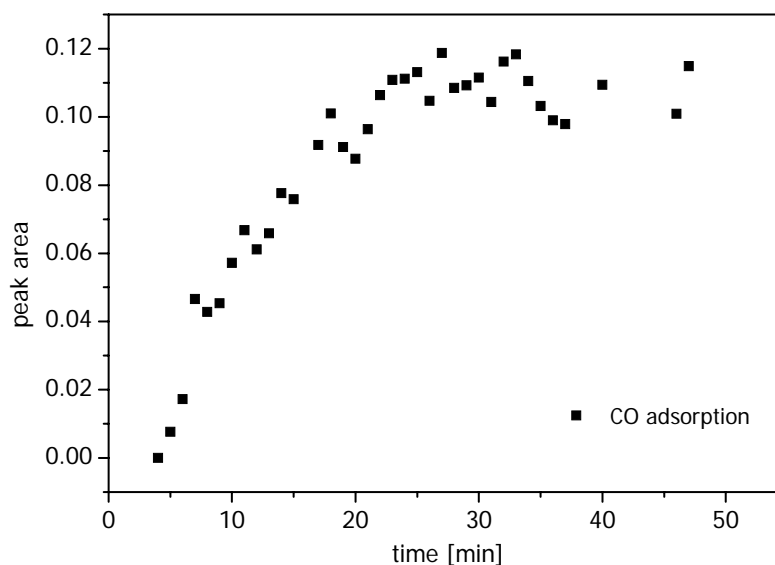


Figure 4.14: The changes of the area of the band corresponding to the weakly bound CO as a function of time. The form of the curve is similar to a Langmuir isotherm.

Also, during further CO exposure new bands appeared at 1584 , 1512 , 1268 and 1224 cm^{-1} . The analysis of the time resolved spectra shows that the intensity of the bands at 1584 and 1224 cm^{-1} as well as the bands at 1512 and 1268 cm^{-1} increase with the same rate (Figure 4.15). The bands at 1584 and 1224 cm^{-1} are assigned to symmetric (O-C-O) and anti-symmetric (O-C-O) stretch vibrations of chelating bidentate carbonates [105, 106, 107]. The bands at 1512 and 1268 cm^{-1} were assigned to the symmetric and anti-symmetric (O-C-O) vibration of surface carboxylate group [105]. The quantitative analysis shows that the creation of these bands runs parallel to the decrease of the surface hydroxyl group at 3638 cm^{-1} , which is an important aid for formulating the reaction equation. In the spectrum recorded after two hours, a weak band at 1726 cm^{-1} was detected which is assigned to the symmetric C-O stretch vibration of

bridging bidentate carbonates. The anti-symmetric C-O stretch mode is between 1200 and 1150 cm^{-1} . This band was not observed in the time resolved spectra, recorded continuously during the first 50 minutes of CO exposure.

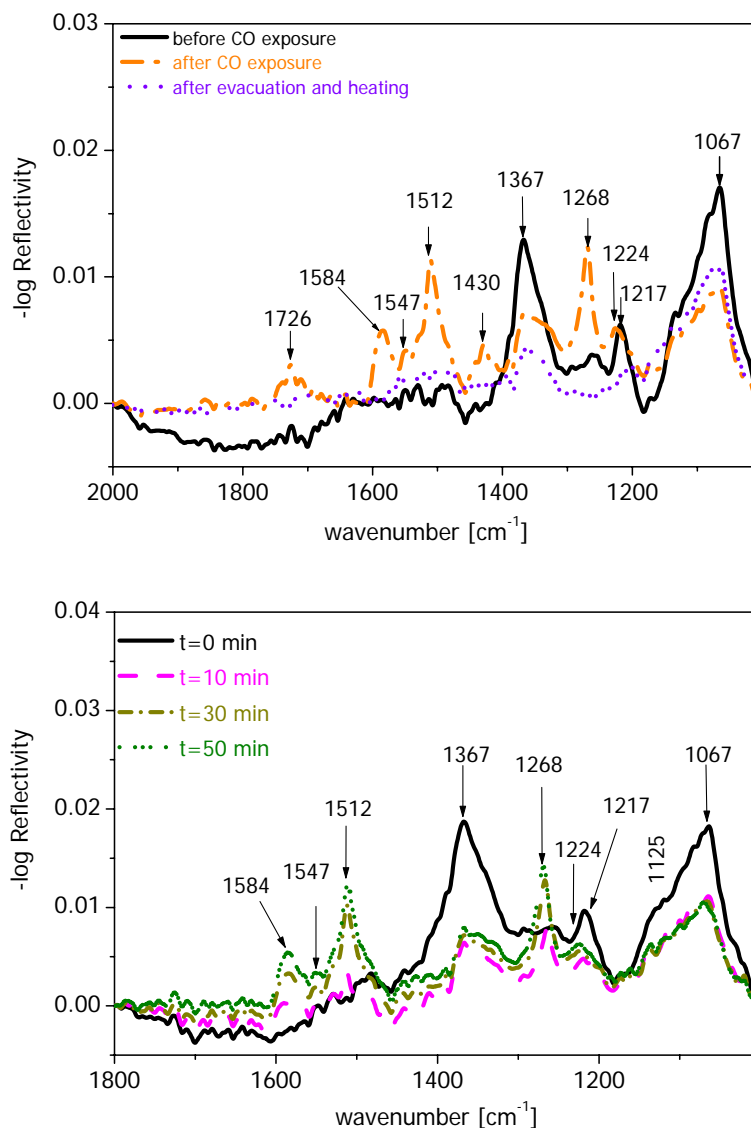
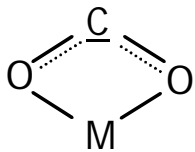
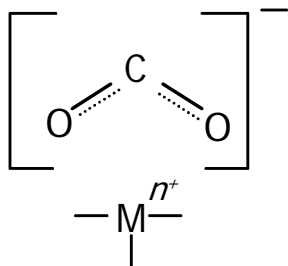


Figure 4.15: Top: Spectral range between 2000 and 1000 cm^{-1} before and after one hour of CO exposure. Bottom: Time resolved spectra recorded during CO exposure.

Two types of carboxylates are described in the literature. For example, in the Willet's description both oxygen atoms of carboxylates molecules are bound to the metal cation, while in Davydov's description there is no bond between oxygen atoms of the carboxylate molecules and the metal atom

(as formates). Table 6 shows two structures of carboxylates drawn by different authors. The observed frequencies of the symmetrical and asymmetrical vibration modes are at higher frequencies for the ionized form (difference between ν_{as} and ν_s in both cases is more or less the same). Whereas on the powder measurements performed under static conditions bound carboxylates (I) are present, on the sensor performed under dynamic conditions at higher temperatures, ionized form of carboxylates (II) are present. For a better understanding of the surface reaction mechanism, the form of the carboxylates on the surface must be clearly defined (ionized or bonded).

Table 6: Literature overview of surface carboxylate in terms of structure and absorption frequencies.

Structure	Observed frequencies [cm^{-1}]	Reference
I 	1520-1560 (ν_{as}) 1300 (ν_s)	[81]
II 	1630-1560 (ν_{as}) 1420-1350 (ν_s)	[22]

Additionally, in this spectral range unidentate carbonates ($\nu_{as(\text{COO}^-)}=1547$, $\nu_{s(\text{COO}^-)}=1370$ and $\nu_{(\text{C-O})}=1080 \text{ cm}^{-1}$) were detected on the commercial powder in the presence of pure CO.

A quantitative analysis for each absorption band is performed, in order to find a correlation between the chemical compounds which helps us in the construction of a possible reaction mechanism. The results of band analysis (Figure 4.14, Figure 4.16) show, firstly, that the intensity of the OH groups

at 3638 cm^{-1} , carbonate ions, hydrated proton and physisorbed CO start to change at the same time, namely 4 minutes after the beginning of CO exposure, while the covalent bound carboxylate creation starts after 8 minutes.

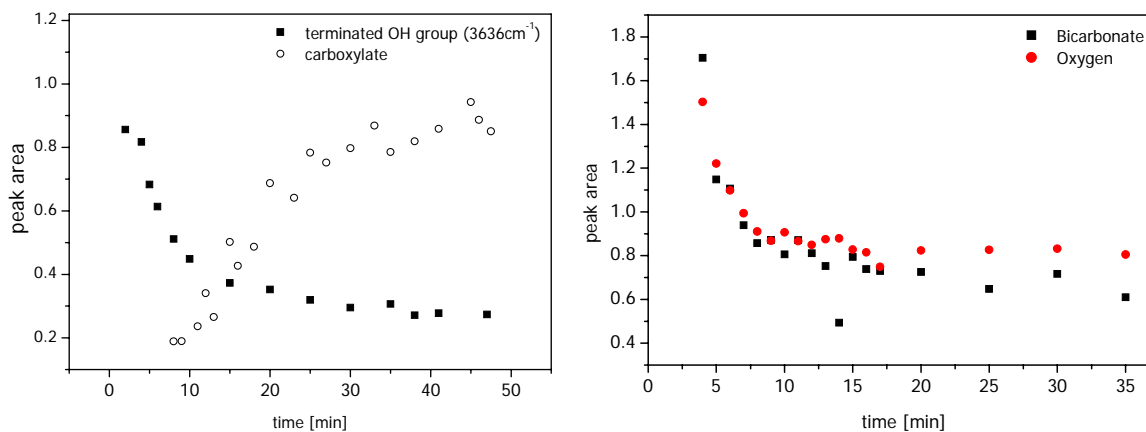


Figure 4.16: Results of band analysis for different surface species.

The second conclusion derived from the band analysis is that the carboxylates are created after nearly all of the above mentioned OH groups have reacted.

On the basis of Figure 4.16 the surface process can be described as a

consecutive reaction, $A \xrightarrow{k_1} B \xrightarrow{k_1^*} C$, with an exponential decrease of reactant A. The increase of B as the intermediate product takes place with the same gradient as the decrease of A at the beginning of the reaction. The rate of reduction of the reactants and the rate of increase of the intermediate products depend on the ratio of the reaction constants. If $\frac{k_1}{k_1^*}$ is big, the

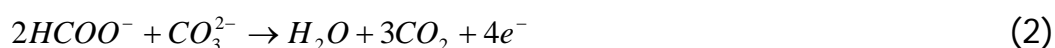
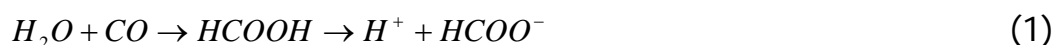
reduction of A is fast and the concentration of the intermediate product is high. If $\frac{k_1}{k_1^*}$ is small, the decrease of A is slow and the concentration of B is

low, like in our case. However, we could not identify the intermediate product, most probably due to its very low concentration or due to measurement conditions (e.g. temperature). Possible intermediate products occur probably only at high temperatures under dynamic conditions (see

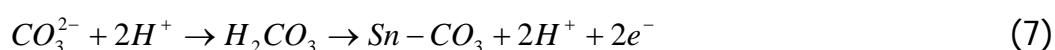
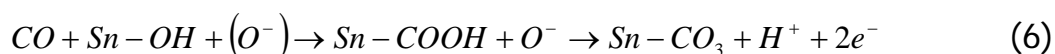
chapter 4.1.4.2). After reheating the powder at high temperatures ($\sim 470^\circ\text{C}$) under vacuum over night the broad band between 2600 and 2000 cm^{-1} and the band at about 1050 cm^{-1} increased and all bands corresponding to carbonate like species and water related species vanished completely.

The above description of experimental facts suggests that several reactions are taking place upon CO exposure. According to the analysis of the time resolved spectra and the band analysis the following reactions seem to take place:

CO can react directly with surface water to form formic acid, which can dissociate to H^+ and HCOO^- (1). H^+ can protonate water molecules (3 and 4) and HCOO^- can react to CO_2 and water (2). The creation of the CO_2 however could not be detected.



Smiltaneously CO reacts with oxygen ions (O^-), which leads to the creation of the covalent bound surface carboxylates, and with a particular terminal OH group, which leads to the covalent bound surface chelated bidentate carbonate involving the oxygen ions. In this reaction protons are created. The new protons can also move to the already existing carbonate ions, so that the increase in the proton concentration moves the equilibrium to the left side of the equation (6) (carbonic acid side). However, the latter one is not stable and decomposes into the surface covalent bound bidentate carbonate and a proton. The reactions can be formulated as:



The result is the creation of covalently bound carbonate-like species: carboxylate vibrating at about 1268 and 1512 cm^{-1} , chelating bidentate carbonate (at 1223 and 1585 cm^{-1}) and bridging bidentate carbonate (1726, \sim 1200 cm^{-1}). All of them appear with a significant delay when compared to the physisorption of CO and reaction of OH groups, carbonate ions and, most probably, oxygen ions.

4.1.4.2 CO Measurements on the Un-doped Sensor

Different CO concentrations (30, 60, 125, 250, 350, 500 ppm) were exposed to the sensor at various temperatures (150, 300 and 350°C) and at different relative humidity levels (0, 4, 10, 20 and 50%) in order to examine the temperature and humidity effects on the gas sensing mechanism. In all measurements, the spectrum taken directly prior to CO exposure was used as a reference (detailed description in 3.9), in order to eliminate effects coming from the substrate. In the temperature cycle experiments described above it was demonstrated that the surface structure changes dramatically at about 200°C. In order to understand the influence of the changes of the molecular structure on the conductivity, measurements were performed at three temperatures (150, 300 and 350°C). One temperature was lower than the operation temperatures and two temperatures were in the operating temperature range.

4.1.4.2.1 Influence of operation temperature on CO detection

In the first set of experiments, the influence of temperature as a function of CO concentration on the DRIFT-spectra and on the sensor signal was investigated.

Figure 4.17 shows spectra recorded at 150°C in dry air in the presence of different CO concentrations over the spectral range between 4000 and 850 cm^{-1} . Spectra are presented in KM-units which give a linear relationship between the band intensity and the concentration of the adsorbed surface

species. Spectra recorded in synthetic dry air direct prior to CO exposure were used as reference.

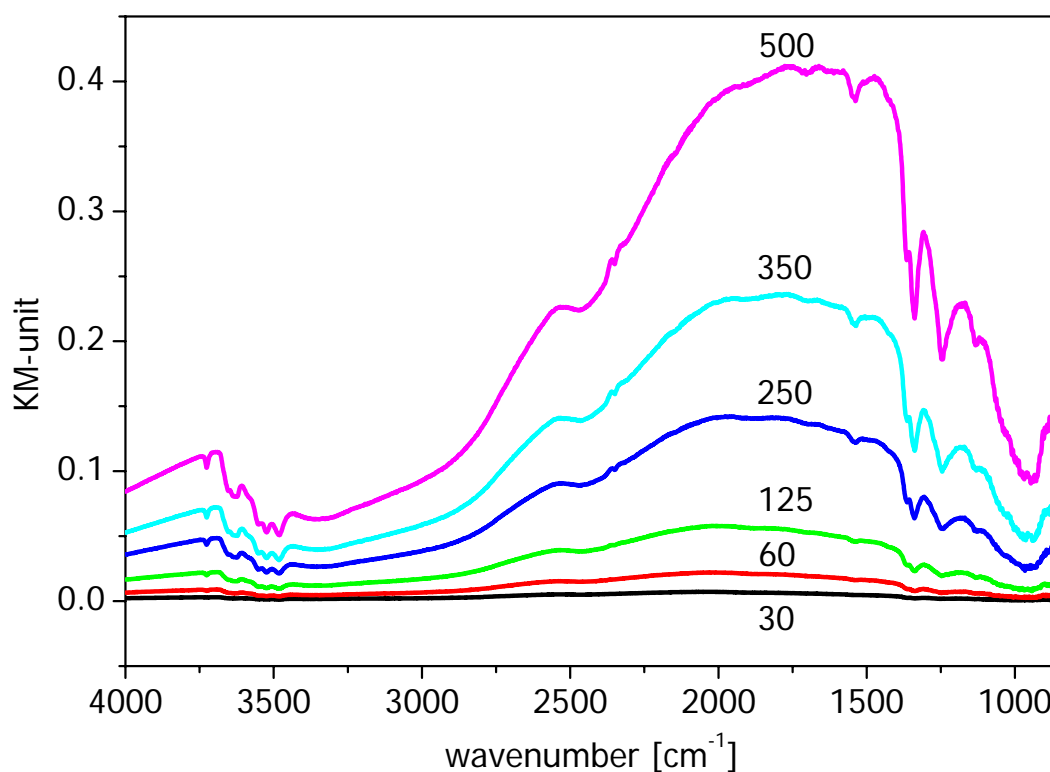


Figure 4.17 Difference spectra in the presence of CO in different concentrations (30, 60, 125, 250, 350, 500 ppm) at 150°C in dry air. Spectra before each CO exposure in dry air were used as reference.

Exposure to CO of the tin oxide surface leads to different changes in the spectra: 1) On the molecular level, the band intensities of the already existing absorption bands change and new absorption bands are created. 2) Additionally, a broad absorption covering the total middle infrared (MIR) range appears in the spectrum, the intensity of which increases linearly with CO concentration.

For better illustration of the changes in the spectra, individual spectral ranges are shown (4000-3000 cm^{-1} , 3000-2000 cm^{-1} , 2000-850 cm^{-1}) in Figure 4.18-Figure 4.20.

The following information was extracted from the infrared spectra during CO adsorption at 150°C:

1. In the OH/H₂O range, all bands corresponding to the different hydroxyl groups and water decrease in the presence of CO. No specific CO interaction was found. On the powder, an interaction between only one type of hydroxyl group (located at 3638 cm⁻¹) and CO was observed (see chapter 4.1.4.1).

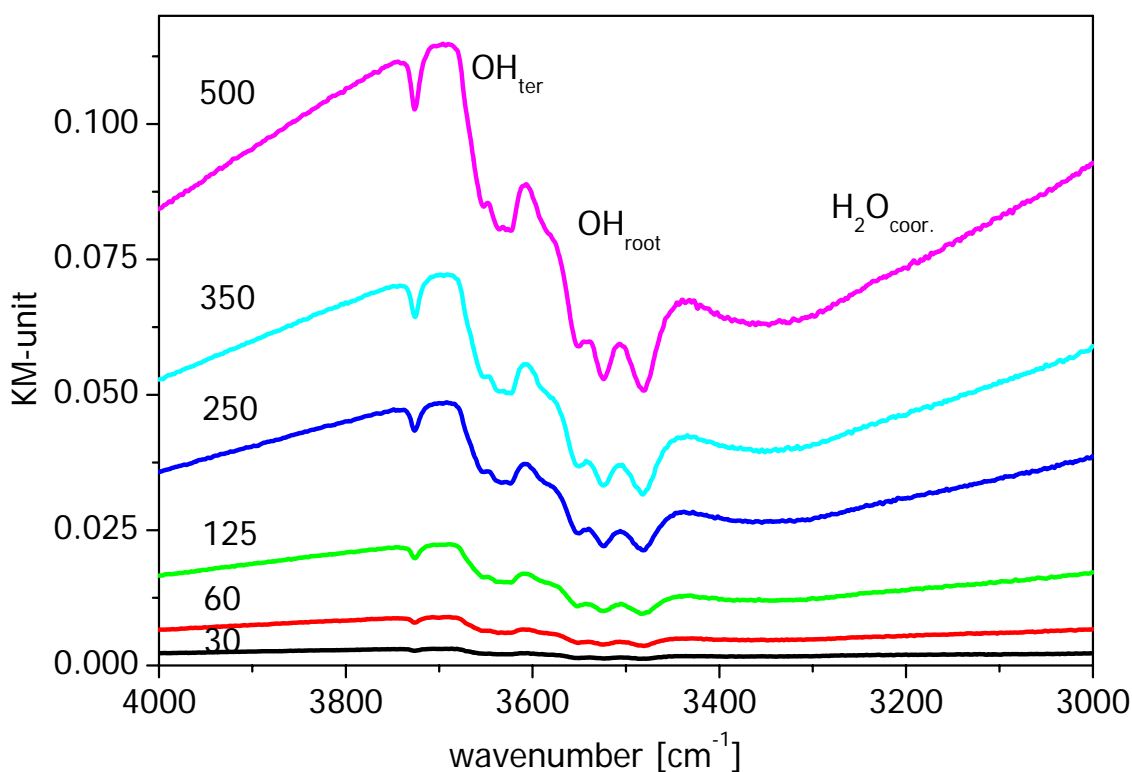


Figure 4.18: OH/H₂O spectral range of spectra recorded at 150°C in dry air, in the presence of various CO concentrations (30-500 ppm).

2. In the middle spectral range, between 3000 and 2000 cm⁻¹, the broad absorption (at 2550 cm⁻¹) assigned to hydrated proton species which was observed during the powder measurements was also detected. Two bands with a rotation–vibration fine structure with the characteristic absorption at 2350 and 2143 cm⁻¹ were also detected which corresponds to gaseous CO₂ and CO, respectively. While hydrated protons (H₃O⁺) and carbon dioxide (CO₂) are the main products of the reaction, CO is remaining as reactant. Both gases are

in the pores of the sensitive layer (characterized by the narrow P-R distance).

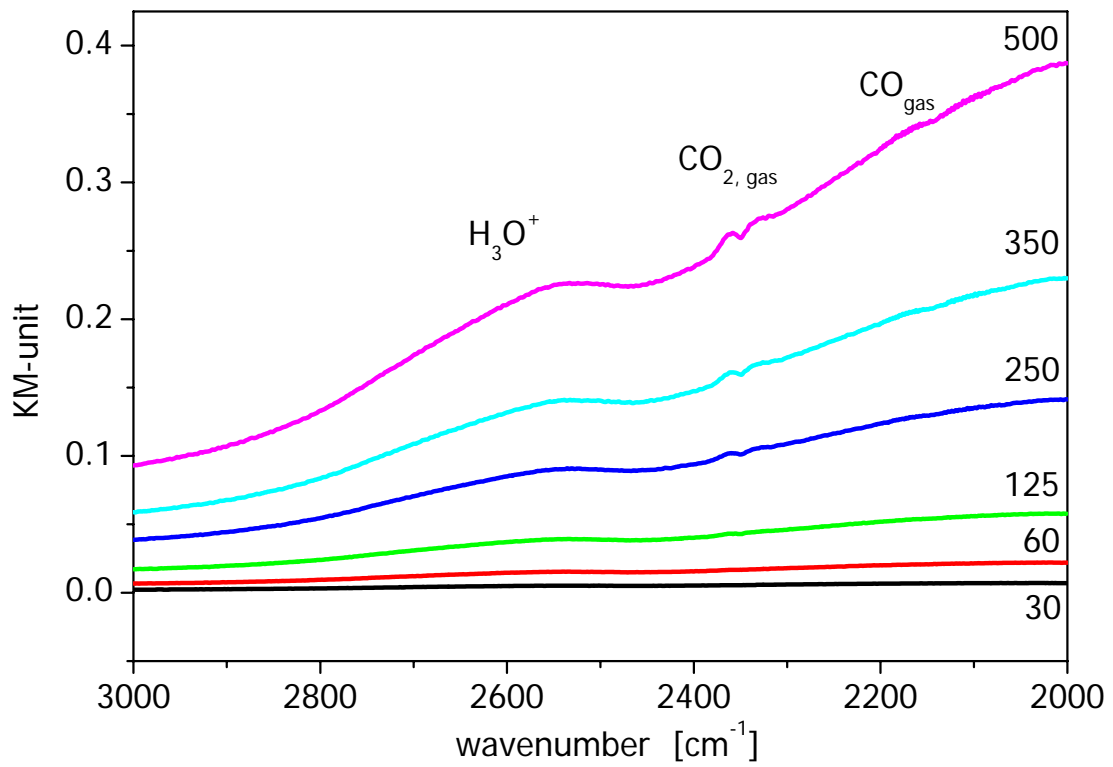


Figure 4.19: Spectral range between 3000 and 2000 cm^{-1} in the presence of different CO concentration (30-500 ppm) at 150°C, where hydrated proton species, CO and CO_2 appear in the spectra.

3. In the spectral range between 2000 and 850 cm^{-1} the bands assigned to the deformation mode of hydroxyl groups, the deformation mode of water, and different surface oxygen species decrease. In addition, the creation of two relatively broad absorption bands with the maxima at 1750 and 1660 cm^{-1} was detected. In this work the band at 1750 cm^{-1} is assigned to the symmetrical vibration mode of bridged bidentate carbonate ($\nu_{\text{C=O}}$ in carbonate ion). The asymmetrical vibration mode of bridge bidentate carbonates ($\nu_{\text{as, COO}^-}$) is expected to be at 1200 cm^{-1} and the symmetrical one at about 1050 cm^{-1} . These two vibrations were not observed in this work. The reason for this might be an overlapping of these bands with the bands ascribed to deformation

modes of the surface hydroxyl groups and surface oxygen species, which are decreasing in the presence of CO. The observed frequency of the symmetrical vibration mode ($\nu_{C=O}$) of bidentate carbonate is high. In the literature, this phenomenon is explained by the covalency of the M-O bond in the carbonate complexes, which influences the frequency of the bands belonging to the symmetrical and asymmetrical vibration mode of the carbonates. It was found that the fully covalent bond, as dimethyl carbonate $(CH_3O)_2CO_{II}$, shifts the frequency of the symmetrical and asymmetrical vibration and causes an increase of the splitting ($\nu_{CO_{II}} = 1870\text{ cm}^{-1}$, $\nu_{CO_I} = 1260\text{ cm}^{-1}$, $\Delta\nu = 600\text{ cm}^{-1}$) [108]. The band with the maximum at 1660 cm^{-1} is assigned to the asymmetrical vibration mode of surface carboxylates (CO_2^-) [21, 81].

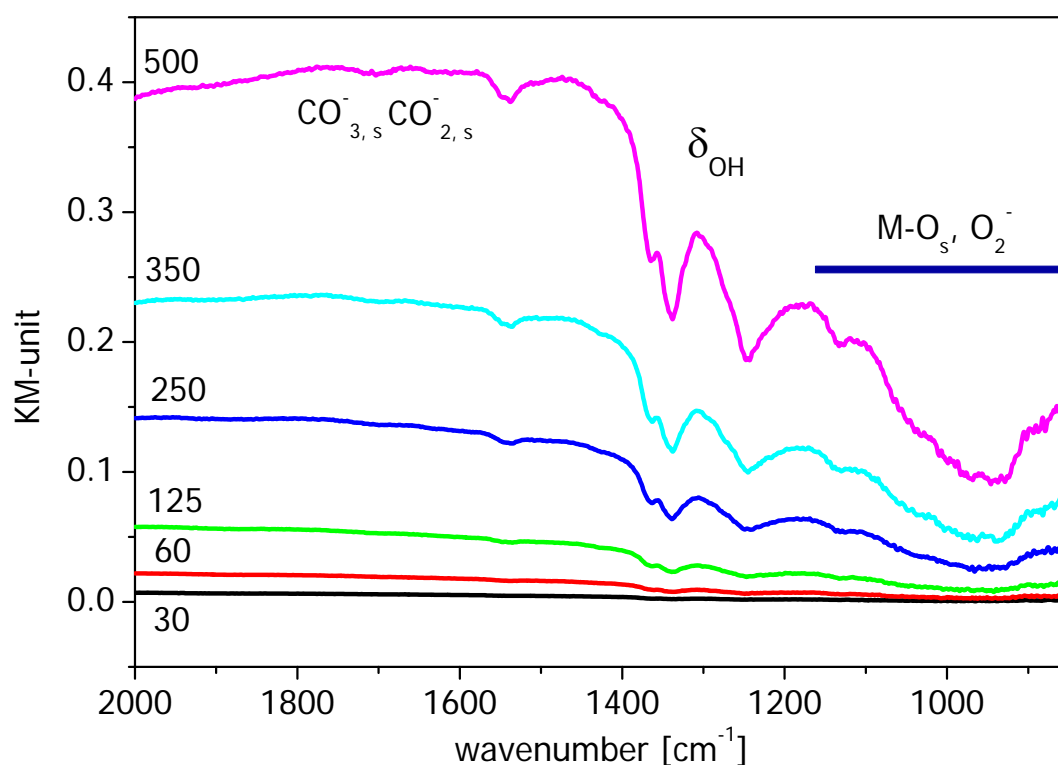


Figure 4.20: Spectral region between 2000 and 850 cm^{-1} , where carbonate related species and oxygen ions appear.

Figure 4.21 shows spectra recorded at 300°C in dry air in the presence of different CO concentrations (60-500 ppm).

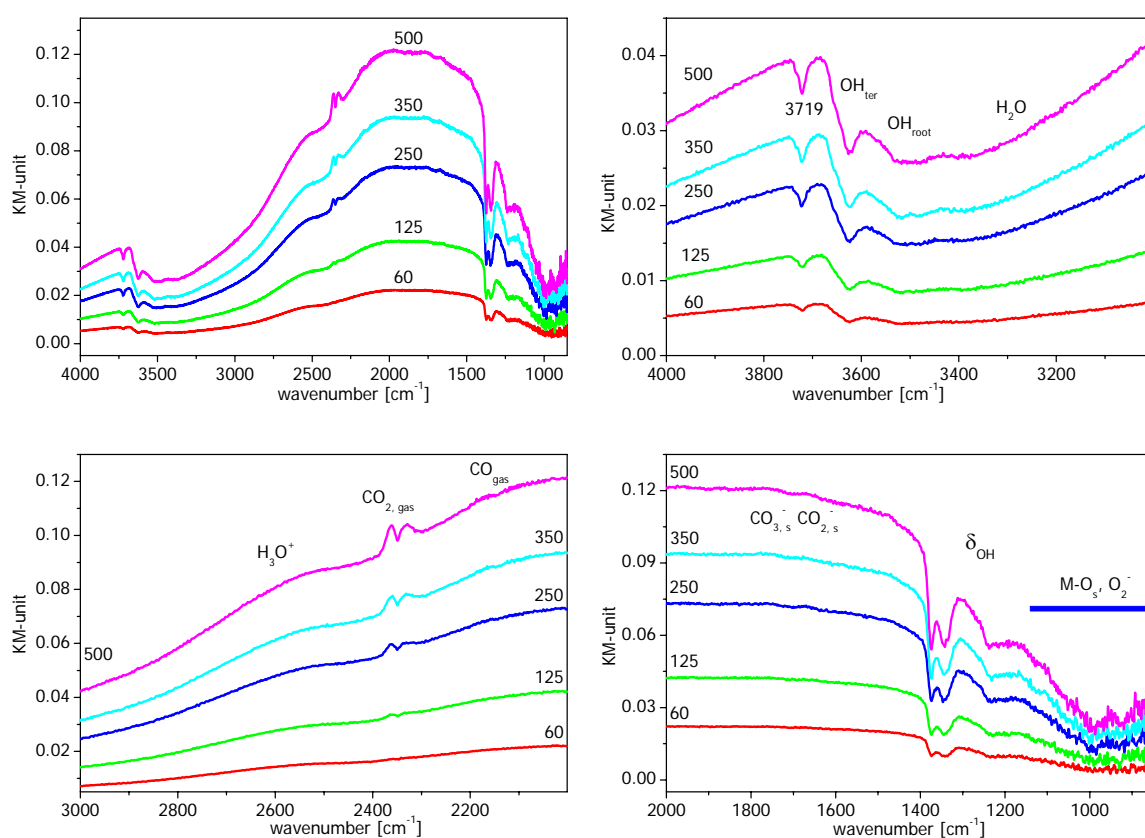


Figure 4.21: DRIFT spectra of un-doped sensors at 300°C in dry air. Top left: Spectral range between 4000 and 850 cm^{-1} . Top right: the OH/H₂O region. Bottom left: Characteristic spectral region for CO, CO₂ and, in this study H₃O⁺, H₅O₂⁺ vibration. Bottom right: The spectral region between 2000 and 850 cm^{-1} shows the characteristic deformation mode of the water, hydroxyl groups, vibrations corresponding to carbonate like species and oxygen.

Basically, changes in the spectra recorded at 300°C in dry air in the presence of CO are similar to the ones for the case of 150°C. In the presence of CO what was detected was a decrease of the band intensity ascribed to surface hydroxyl groups, water, oxygen species and an increase of bands assigned to hydrated proton species, CO, CO₂ in the gas phase, carboxylates (CO₂⁻) and bridged carbonate. However, the intensities of the absorption bands and the shapes of the spectra recorded at 300°C in dry air are different from those at 150°C. In the middle spectral range between 3000 and 2000 cm^{-1} additional to the broad band corresponding to the

hydrated protons (maximum at about 2550 cm^{-1}) a new band corresponding to H_5O_2^+ (2100 cm^{-1}), called *Zundel structure* overlapping with the CO rotation vibration band, was detected. At 300°C , the intensity of the broad absorption is lower than that at 150°C . The maximum of this broad band is shifted to the higher wavenumbers and its shape differs from the spectrum recorded at 150°C . If the interpretation that the broad absorption is caused by the electronic transition from shallow levels into the conduction band is true, the shift of the maximum of the broad band absorption can indicate that the transition occurs probably from different shallow levels during the reaction depending on the measurement condition (temperature, humidity). The reason for the creation of different shallow levels might be the reaction of CO with surface oxygen, which was assumed by ISS measurements [30]. It must be stressed again that for a better understanding of the origin of this broad absorption band, we need additional calculations and further in situ experiments.

At 350°C in dry air, the observed changes in the spectra are not very different from the ones at 150 and 300°C . However, the intensities of the absorption bands are much less pronounced than in the case of lower temperatures (see quantitative analysis). Especially CO and CO_2 bands, supposed to be in the cavity of the sensitive layer, are hardly detectable. The bad signal-to-noise ratio of the spectra recorded in the presence of 350 and 500 ppm CO hinders the recognition of the rotation vibration fine structure of CO, if CO exists. Although the signal-to-noise ratio is much higher in the spectra recorded in CO concentrations lower than 350 ppm , no CO vibration mode was detected.

Figure 4.22 shows spectra taken in the presence of different CO concentrations (30 - 500 ppm) at 350°C in dry air in various spectral ranges.

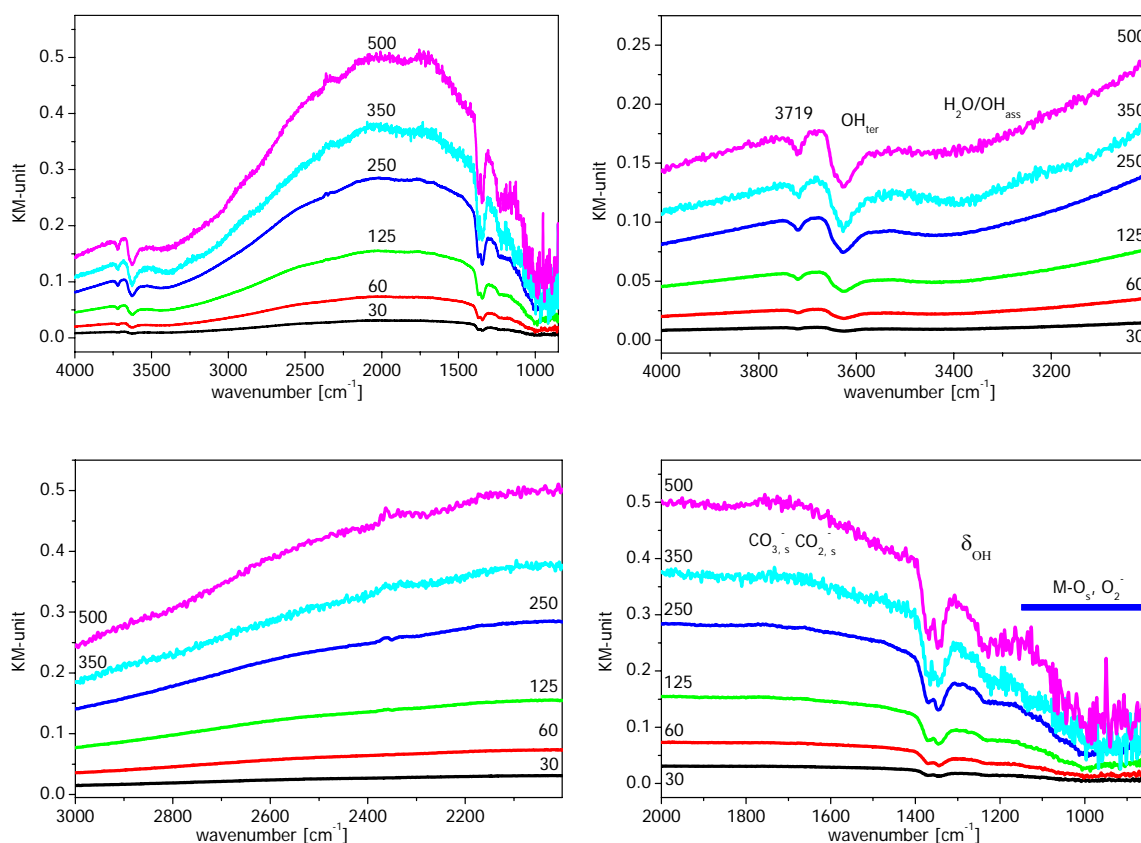


Figure 4.22: DRIFT spectra of un-doped sensors at 350°C in dry air. Top left: Spectral range between 4000 and 850 cm^{-1} . Top right: the OH/H₂O region. Bottom left: Characteristic spectral region for CO, CO₂ and in our measurements H₃O⁺ vibration. Bottom right: Spectral region between 2000 and 850 cm^{-1} where the characteristic deformation mode of the water, hydroxyl groups, vibrations corresponding to carbonate like species and oxygen appear.

Figure 4.23 presents resistance changes (left) and the sensor signal (right) at 150, 300 and 350°C in dry air as a function of CO concentration and of time. The sensor resistance in dry air does not differ between 150°C and 300°C (slightly increased), but it decreases dramatically at 350°C. At all temperatures, the sensor resistance decreases in the presence of CO in different magnitudes as the result of the reaction between CO and surface oxygen when CO₂ is created and an electron is released into the bulk. In the raw data of the resistance measurements one can clearly see that at 150°C the response time and especially recovery time of the sensor is longer than at 300 and 350°C.

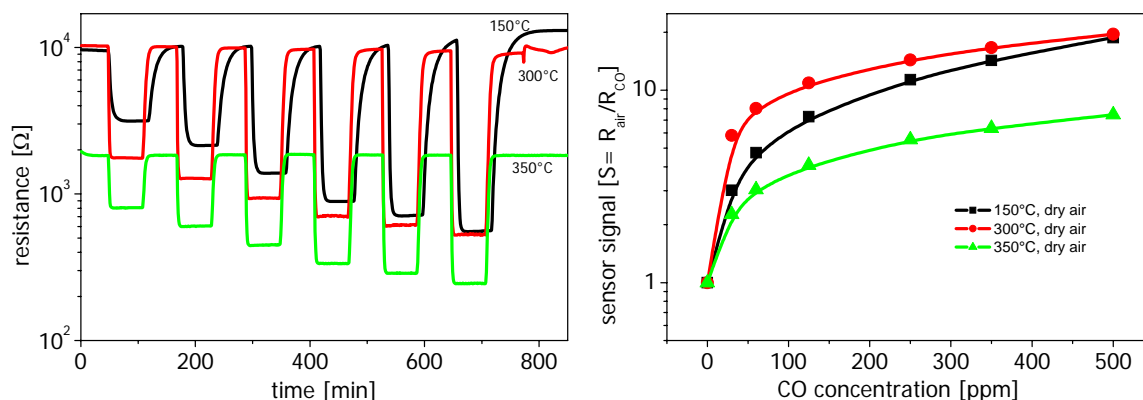


Figure 4.23: Resistance (left) and sensor signal (right) of un-doped sensor at various temperatures as function of CO concentration in dry air.

Looking at the sensor signal (Figure 4.23 right) obtained at different temperatures the lowest sensor signal is at 350°C. At first sight, this is surprising, since the concentration of the oxygen ions (O^-) should dominate at higher temperatures (see Chapter 2.11.1), which is very reactive to CO and makes the main contribution to the sensing process measured as sensor signal. However, the adsorption of CO decreases with increasing temperature and therefore there are not enough CO molecules to react with the surface oxygen ions (O^-). On the basis of DRIFT measurements, we expected that the major sensor signal difference would appear around 200°C, since a dramatical structure changes in the hydroxyl groups spectral range was observed. Spectra recorded at 300 and 350°C were not too different from the point of the hydroxyl groups (see chapter 4.1.3.1). As we will see in the following chapter, additional to the presence of surface oxygen species and hydroxyl groups small amount of water on the surface is needed for high sensitivity in order to create surface species which provide donors.

4.1.4.2.2 CO Effect in the Presence of Humidity

In order to examine the influence of humidity, a set of experiments at different relative humidity levels (0, 4, 10, 20 and 50% r.h.) and at several temperatures (150, 300, 350°C) were conducted.

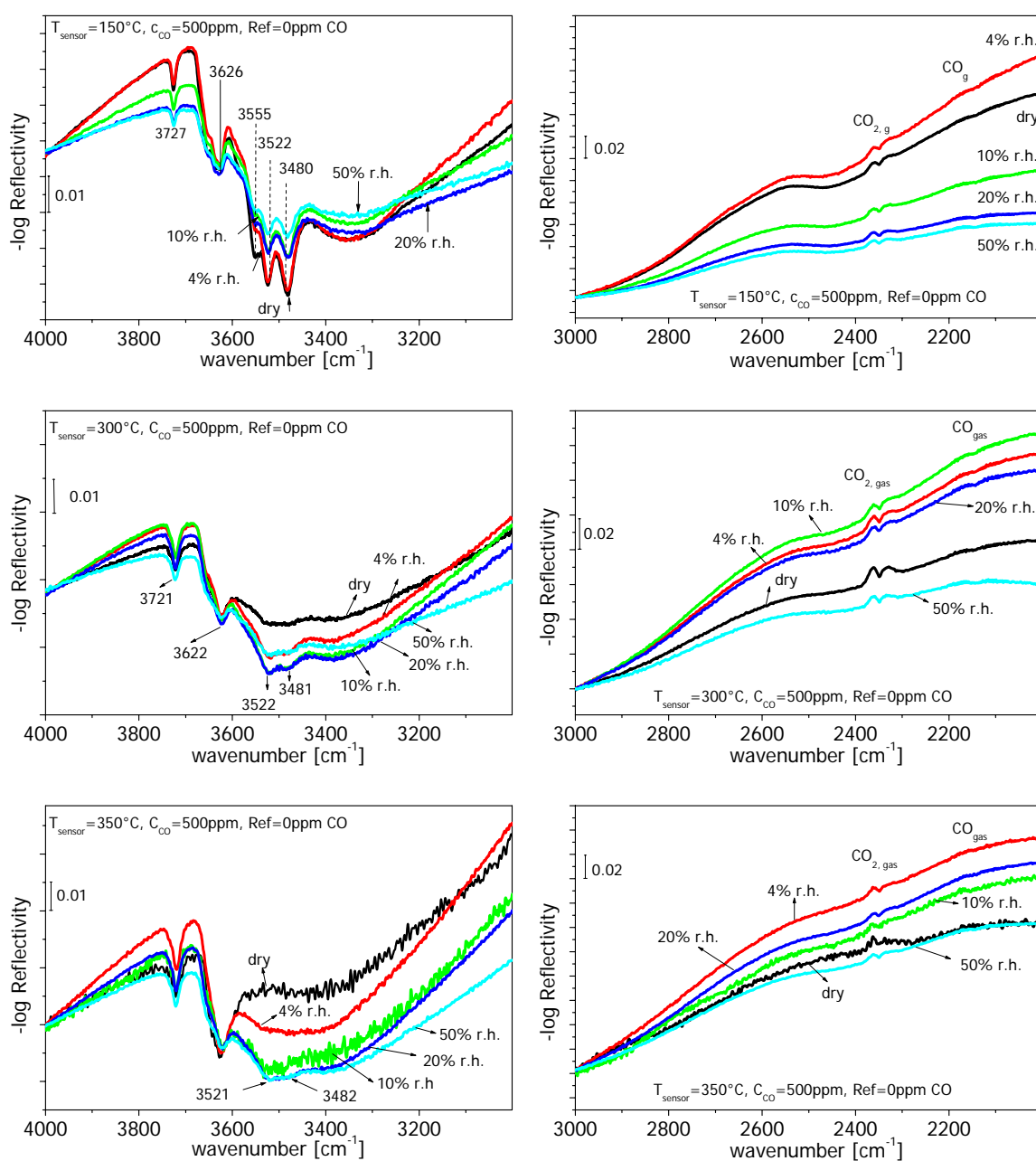


Figure 4.24: Effect of humidity on the spectra at 150°C (top), 300°C (middle) and 350°C (bottom). Two spectral regions are shown. Left: The OH/H₂O spectral region. Right: The H₃O⁺, CO₂, CO region at respective temperatures.

Figure 4.24 reveals the influence of the humidity on the spectra in the presence of 500 ppm CO at different temperatures. Two spectral ranges from 4000 to 3000 cm⁻¹ (left) and 3000 to 2000 cm⁻¹ (right) are shown at various temperatures. Each spectral region is normalised to a certain value, in order to see changes of the spectral features caused by the humidity.

Humidity gives rise to the following effects:

The intensities of all bands ascribed to hydroxyl groups, water and different oxygen species decrease in the presence of CO at all temperatures and humidity levels employed in this work. Gaseous CO₂, like adsorbed surface species bridged bidentate carbonate and carboxylates are the product of the reaction.

At 150°C, in the complete spectral range between 4000 and 850 cm⁻¹ (Only two spectral ranges are shown in Figure 4.24. top left: spectral range 4000-3000 cm⁻¹ and top right: the spectral range 3000-2000 cm⁻¹) one can see that the higher the humidity, the smaller the decrease of band intensity. At high temperatures (300 and 350°C), the trend is inverted: the higher the humidity, the larger the decrease of band intensities. At these high temperatures, in the spectral range 4000-3000 cm⁻¹, negative bands at 3522 and 3481 cm⁻¹ were seen in the presence of humidity and CO. These bands, assigned to rooted OH groups, were initially detected at lower temperatures (below 200°C); they shifted and vanished with increasing temperatures in dry air (see 4.1.3). The appearance of these bands in the spectra as negative bands in the presence of humidity indicate, that they were rebuilt at higher temperatures in the presence of humidity and interact with CO molecules. It is a confirmation of the assumption that water dissociation at the surface at higher temperatures results in different types of hydroxyl groups (terminal Sn-OH and rooted hydroxyl group O_{lat}-H).

The intensity of the bands corresponding to gaseous CO and CO₂ was also influenced by the humidity. With increasing humidity the intensity of the gaseous CO and CO₂ located in the pores of material decreases.

The influence of the humidity on the changes of the band intensity was obtained by the quantitative analysis of the individual absorption bands, which is presented below.

Before presenting the results of the quantitative analysis, difference spectra created by the comparison of those recorded before and after the

exposure of CO at various temperatures, in dry and humid air are shown in Figure 4.25 and Figure 4.26.

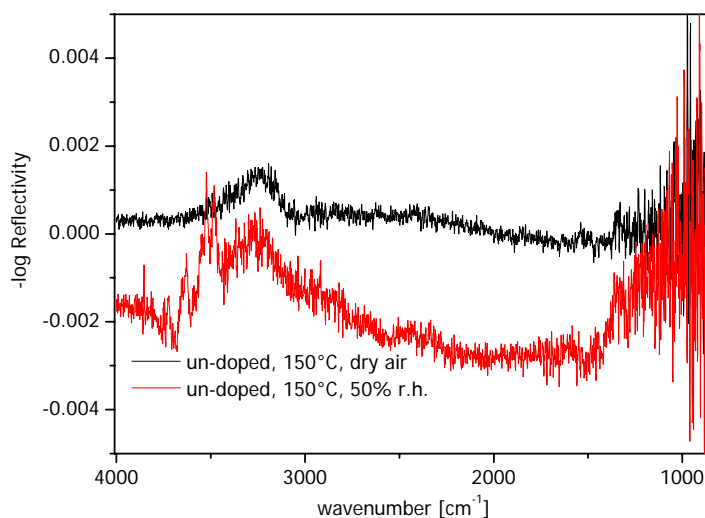


Figure 4.25: Spectra recorded after the exposure to CO in dry and humid air at 150°C. Spectrum recorded before the CO pulse was used as reference.

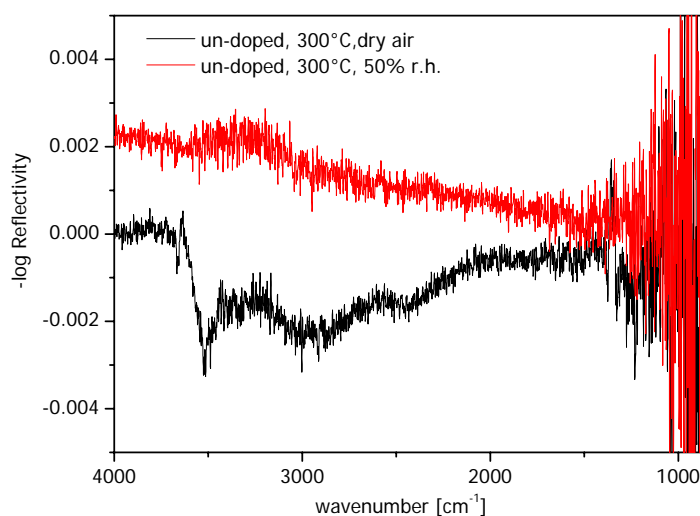


Figure 4.26: Spectra recorded after the exposure to CO in dry and humid air at 300°C. Spectrum recorded before the CO pulse was used as reference.

The comparison shows that in each case spectra recorded at 150°C and at 300°C in dry air and in the presence of humidity come back to the initial state (before CO exposure). The baseline is in the range of 10^{-3} and it is in the range of detector signal-to-noise ratio.

In order to get an overview and to obtain a correlation between the intensity changes of the reactants and products as functions of temperature and humidity levels, a quantitative analysis at each temperature was performed. As described in the chapter "*Basics and Survey*" for the quantitative band analysis for the adsorbed species KM-units were used, because they show the linear relationship between band intensity (in this work calculated as area of an absorption band) and concentration of the corresponding adsorbates. For the gaseous species (CO-CO₂) *-log Reflectivity* was used.

In Figure 4.27 and Figure 4.28 results obtained by using the quantitative band analysis plotted versus humidity levels and the resistance measurements are presented. As mentioned in Chapter 3.10, for the fitting of the absorption bands either Lorenz or Voigt functions were used depending on the band structure in order to calculate the integrated area. Cutting of the wings of the Lorenz curve causes an error of 10-18% which is given in the graphs as error bars.

For the quantitative analysis, hydroxyl groups and different oxygen species were considered as reactants (band at 1133 cm⁻¹ assigned to O₂⁻ ions stabilized on Sn³⁺ and band at 1045 cm⁻¹ assigned to O₂⁻ ions stabilized at Sn²⁺). Hydrated proton (H₃O⁺), surface carboxylate-ions (CO₂⁻), and surface carbonates were considered as reaction products.

As mentioned above, for the CO measurements the difference spectra were calculated; they show the relative changes determined by the CO exposure. It must be pointed out that in the diagrams one must take into account the absolute values, the negative values are presenting the intensity of the bands which are consumed during the reaction (reactants). For example, in Figure 4.27 in the left diagram the relative changes of the absorption band intensity at 1045 cm⁻¹ are shown at different relative humidity levels. The larger the absolute value, the larger the difference and the higher the changes in concentration of the species which are consumed

or created by the reaction. Therefore, in the curves presented in Figure 4.27 and Figure 4.28 minima (reactants) and maxima (for the products) show the magnitude of the changes of the band intensity in comparison to the initial spectra recorded in the absence of CO.

Generally, at 150°C one records the biggest changes for products and reactants in dry air and at 4% r.h.

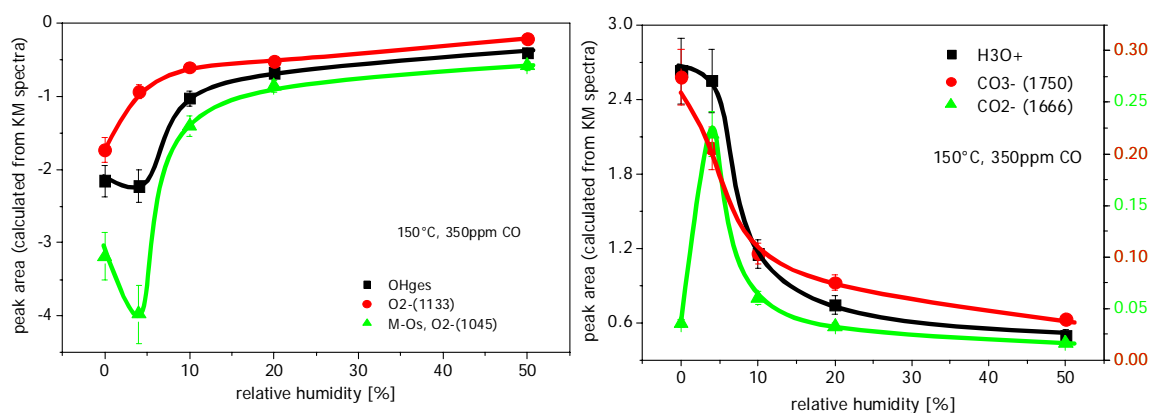


Figure 4.27: Results obtained by quantitative band analysis for the influence of humidity at 150°C.

A comparison of all humidity dependency curves indicates the following correlations between educts and products:

- OH groups: The maximum differences are in dry air and at very low humidity levels. With increasing humidity, the changes are getting smaller. It stands out that the changes of the OH-band intensity as a function of humidity correlates with the changes of the band intensity corresponding to hydrated proton species (H_3O^+).
- Oxygen ions (1133 cm^{-1}): Maximum of the difference is in dry air. With the increase of relative humidity the changes decrease. It stands out that the course of the curve belonging to oxygen behaves in the same way as the curve belonging to carbonate ions (CO_3^-).
- Oxygen ions (1045 cm^{-1}): The course of the curve, which is a result of changes of the band intensity at 1045 cm^{-1} , is quite prominent. A similar prominent course was obtained for the surface carboxylate ions (Figure 4.27, left diagram). This indicates that by the creation of the surface

carboxylates the other surface oxygen species (at 1045 cm^{-1}) are involved. It must be noted that additional measurements are needed in the low humidity range (0-10% r.h.) at this temperature, in order to make these results more reliable. This maximum at 4% r.h. could be also an outlier.

- Generally, one can say that with increasing humidity the concentration differences (always in comparison to the CO free spectrum) decrease for educts and products at 150°C . The interaction between CO and surface species is inhibited by humidity.

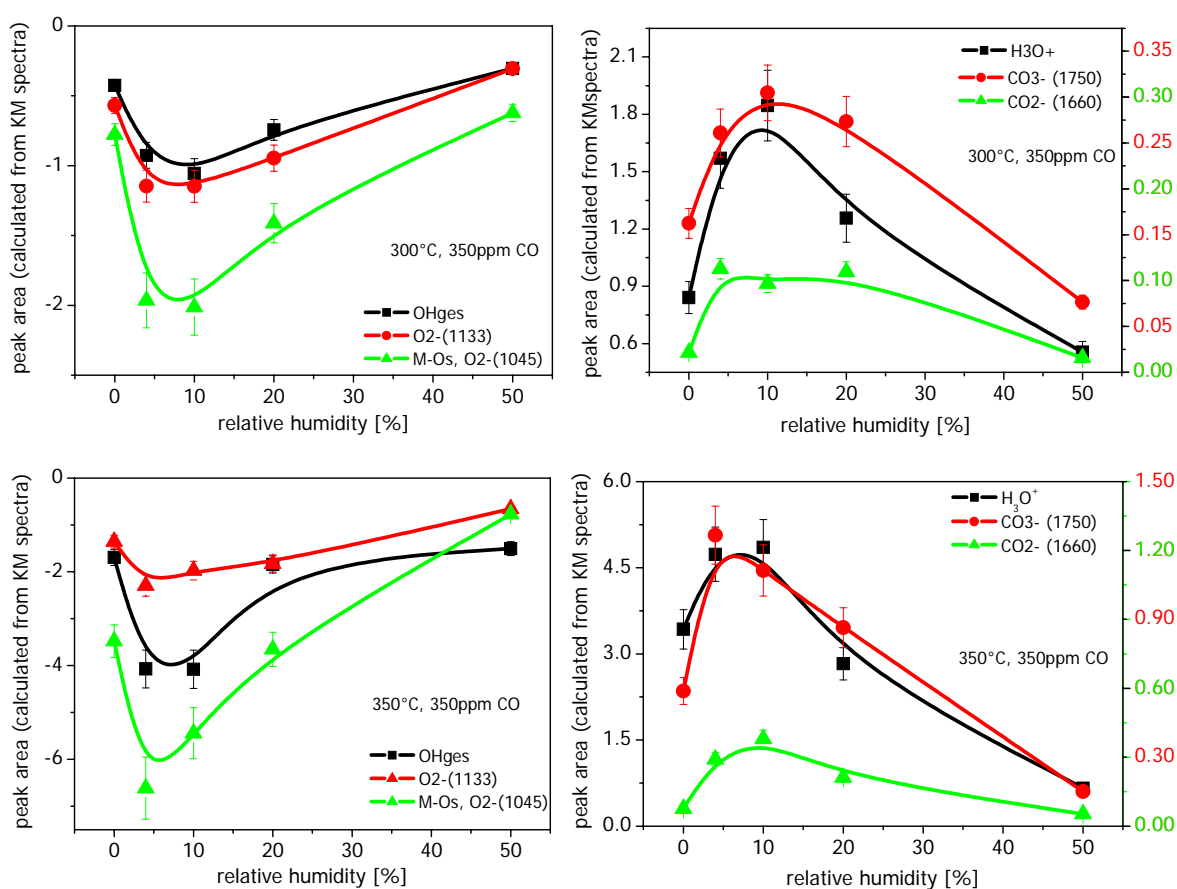


Figure 4.28: Results obtained by quantitative band analysis for the influence of humidity at different temperatures. Top 300°C and bottom 350°C

A shift of the maximum changes towards low humidity levels (4 and 10% r.h.) was recorded at high temperatures. The relationships at 150°C between educts and products described above were observed also at 300°C and 350°C , although the relationships between educts and products are not

so clear as in the case of at 150°C. For the un-doped sensor at the investigated temperatures and humidity levels, the results can be summarised as 1) surface hydroxyl groups are involved in the creation of the hydrated protons; one should note the following changes of the concentration of the hydroxyl groups: In the temperature cycle, two types of terminal hydroxyl groups were detected on the surface. The transition temperature from one type to the other was found to be around 200°C. Due to different extinction coefficients, the concentrations of the hydroxyl groups measured below and above 200°C cannot be compared. Therefore, one cannot say that the decrease of the hydroxyl groups intensities (-2) is bigger than the decrease of the hydroxyl groups intensity at 300°C (-1). Only the differences of the hydroxyl groups' intensities determined for 300 and 350°C can be compared directly, 2) different oxygen species (1045 and 1133 cm^{-1} respectively) participate in the formation of the surface carboxylate and carbonate ions.

The sensor signal for CO as a function of humidity at various temperatures is shown in Figure 4.29 (left). One can see that the sensor signal decreases dramatically in the presence of humidity at 150°C, whereas an opposite behaviour occurs at higher temperatures (300 and 350°C). On the basis of the work function and conductance investigations on Pd-doped sensor measured between 200 and 400°C it was found that the humidity increases the sensor signal dramatically due to the occurrence of a reaction between CO and isolated surface hydroxyl groups in addition to the reaction between CO and surface oxygen ions. There [85], it was concluded that the reaction between CO and hydroxyl groups takes place at lower temperatures and this is the dominating surface reaction, while the reaction between CO and surface oxygen ions (O^-) is dominating reaction at higher temperatures.

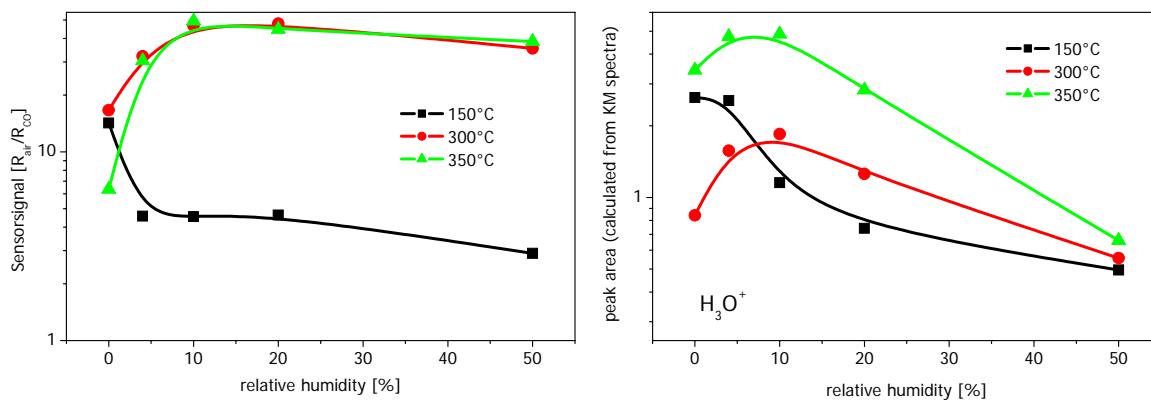


Figure 4.29: Sensor signal and peak area of the hydrated proton species plotted versus different humidity levels at various temperatures.

During the DRIFT and electrical resistance data interpretation, an additional correlation between sensor signals and the peak area of the hydrated proton species (area is proportional to the concentration) was found and is presented in Figure 4.29. This is an important hint for establishing a reaction mechanism or correction of the proposed reaction mechanism which was established by the phenomenological measurements discussed in section 2.11.3.2. According to these results, CO reacts with surface terminal hydroxyl groups to CO_2 and releases a hydrogen atom, which combines with lattice oxygen and provide donors (rooted hydroxyl groups), i. e. free charges. As shown in the DRIFT spectra above, by the reaction in all temperature and humidity levels no rooted hydroxyl groups appears in the spectra during the exposure of CO. The identification of the hydrated proton species offers an alternative sensing mechanism and an improvement of the reaction mechanism proposed in earlier studies.

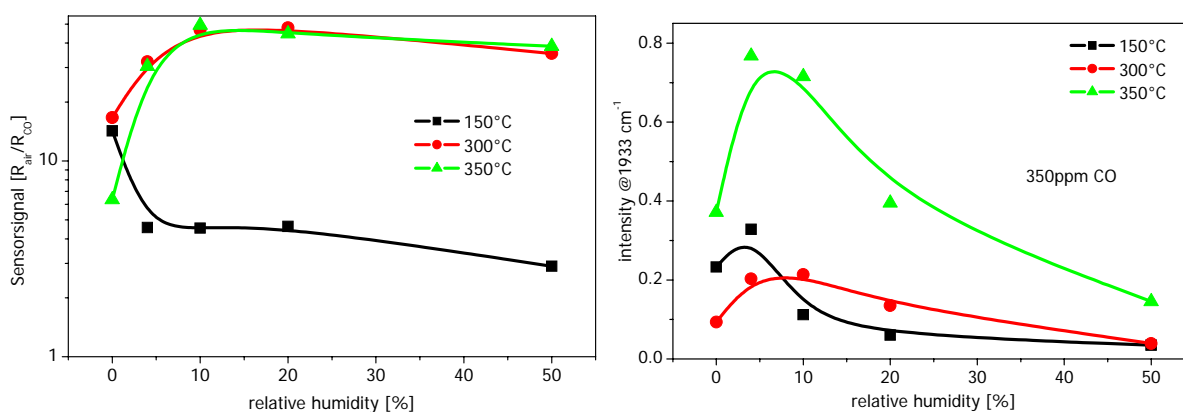


Figure 4.30: Sensor signal and intensity of the broad absorption as function of relative humidity at 150, 300 and 350°C for 350 ppm CO.

Figure 4.30 shows the graphs where the sensor signal and the intensity of the broad absorption band for 350 ppm CO versus humidity are plotted for different temperatures. A very rough correlation between the sensor signal and the broad band intensity can be seen by comparing the dependency of the sensor signal on the humidity level with the dependency of the broad band intensity on the humidity. The broad absorption (almost over the total mid infrared range) was discussed in detail in chapter 2.13. There, the spectroscopic interpretation of this absorption is compared with the results obtained by the phenomenological measurements. It was particularly emphasized that this broad absorption must be investigated further extensively, because the results of the phenomenological methods and IR-spectroscopy are contradictory. Since the interpretation of this band is unclear and the broad absorption is not separated from the contribution of the scattering of the electrons in the conduction band, in this work, only the relationship between the sensor signal and roughly determined intensity of the broad absorption is presented.

The sensor signal at different temperatures recorded in parallel to the DRIFT measurements yields similar results as obtained by DRIFT measurements and is summarised in the following:

- At 150°C an increase of the humidity leads to a decrease of the sensor signal. In contrast to the DRIFT measurements, the sensor signal decreases dramatically already at a very low humidity level (4%r.h.). In DRIFT measurements the highest changes were recorded at low humidity levels. Furthermore the intensity of the hydrated proton species and the broad absorption shows a slower decay with increasing humidity than the sensor signal.
- At 300 and 350°C the results obtained by resistance and DRIFT measurements are in agreement, meaning that the maximum changes in both types of measurements are obtained under the same conditions.

The information obtained by DRIFT spectroscopy and DC measurements leads to the following conclusion for the CO sensing mechanism for undoped material: CO reacts with all surface species (OH_{ter} , OH_{root} , H_2O and oxygen species) directly or indirectly. The main products are CO_2 , hydrated protons (H_3O^+) and their higher homologues (H_5O_2^+), surface carboxylates (CO_2^-) and surface carbonate (CO_3^-) ions.

The second important result is the identification of surface carboxylate and carbonate ions as reaction intermediate products, which disappear from the spectra in the absence of CO. Previous studies of CO adsorption on the powder showed sharp bands assigned to surface carbonates (different bidentate carbonates) in the spectral range between 2000 and 1000 cm^{-1} . Only in vacuum at high temperatures, it was possible to remove the bidentate carbonates from the powder surface. Quantitative analysis of the time resolved spectra recorded on the powder showed that a consecutive reaction was taking place on the powder surface through the CO exposure at RT. However, it was not possible to detect any intermediate product. This indicates that the surface carboxylates and carbonates detected on the sensor surface are intermediate products of the reaction, if the measurements are conducted at high temperatures and in flow.

In the following, possible reaction mechanisms are established on the basis of the correlations described above and the resistance measurements. Cartoon presentations are given for a better description of the reaction mechanisms.

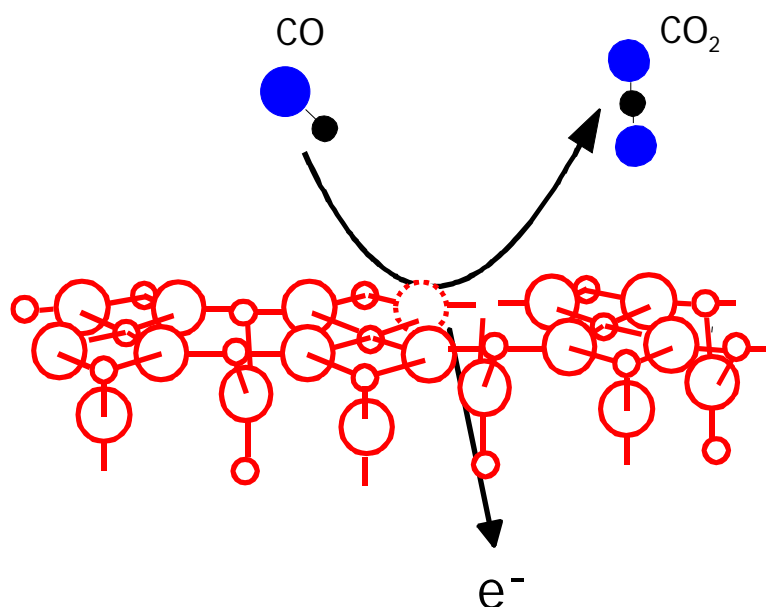


Figure 4.31: A possible reaction mechanism for the CO sensing. CO reacts with the surface oxygen ion. In this process an electron is released.

One of the reactions on the surface is between CO and surface oxygen (M-O vibration is at around 1000 cm^{-1}). In this case CO molecules can react with surface "lattice" oxygen to CO₂ or/and can react with ionosorbed surface oxygen to CO₂. During the latter reaction, first an intermediate product CO₂⁻ can be generated, which desorbs to CO₂. In the last step, an electron will be released to the bulk, which causes changes of the conductivity. Both possible reaction pathways are presented in Figure 4.31 and Figure 4.32. CO₂ is the reaction product of the interaction.

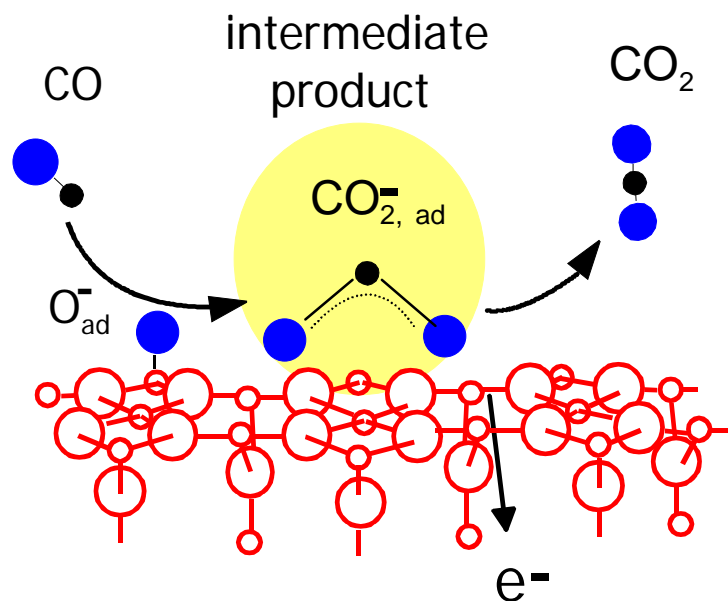


Figure 4.32: An intermediate product was identified by the reaction between CO and the tin oxide surface. CO_2^- is formed probably during the reaction between CO and ionosorbed oxygen species, which reacts to CO_2 in the gas phase under release of an electron into the bulk.

Another possible reaction is between CO and molecular oxygen ions (O_2^- localized at Sn^{2+} (1045 cm^{-1})). In this reaction, bridged bidentate carbonates are formed, which dissociate in the presence of further CO molecules to gaseous CO_2 . Also in this reaction step an electron will be given into the bulk, which contributes to the conductivity. In this work, CO_3^- ions are also identified as intermediate products, since they immediately lose their intensity in air after CO exposure. A cartoon presentation is given in Figure 4.33.

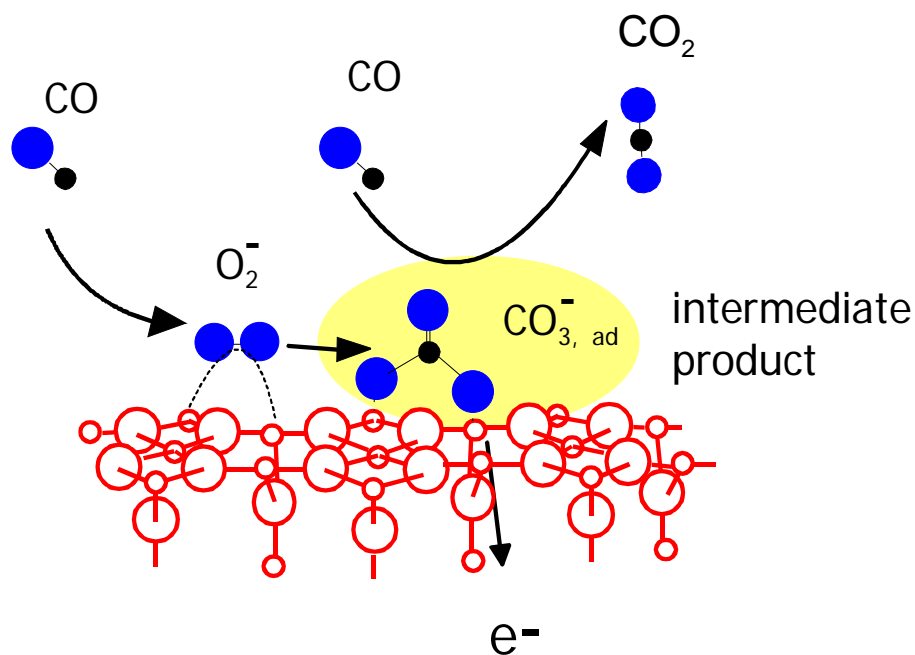


Figure 4.33: A second possible reaction mechanism for the CO sensing. CO reacts with surface oxygen ions (O_2^-) to surface carbonate give CO_2 in the reaction with further CO.

The experimental results indicate a clear interaction between CO and surface hydroxyl groups. The hydrogen atom of those hydroxyl groups is set free and reacts with the neighbouring water molecules, which leads to the creation of hydrated protons and their higher homologues like $H_5O_2^+$. Pictorial presentation of the reaction is shown in Figure 4.34.

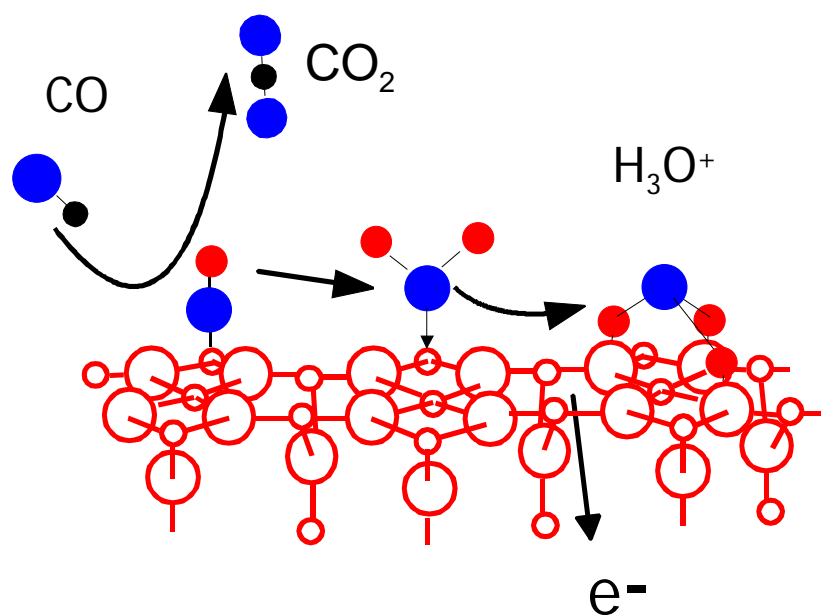


Figure 4.34: Schematic presentation of the reaction that takes place between CO, surface hydroxyl groups and water molecules.

At 150°C, the intensity of the already reacted hydroxyl groups in dry air was high. Probably, at this temperature in dry air and in the presence of very low humidity (4% r.h.) on the surface, enough water molecules were present, which can be protonated by different hydroxyl groups. Probably 150°C is too low for the dissociation of water molecules to differently bound hydroxyl groups. When the temperature is increased to 300-350°C a dissociation of water molecules takes place on the surface, which makes an interaction between CO and hydroxyl groups possible. This fact indicates that for optimized sensing the presence of the surface hydroxyl groups and surface water is a major precondition.

During the CO measurements on powders, a decrease of a specific hydroxyl group was observed. However, on the sensor surface an interaction between CO and a specific hydroxyl group was not observed: CO reacts with all sort of surface hydroxyl groups. Since the time resolution of the spectrometer was not sufficient for the kinetic investigation, no additional information, as found for the powders shown in Figure 4.16, was obtained about the correlation between the surface species on the sensor.

4.1.4.2.3 CO-CO₂ Equilibrium in the Pores of the Sensitive Layer

Gaseous CO and CO₂ were identified in the pores of the samples as described in chapter 4.1.3.3. In order to get additional information which can give a hint for example about the catalytic conversion, quantitative band analysis was performed for CO and CO₂. For the band analysis, spectra in "*-log Reflectivity*" were used, since these gases are not adsorbed species. In Figure 4.35 the changes of the peak areas are shown corresponding to the concentration of CO and CO₂ as a function of dosed CO concentration at different humidity levels at 150 and 300°C. Only at 350°C, it was not possible to perform a band analysis, because of the bad signal-to-noise ratio and low intensity of the bands, especially in the lower concentration range (up to 125-250 ppm CO exposure). A linear relationship was observed between peak areas corresponding to the concentration of the species and the exposed CO concentration. At 150°C it was not possible to recognise the influence of the humidity on the CO-CO₂ equilibrium. It seems that the humidity does not play a role in the CO-CO₂ equilibrium at this temperature.

At 300°C, equilibrium between CO and CO₂ in the pores of the sensitive layer was assumed, which was also clearly observed on the same type of sensor in the previous investigations [109]. At 300°C in dry air, the CO₂ is influenced by the humidity. A clear influence of the humidity on the CO concentration is hardly to be seen due to the low signal to noise ratio in the spectra. This result is surprising since - as has been shown by the resistance measurements - the sensor signal increases in the presence of humidity. Extensively performed consumption measurements [85] on bare substrate, substrate provided with electrodes and heater, bare substrate with sensitive layer (sensitive layer is Pd doped SnO₂ with the average grain size 10 nm) on top and complete sensors (Pd-doped sensor) showed that only the substrate with electrodes and heater showed the strongest humidity

dependence. The consumption by the complete sensor decreases with increasing humidity but not so strong as in the case of alumina substrate provided with electrodes and heater. The gas interaction is proposed in the following way: The CO containing gas flow reaches the sensitive layer where part of CO is combusted. The gas penetrates into the porous layer and reaches the interdigitated electrodes, where again part of the reaction takes place. Moreover, combustion at the heater and uncovered part of the electrodes takes place. In this study it was also found that the consumption of the sensor is not the sum of the independent contribution of the sensitive layer, but the substrate and sensitive layer interact in some way.

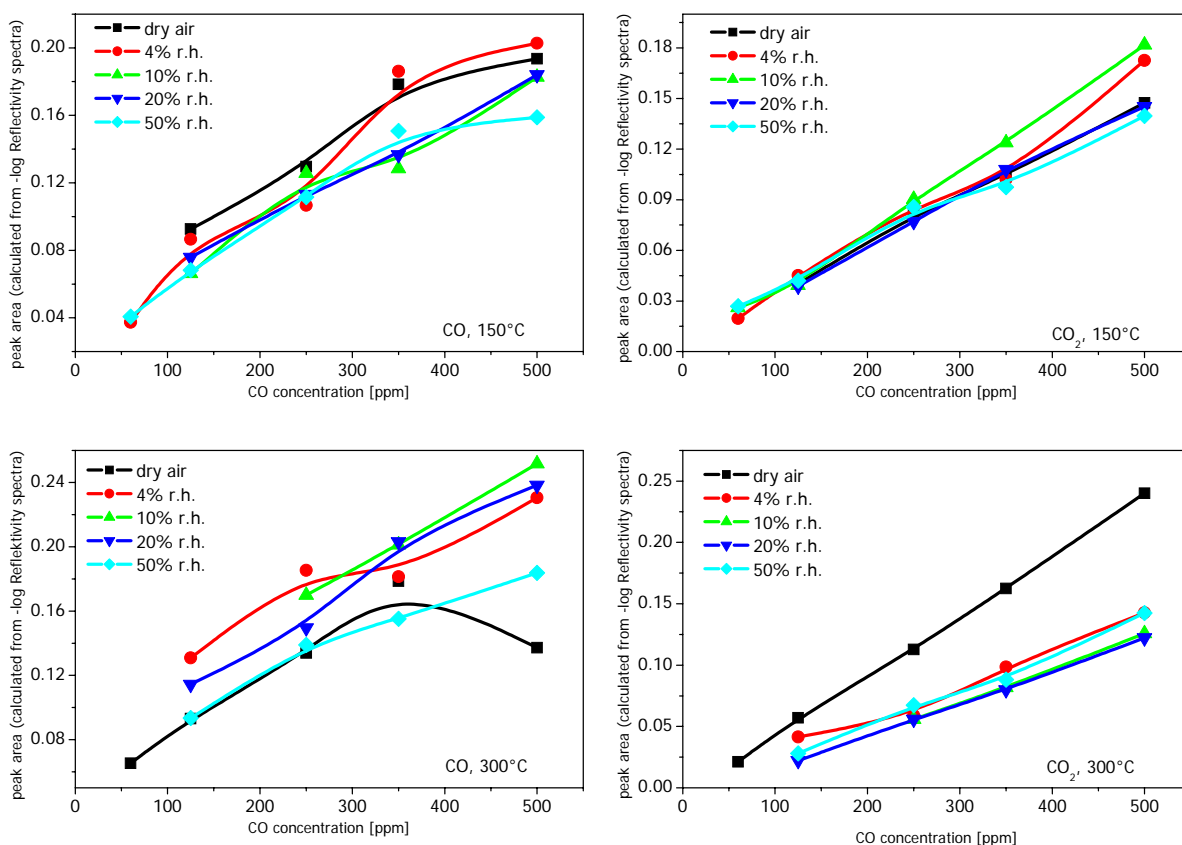


Figure 4.35: Results obtained by band analysis for CO (left) and CO₂ (right) at 150 (top) and 300°C (bottom) at different humidity levels (0-50% r.h.) In the diagrams for the unconsumed CO, the points deviate from the linear course, since the CO rotation fine structure appears in the same spectral range in the spectrum as the H₅O₂⁺ (Zundel structure), especially in the presence of humidity.

4.1.4.2.4 Summary

The sensor surface in the presence of CO was characterized by DRIFT and DC measurements at various temperatures and humidity levels.

At all temperatures the reaction products are the same, only the intensity or the concentrations of the surface species differ. At 150°C, the intensity of the bands belonging to the reaction products, hydrated proton species (H_3O^+), carboxylate (CO_2^-) and bridging carbonates (CO_3), decrease with increasing humidity levels. Obviously, 150°C is too low in order to dissociate water molecules into the different types of hydroxyl groups. Probably undissociated water hinders the interaction between CO molecules and active surface sites. This indicates also that there is no direct reaction between water and CO.

A different equilibrium between CO and CO_2 located in the pores was not observed at all investigated temperatures. It was observed that the CO/ CO_2 equilibrium is not influenced by the humidity at low temperatures, but at high temperatures due to the electrodes. The data for CO_2 at 300°C and 350°C could be interpreted, but the CO data are less informative due to the low signal to noise ratio of spectra. The humidity effect is much more evident in the Pd-doped case.

In the CO vibration spectral range, neither bands belonging to physisorbed CO nor carbonyl complexes (Sn-CO) were detected on the SnO_2 sensor surface at the examined temperatures and humidity levels.

4.1.4.3 CO Measurements on Pd-doped Sensor

The same set of CO experiments was performed on the Pd-doped sensor in order to examine the effect of the dopant on the CO sensing mechanism. Additionally to DRIFT and resistance measurements, a FTIR Photo Acoustic Spectrometer (PAS) was mounted within the flow behind the FTIR spectrometer. The aim of this addition was to analyse the exhaust gases and thus get information about the catalytic conversion of the sensor in

parallel to DRIFT and resistance measurements. Detailed conversion investigations on the same type of Pd-doped sensor are described in [110].

Spectra of Pd-doped sensors recorded at different temperatures and at different humidity levels are essentially similar to the spectra of un-doped ones. All spectra of the un-doped sensors recorded under different conditions were shown and the spectral features were described in detail in the last chapter. Therefore, in the following not all spectra of the Pd-doped sensor will be shown and only selected spectra will be presented. Instead of spectra, the results of the quantitative analysis for Pd-doped sensor are illustrated and compared with the results obtained for the un-doped sensor. The comparison of the results obtained both by the DRIFT and resistance measurements show the role of the catalyst.

4.1.4.3.1 CO effect in the Presence of Humidity at Different Temperatures

Figure 4.36 shows spectra of a Pd-doped sensor at 150°C in the presence of humidity and 500 ppm CO separated in three spectral regions. Spectra recorded in the absence of CO just before CO exposures were used as reference as in the case of un-doped sensor. As mentioned in the experimental part negative bands mean a relative decrease of the band intensity and positive bands mean a creation or a relative increase of the band intensities. In the spectral range between 4000 and 3000 cm^{-1} the intensity of all bands - those ascribed to terminal, rooted hydroxyl groups, associated hydroxyl groups and water molecules - decrease in the presence of CO. With increasing humidity the concentration of the hydroxyl groups involved in the reaction increases. In the middle spectral range, between 3000 and 2000 cm^{-1} , the appearance of bands corresponding to hydrated proton species and to gaseous CO_2 and CO was observed. In the spectral range between 2000 and 850 cm^{-1} , what was detected was a decrease of the bands belonging to oxygen species. They are very sharp and therefore

almost all maxima of the individual absorption bands can be clearly distinguished. In the case of the un-doped sensor, the absorption bands between 1200 and 850 cm^{-1} showed a relatively broad absorption with several shoulders. In the spectra of the Pd-doped sensor, the decrease of the absorption bands corresponding to M-O vibrations (970, 1060 cm^{-1}) in the presence of humidity is clearly to be seen. This is an indication that the lattice oxygen on the surface reacts with CO.

Additionally, the appearance of the bands belonging to surface carbonates and carboxylates was detected.

At 150°C, with increasing humidity the following intensity changes were observed in the spectral range between 4000 and 850 cm^{-1} . The intensity of the consumed reactants (hydroxyl groups, different oxygen species) as well as the reaction products (hydrated proton species, the carbonate related species) increase. However, the intensity of gaseous CO and CO₂ decreases with the increasing humidity level. In the case of the un-doped sensor, the opposite behaviour was observed at this temperature; namely a decrease of all band intensities corresponding to already consumed hydroxyl groups, as well as different oxygen species and the decrease of band intensities corresponding to reaction products (surface carboxylates, carbonates and hydrated proton species). A possible explanation could be the availability of hydroxyl groups through the enhanced dissociation of the water molecules, even at this low temperature.

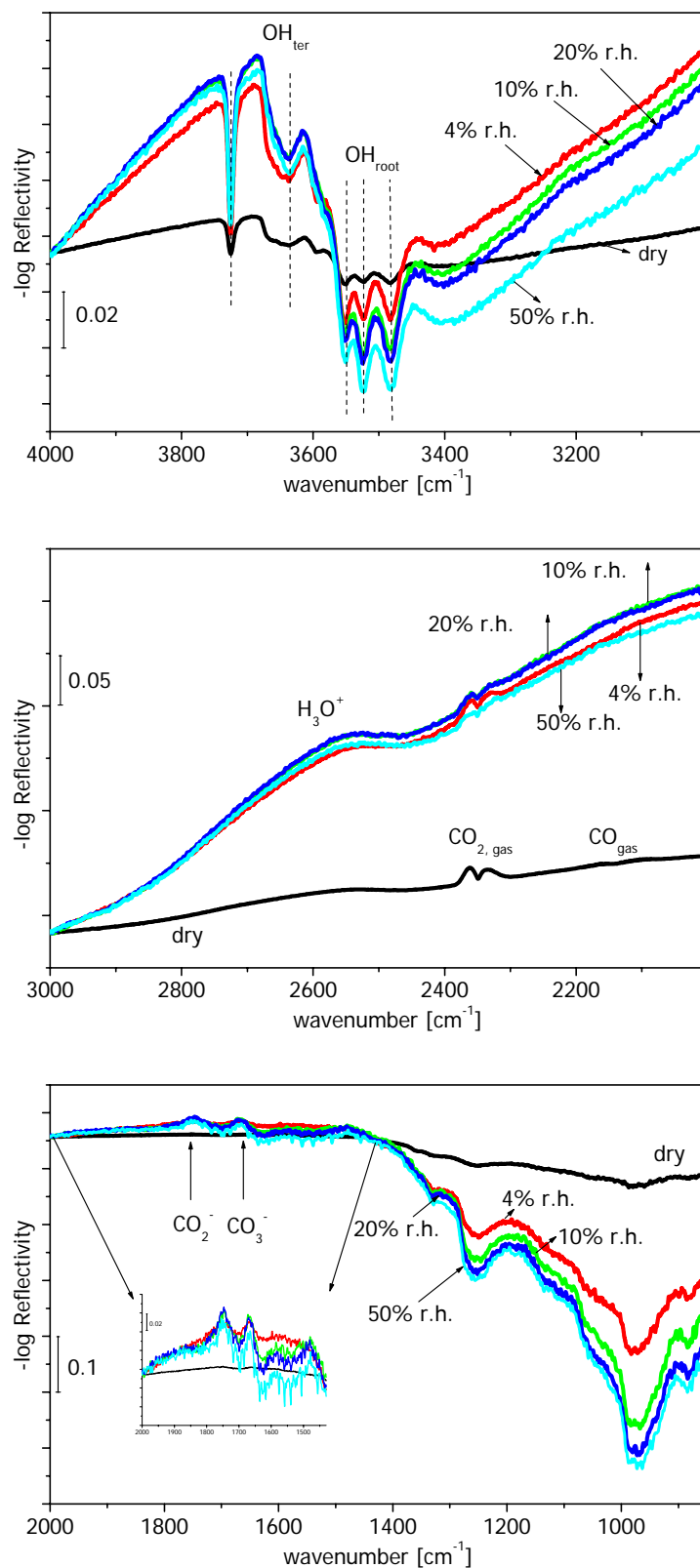


Figure 4.36: Spectra recorded at 150°C at different relative humidity levels during 500 ppm CO adsorption. Top: OH/H₂O spectral region, middle: spectral region between 3000 and 2000 cm⁻¹, bottom: Spectral region between 2000 and 850 cm⁻¹.

The changes of the spectra recorded at 300, 350°C at different humidity levels in various CO concentrations are in general similar to spectra recorded at 150°C. Only the magnitude of the changes differs. Figure 4.37 shows the band analysis results for surface hydroxyl groups, oxygen ions, hydrated proton species, carboxylate and bridged bidentate carbonates at different temperatures and humidity levels in the presence of 350 ppm CO. The lowest relative change of the band intensities belonging to educts and products is detected in dry air at all examined temperatures. In the presence of humidity, the relative changes of the intensity corresponding to the reaction products (H_3O^+ , H_5O_2^+ , CO_2^- , CO_3^-) become more pronounced.

At 150°C the maximum of the relative changes of the band intensities is at 20% r.h. Both the intensity of the educts and products seem to reach saturation (no difference between 20 and 50% r.h.).

At 300°C and 350°C, the relative changes of intensity corresponding to surface species show an almost linear increase with the humidity.

From the diagrams shown in Figure 4.37, a correlation among educts and products is not as clear as for the un-doped sensor at low temperature (150°C).

It should be kept in mind that the concentration of the different O_2^- ions should be very low at 300 and 350°C. At these temperatures, O^- -ions are on the surface and the reaction between CO and O^- should be dominant, most probably via carboxylate ions.

Characterisation of the Samples

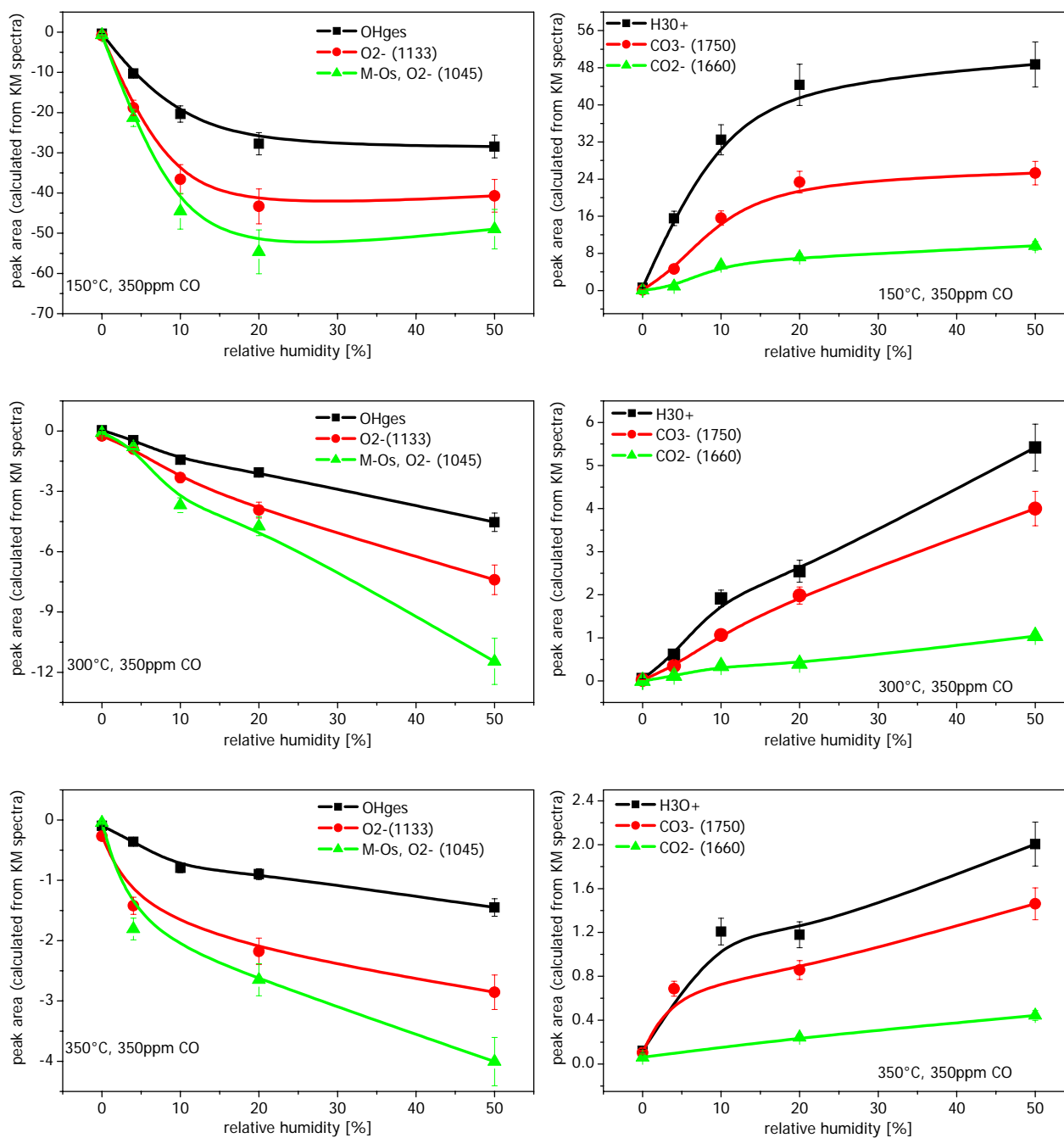
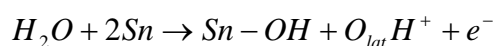


Figure 4.37: Results obtained by band analysis for hydroxyl groups (OH), different oxygen species (O₂⁻) (Educts, left column), hydrated protons (H₃O⁺), carboxylates (CO₂⁻), bridging carbonate (CO₃⁻) (products, right column) at 150°C (top), 300°C (middle), 350°C (bottom).

Figure 4.38 shows the resistance of the sensor in air, at different CO concentrations and humidity levels at 150° (top) and 300°C (bottom). The sensor resistance decreases with increasing humidity at all examined temperatures, which is explained by the following reaction on the basis of literature, work function and conductance measurements on the same type of sensor [85] and on the basis of our results obtained by DRIFT spectroscopy:



From the raw data one can easily see that the sensor resistance deviates from the original value and the recovery time of the sensor is getting longer with increasing humidity level at low temperatures. Moreover, the response time of the sensor resistance is not influenced by the humidity. At higher temperatures, the sensor resistance stays stable at all humidity levels. Both the recovery time and the response time of the sensor are very short and not affected by humidity.

Furthermore, the decrease of the resistance increases in the presence of humidity. This higher sensibility in humid air is explained by a possible reaction found in the previous detailed studies using work function and conduction measurements on the same type of sensor [9, 85]: CO reacts with water related species under the release of electrons. In these investigations performed on Pd-doped sensor it was found that this reaction dominates at lower temperatures since the concentration of the oxygen ions (O^-) is too low at low temperatures, while the reaction between CO and oxygen ions (O^-) makes a major contribution to the sensitivity at high temperatures.

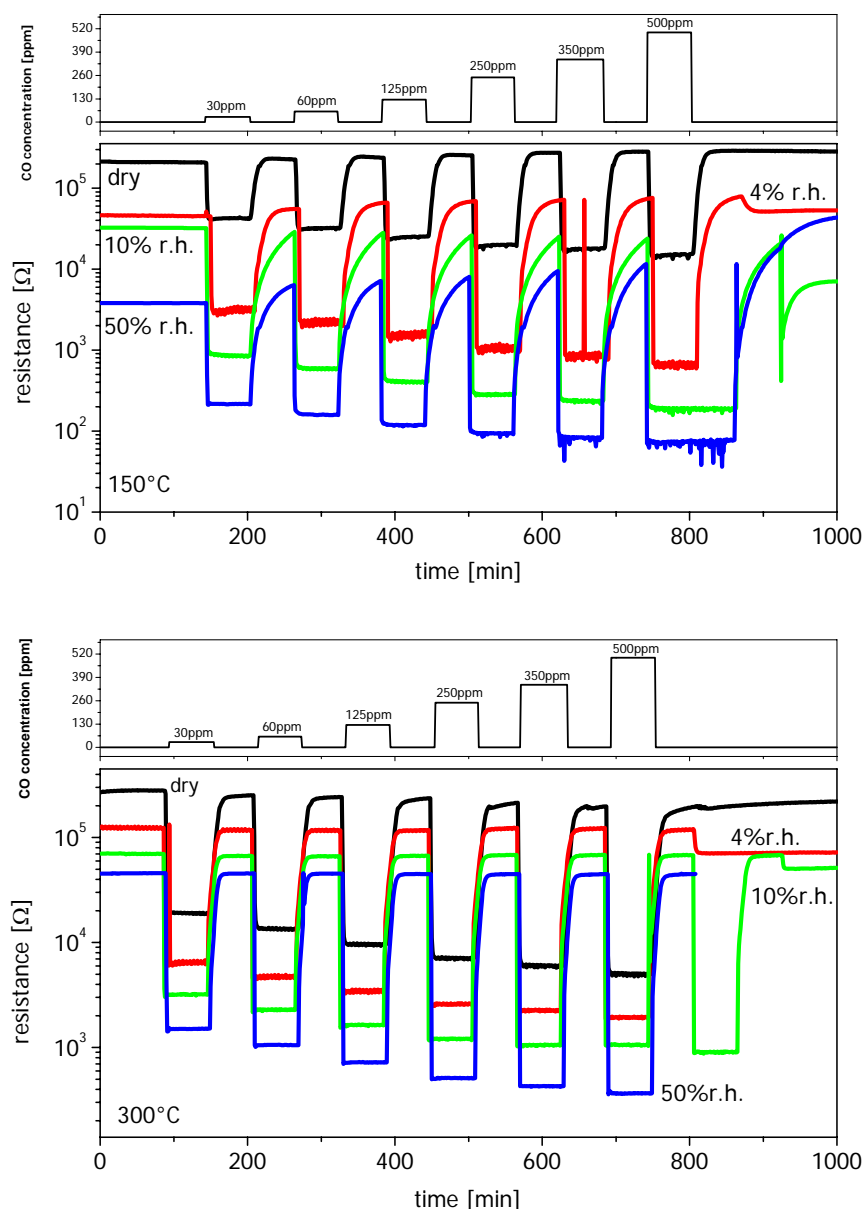


Figure 4.38: Resistance of the Pd-doped sensor at 150 (top) and 300°C (bottom) in the presence of humidity and various CO concentrations.

Comparing the sensor signal with the concentration of hydrated proton species indicates that both are well correlated (Figure 4.39). The results obtained by DRIFT spectroscopy also indicate that CO reacts with surface hydroxyl groups. However, the strong and obvious correlation between sensor signals and hydrated proton species confirms the reaction mechanism proposed in this research and described above for the un-doped sensor: CO reacts with surface terminal hydroxyl groups to CO_2 and releases hydrogen atoms. These react with the neighbouring surface water

molecules to H_3O^+ that are donors, instead of the rooted hydroxyl groups supposed on the basis of phenomenological measurements. In the DRIFT spectra no indication was observed towards creation of rooted hydroxyl groups by CO reaction.

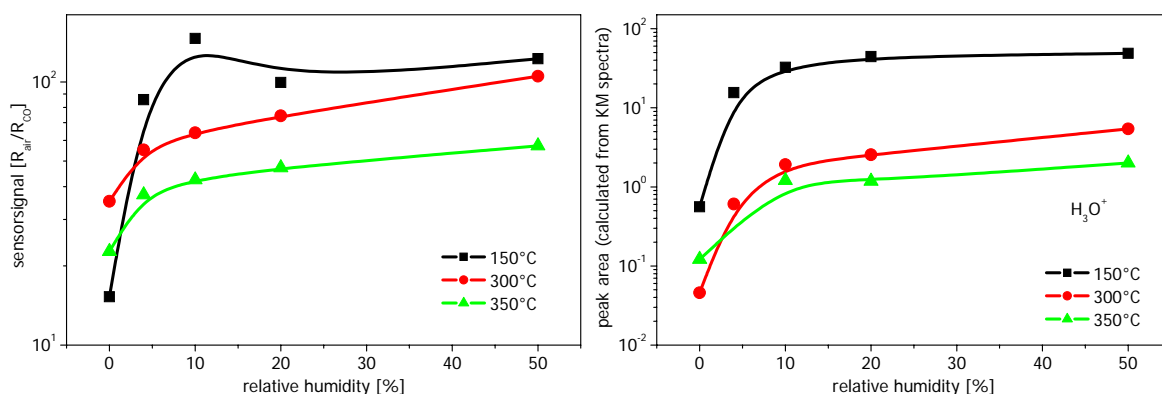


Figure 4.39: Sensor signal (left) and peak area of hydrated proton species (right) as a function of relative humidity for 350 ppm CO at different temperatures.

In Figure 4.40, the sensor signal and the intensity changes of the broad band at 1933 cm^{-1} are presented as a function of humidity.

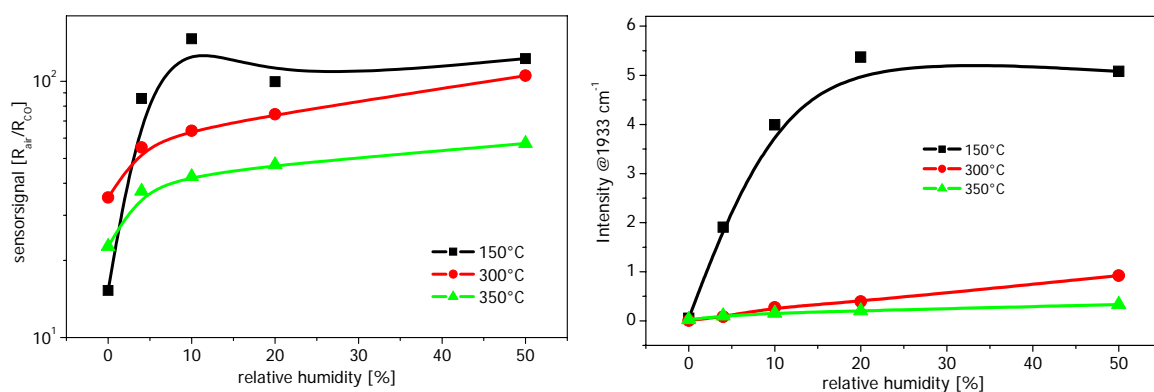


Figure 4.40: Sensor signal as a function of humidity at different temperatures (left) and intensity of the broad band at 1933 cm^{-1} (right).

Also, as in the case of the un-doped sensor, for the Pd-doped sensor a correlation between the sensor signal and the intensity of the broad absorption covering almost the total MIR range was observed. From both graphs one can see that the highest sensor signal and maximum changes in the band intensity were in the presence of humidity at the lowest temperature investigated in this research. At 150°C the sensor signal

increases almost linearly between dry air and 10% r.h., then it reaches saturation. Similar behaviour was observed, if the intensity of the broad absorption was plotted versus humidity.

Figure 4.41 and Figure 4.42 present the spectra which were recorded in dry air and in the presence of 50% r.h. after CO exposure at 150 and 300°C respectively. The spectrum recorded before CO exposure in the corresponding temperature and humidity is used as reference spectrum. In all spectra no absorption bands are detected, which indicates that the surface has completely regenerated. Looking at the resistance data at different temperatures and humidity levels presented in Figure 4.38, one can see that the resistance values in all measurement conditions at 300°C reach similar resistance value after one hour purging with dry/humid air. However, this is not the case in the measurements conducted at 150°C in the presence of humidity. The sensor generally needs a longer recovery time in the presence of humidity.

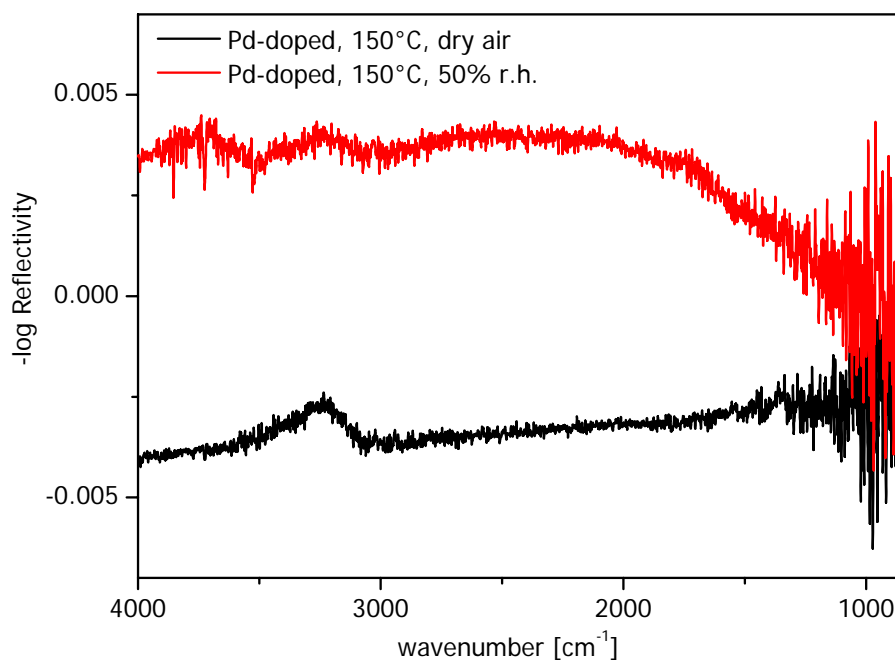


Figure 4.41: Spectra recorded after the exposure to CO in dry and humid air at 150°C. The spectrum recorded before the CO pulse was used as reference.

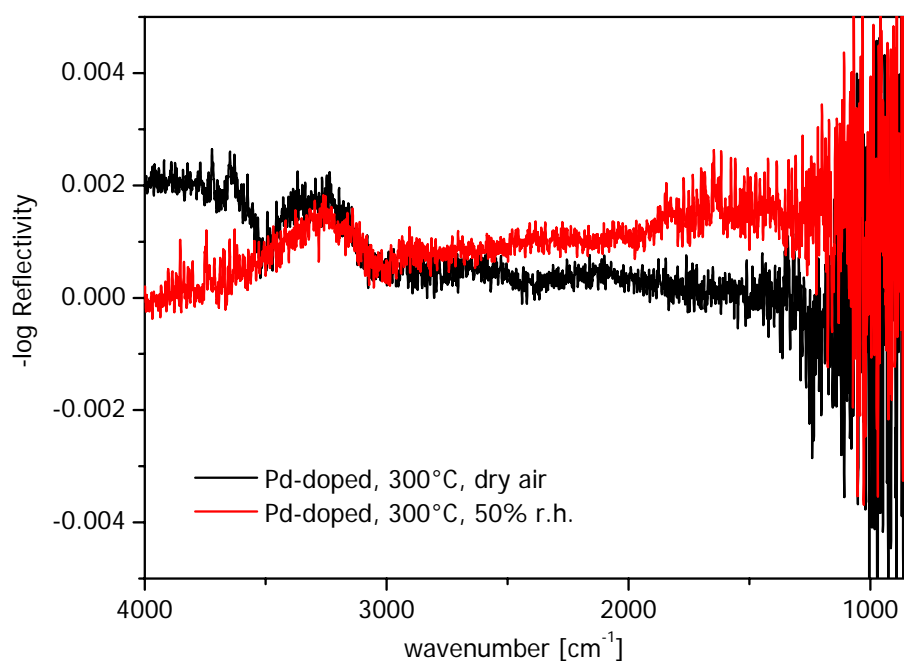


Figure 4.42: Spectra recorded after the exposure to CO in dry and humid air at 300°C. Spectrum recorded before CO pulse was used as reference.

4.1.4.3.2 CO-CO₂ Equilibrium in the Pores and in the Exhaust

Also for Pd-doped sensor, gases (CO, CO₂ and H₂O) in the exhaust were analysed additional to the one (CO, CO₂) in the pores. The main aim of this experiment was to monitor the system and get additional information about the CO-CO₂ equilibrium after the sensing processes, i.e. information about the catalytic conversion associated with the CO sensing.

Figure 4.43 presents the results, obtained by DRIFT: gaseous CO and CO₂ are located in the pores of sensitive layers. At all temperatures, one can see a clear influence of the humidity on the CO/CO₂ equilibrium, in contrast to the case for the un-doped sensor. On the un-doped sample, no humidity effect was observed at low temperature, and at higher temperatures the signal to noise ratio of the spectra was bad which leads to difficult data interpretation and makes it more difficult to see the influence of the humidity on the CO consumption. At 150°C and 300°C, the highest signal for CO₂ was obtained in dry air. With increasing humidity the generation of CO₂ decreases. As mentioned above for the un-doped sensor, the decrease of the CO₂ concentration in humidified air is due to electrodes working as some kind of additional doping, which was found on the basis of consumption measurements performed on different samples (bare alumina substrate, alumina substrate provided with electrodes and heater, bare alumina substrate plus a SnO₂ layer on top, complete sensor) [85]. In the graph for CO, the starting points of the curves deviate from each other much more than for the CO₂-curves (Figure 4.43). This can be explained by the overlapping of the CO band with that of the H₅O₂⁺-ions. This makes it difficult to conduct a precise band analysis.

One should note that it was not possible to evaluate the data for 4 and 10% r.h., due to the very bad signal-to-noise ratio.

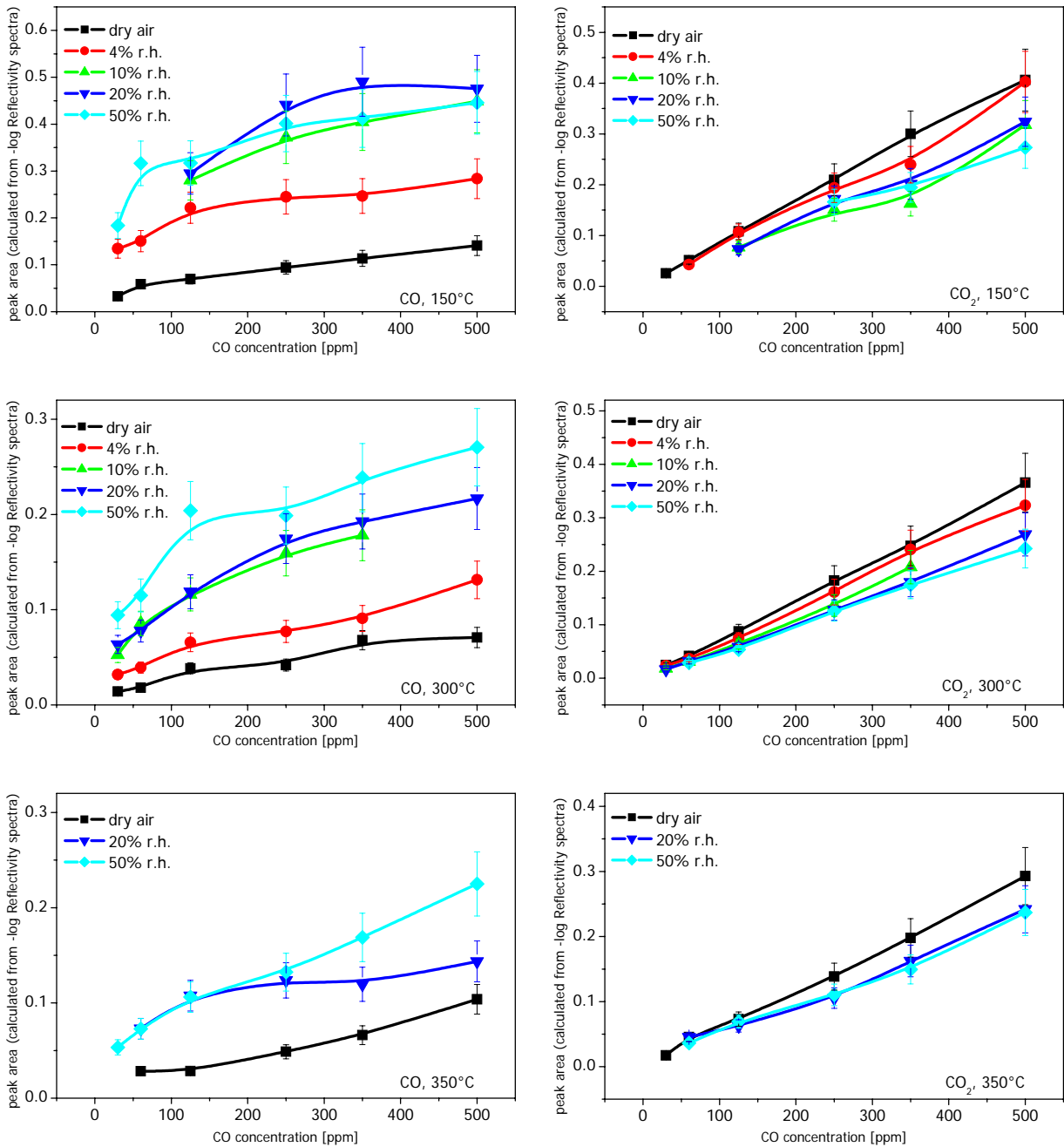


Figure 4.43: Results of band analysis for CO (left column) and CO₂ (right column) at different temperatures and humidities. Top: 150°C, middle: 300°C, bottom 350°C.

Figure 4.44 shows the data recorded with a photoacoustic spectrometer corresponding to the resulting gas concentration in the exhaust after the sensing took place. The sensor temperature was 150°C and the relative humidity was 20% r.h. The diagram shows the concentrations of CO and CO₂ gases in the exhaust (after 30, 60, 100, 250, 350, 500 ppm CO

exposure). As described above, CO in different concentrations was delivered to the sensor for one hour (350 ppm CO was exposed for 2 h); in the diagram one can see that the signal reaches the equilibrium only after one hour. This fact is due to the volume of the sampling bag of the photo acoustic spectrometer.

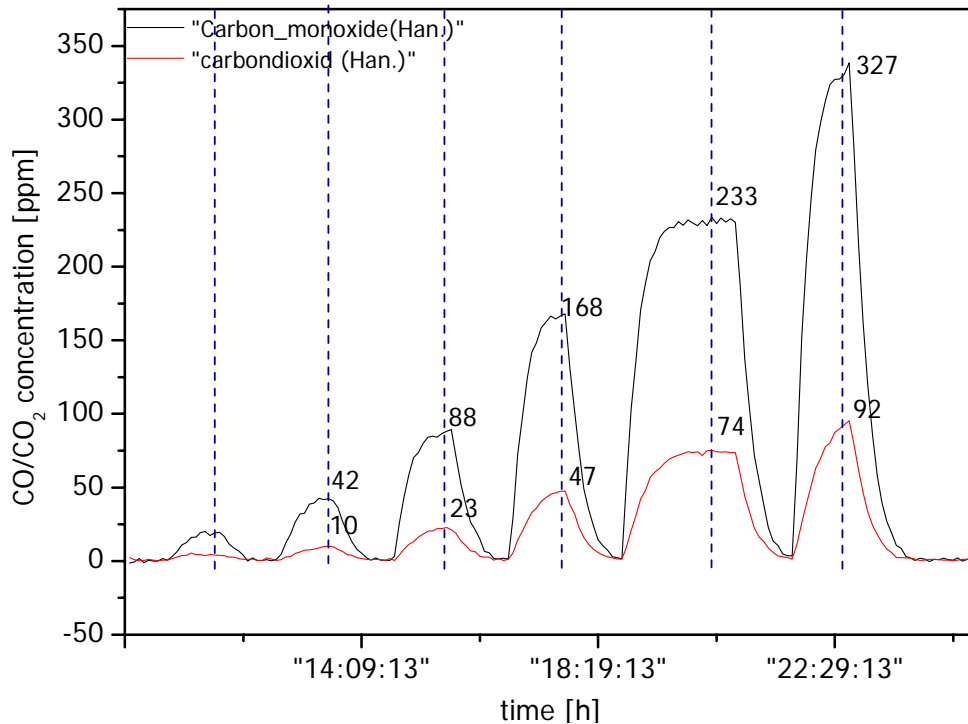


Figure 4.44: CO-CO₂-Equilibrium in the exhaust. Pd-doped sensor at 150°C in humid air (20% r.h.). Data is recorded using a photoacoustic infrared spectrometer.

Evaluated data for the CO and CO₂ concentrations, in the exhaust as a function of exposed CO concentration are presented in Figure 4.45. At 150°C the CO₂ concentration depends on the humidity. The higher the humidity level, the lower the CO₂ concentration. Also at 300°C, the concentration of CO increases and the concentration of CO₂ decreases in the exhaust in humidified air, but the humidity influence is not so high as at 150°C. At 350°C, the influence of the humidity on the CO concentration in the exhaust is smaller than at 150 and 300°C and the influence of the humidity on the CO₂ concentration is negligible. This result is not in agreement with the results obtained by the consumption measurements performed on the same type of sensor, where the effect of the operation

temperature (200-400°C) on the consumption was studied. By this investigation a stronger humidity influence on the CO consumption at higher temperatures was found. For the explanation of this effect there is a need for additional measurements.

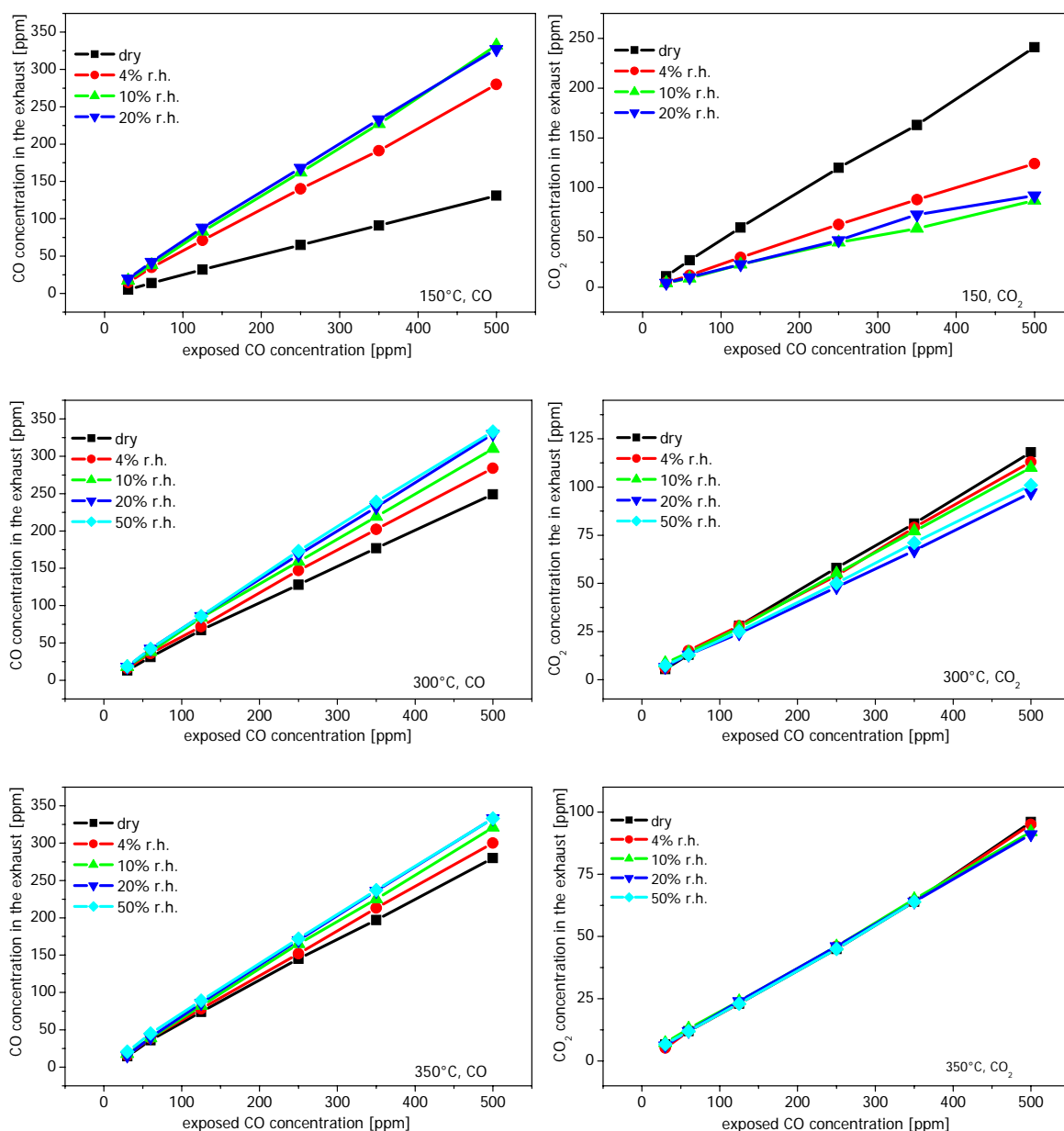


Figure 4.45: CO and CO₂ concentration as a function of exposed CO concentration at various humidity levels.

Results of quantitative analysis for the gaseous CO and CO₂ obtained by parallel recorded DRIFT spectra (as far they can be evaluated) and photo acoustic spectroscopy are to a large degree in agreement.

4.1.5 Comparison of the Un-doped and Pd-doped Sensor

Figure 4.46 presents an overview of the results of the band analysis and the sensor signal for Pd-doped (left column) and un-doped sensor (right column) at 150°C for 350 ppm CO.

In the case of the un-doped sensor, the difference of the intensity corresponding to hydroxyl groups and surface oxygen species decreases with increasing humidity, for the Pd-doped sensors the opposite tendency is the case. Accordingly, the higher the humidity level, the lower are the intensity changes corresponding to the reaction products (H_3O^+ , CO_2^- , CO_3^-) for the un-doped material. In the case of Pd-doped material, the intensity changes of the reaction products (H_3O^+ , CO_2^- , CO_3^-) increase with increasing humidity.

The intensity changes of the surface species are nearly ten times higher in the case of the Pd-doped sensor. Also, the results obtained by the resistance measurements are in very good agreement with the spectroscopic results. The sensor signal of the un-doped sensor decreases with increasing humidity levels at 150°C, but the sensor signal of the Pd-doped sensor increases with increasing humidity levels and the effect is also ten times stronger.

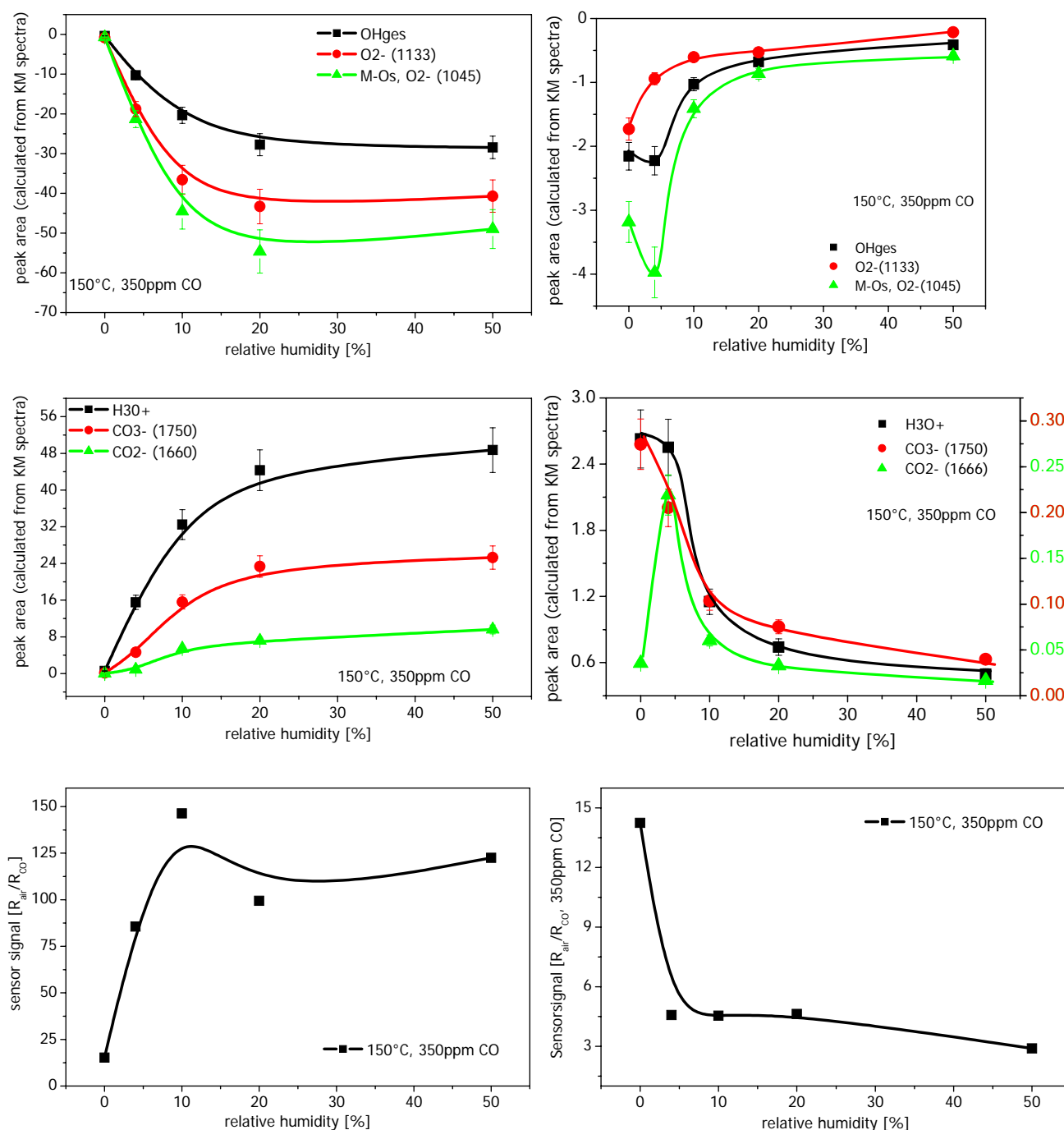


Figure 4.46: Results obtained by DRIFT spectroscopy and resistance measurements and at 150°C on the Pd-doped (left) and un-doped sensor (right).

Figure 4.47 presents the band analysis results for surface species involved in the reaction with CO and electrical resistance changes at 300°C.

The maximum changes of the band intensity were observed in 4% and 10% r.h. in the case of un-doped sensor. At high humidity such as 20 and 50% r.h. the intensity changes are smaller and comparable with those in

dry air. For the Pd-doped sensor, we found a nearly linear increase of the intensity changes with increasing humidity. The highest sensor signal was obtained also at 10% r.h for un-doped sensor but at 50% r.h for Pd-doped ones. Therefore, the spectroscopic and electrical results are in very good agreement.

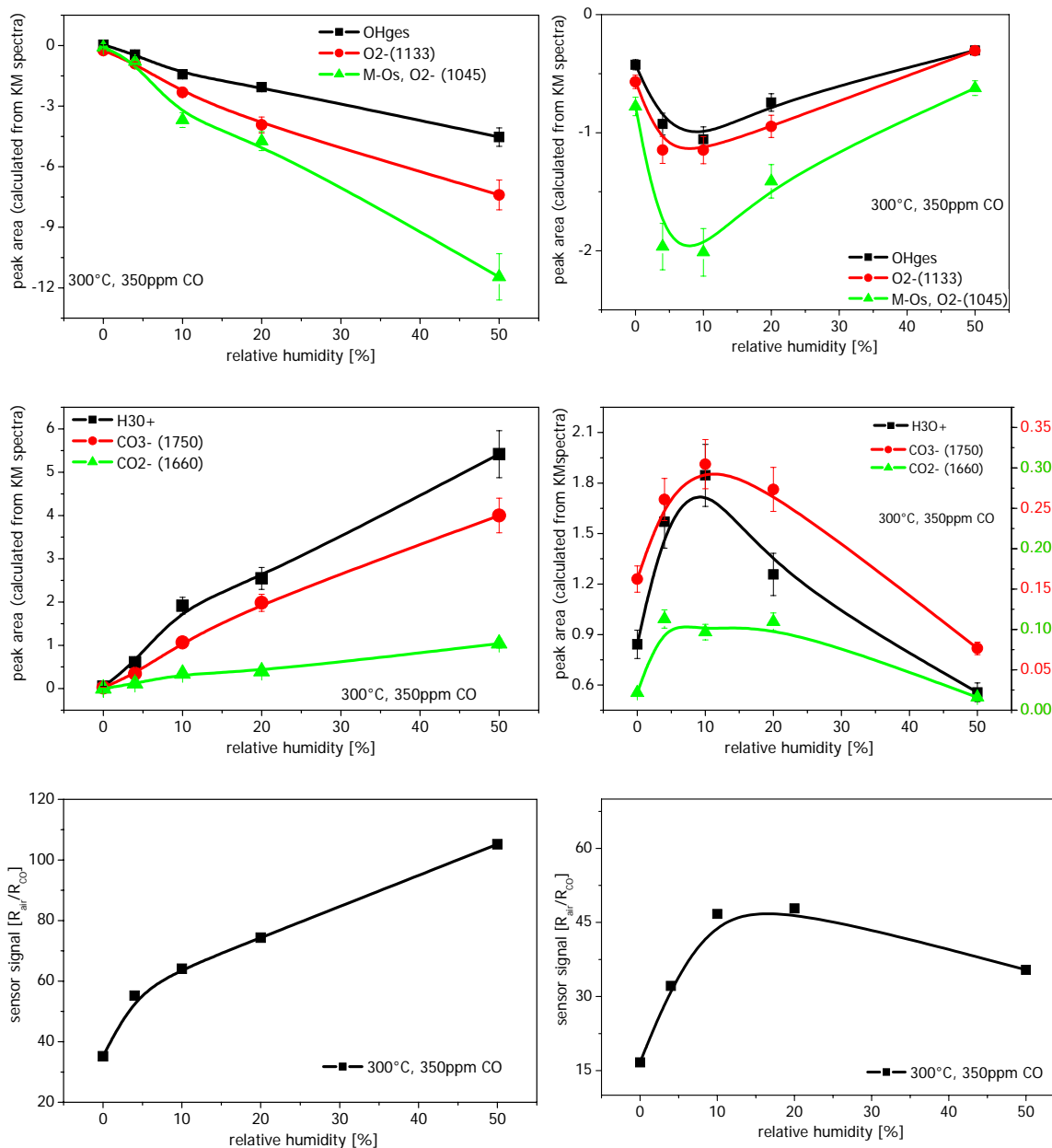


Figure 4.47: Results obtained by DRIFT spectroscopy and resistance measurements and at 300°C on Pd-doped (left) and un-doped sensor (right).

Figure 4.48 presents the band analysis results for surface species involved in the reaction with CO and electrical resistance changes at various humidity levels and a sensor temperature of 350°C.

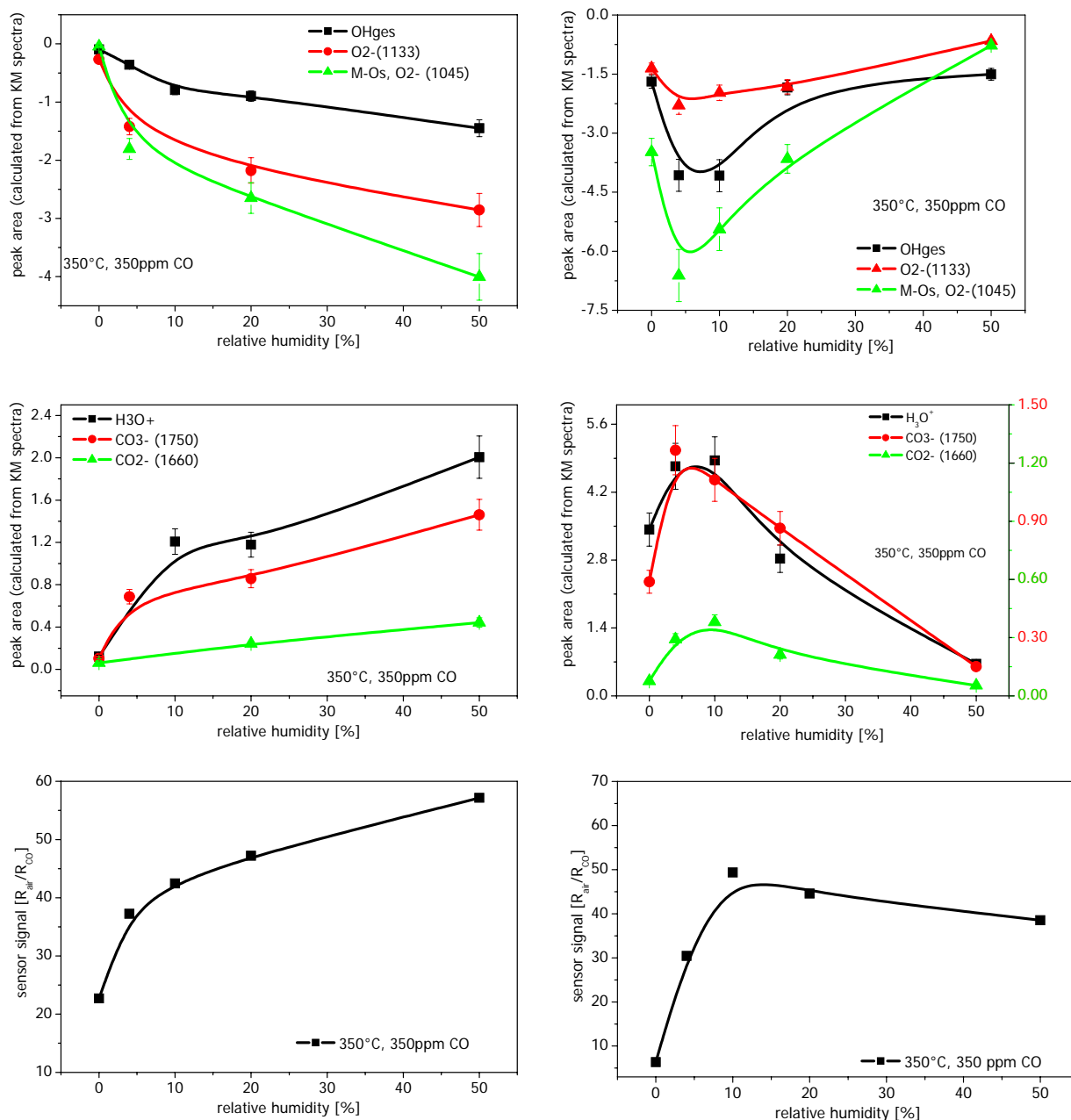


Figure 4.48: Results obtained by DRIFT spectroscopy and resistance measurements and at 350°C on Pd-doped (left) and un-doped sensor (right).

The results at 350°C are very similar to the results at 300°C. In the case of the un-doped material, the maximum intensity changes are obtained at

low humidity levels. At higher humidity, the relative changes of the band intensity strongly decrease. In the case of Pd-doped sensor, the intensity of the changes increases with increasing humidity.

As a summary, it can be seen that both types of sensors show a different dependency on humidity at different temperatures. The amount of the decrease of the reactant concentration and increase of the product concentration is much higher in the case of Pd-doped sensor than in the case of un-doped ones. Comparing the values of the concentration of the products, for the Pd-doped the maximum is at 300°C in the presence of 50% r.h., for the un-doped one at 300°C in the presence of 10% r.h. Also, the concentration of the H_3O^+ -ions is four times higher in the case of Pd-doped sensor than in the case of an un-doped one.

5 Conclusions and Outlook

The studies presented in this work have shown that thick film sensors can easily be characterised in different working conditions (at elevated temperatures, in the presence of humidity) using Diffuse Reflectance Infrared (DRIFT) spectroscopy. Due to its sensitivity to surface species chemical compounds involved in the gas reaction were detected. This would not have been possible with other methods. In this research, un-doped and Pd-doped SnO₂ sensor surfaces were characterized at different temperatures using two different methods in parallel: DRIFT spectroscopy and electrical measurements. Simultaneous recording of the DRIFT spectra and the sensor resistance helped to clarify the role of the individual surface species in the sensing mechanism. The proposed models for the sensing mechanisms, which were established on the basis of the spectroscopic data in the frame of this study, are only partly in agreement with the previous results obtained by phenomenological measurements on the same samples by other authors. Results of the work presented here show that several reactions take place in the presence of CO depending both on temperature and humidity. It was found that all surface species are involved in the reactions and it is supposed that parallel and consecutive CO reactions take place on the surface.

In addition to identifying the chemical compounds, it was clearly demonstrated that one also obtains further information on e.g. the CO/CO₂ equilibrium in the pores and its humidity dependency, which corresponds to the CO consumption during the reaction.

In the following, reaction mechanisms proposed for low and high temperatures as well as the influence of the catalyst and humidity on the reaction with CO are summarised.

5.1 Reaction Mechanism at Low Temperature (150°C)

5.1.1 In the Absence of Humidity

At low temperature, various hydroxyl groups, coordinated water and differently adsorbed oxygen species were detected on the surface. The CO oxidation by the ionosorbed reactive oxygen ions (at low temperatures, mainly O_2^- -ions are present on the surface, the concentration of the O^- -ions is very low), which is a well accepted reaction mechanism, is confirmed using DRIFT spectroscopy. CO reacts with ionosorbed oxygen ions to form surface carbonates and carboxylates. On the basis of powder and in-situ sensor measurements it is suggested that those bridged bidentate carbonates and carboxylates are intermediate products of the reaction. The end product of the reaction is CO_2 in the gas phase. Furthermore, it was shown that the active lattice oxygen species (M-O) participate in the reaction with CO.

A second reaction, which takes place in parallel to the above one, was found between CO and hydroxyl groups and water resulting in hydrated proton species and their higher homologues. Both the quantitative band analysis for these species and the sensor signals show a similar extent of changes at higher temperatures (very similar to measurements carried out at 300°C).

On both types of sensors the same reactions take place. Although the sensor signal of both types of sensors is in the same range at low temperature and in dry air, the response and recovery time is much shorter for the Pd-doped sensor.

5.1.2 In the Presence of Humidity

The adsorption mechanism of water proposed by previous other studies are confirmed on the basis of DRIFT spectroscopy. In the case of the undoped sensor, it was found that water dissociates only at very low humidity levels (4 and 10% r.h.). At higher humidity levels, tin dioxide is not able to

dissociate the water molecules into the surface hydroxyl groups and mainly molecular water is present on the surface.

CO exposure to the surface influences both sensor signal and relative intensity changes of the absorption bands in humid air. In both methods, the signal intensity becomes smaller with increasing humidity, which indicates that a direct reaction between CO and molecular water does not take place, e.g. in a water shift reaction, which was proposed for the reaction on ZnO surface at low temperatures.

The picture changes in the case of the Pd-doped sensor. The results obtained by electrical measurements show that the sensor signal increases with higher levels of humidity. The highest sensor signal is obtained at a high humidity level (50% r.h.) for the Pd-doped sensor. The sensor signal is even larger than at higher temperatures. This is explained by the dissociation of water molecules into the various hydroxyl groups even at this low temperature. Moreover, the sensor response and recovery time are short, which are important sensor properties in the field of sensor application. These observation leads to the assumption that the palladium catalyst accelerates the water dissociation and interaction of the surface hydroxyl groups with CO molecules. The quantitative band analysis for the hydrated proton species also shows that the intensity of the hydrated proton species increases with increasing humidity. This indicates a direct correlation between the sensor signal and hydrated proton species.

5.2 Reaction Mechanism at High Temperatures (300 and 350°C)

5.2.1 In the Absence of Humidity

The relative intensity changes of the bands corresponding to surface hydroxyl groups, hydrated proton species and the sensor signal are slightly larger for the Pd-doped sensor at high temperatures. It is supposed that CO reacts almost exclusively with the very reactive ionosorbed atomic surface oxygen ions to form CO₂, which cannot be confirmed with the measurement methods used in this work.

5.2.2 In the Presence of Humidity

The effect of the water on the sensing mechanism is widely clarified by parallel recording of the DRIFT spectra and sensor resistance. At high temperatures, different hydroxyl groups are created on both un-doped and Pd-doped sensor surfaces due to the dissociation of water molecules. The sensor signal, caused by the CO exposure, increases with the humidity. The magnitude of the sensor signal at each temperature and sensor type is different, although the tendency is the same: The largest sensor signal was obtained at 300°C and at 10-20 % r.h. At 350°C, the largest sensor signal was obtained also at 10-20% r.h., but it is smaller than at 300°C. However, the response and recovery time of the sensor is shorter at 350°C. The same behaviour was seen by the quantitative band analysis for the hydrated proton species (H₃O⁺) and their higher homologues (H₅O₂⁺) which were identified in DRIFT measurements. Their intensity increases with increasing humidity at high temperatures in the presence of CO. This high correlation between the sensor signal and hydrated proton species makes clear that the generation of the hydrated proton species leads to additional changes in the conductance. They are new species acting as donors in the sensing mechanisms.

5.3 Outlook

Although this work has clarified the CO sensing mechanism in synthetic air, there is still need for further investigations to advance the understanding of the sensing mechanism on tin dioxide in order to systematically improve sensor performance. This further work could include isotopic oxygen measurements and H/D exchange measurements with deuterated water for a better characterisation of the surfaces. Additionally, further investigations are needed for the interpretation of the broad absorption band appearing in the total MIR range.

DRIFT spectroscopy can be very helpful for a better understanding of the sensing mechanism of the measurements conducted in the background of different carrier gases and/or in the presence of different gases. For example, it has already been shown that the sensor signal rises strongly in a nitrogen background and in very low oxygen concentration [111].

In order to understand the role of substrate and electrodes in gas sensing, measurements should be conducted on substrates (blank and substrate with electrode) under the same conditions.

6 References

1. N. Barsan, M. Schweizer-Berberich, W. Göpel, *Fresenius' Journal of Analytical Chemistry*, 365, 1999, p. 287
2. J. J. Benitez, M. A. Centeno, C. Louis dit Picard, O. Merdrignac, Y. Laurent, J. A. Odriozola, *Sensors and Actuators B*, 31, 1996, p. 197
3. R. Pohle, M. Fleischer, H. Meixner, *Conf. Proc. EUROSENSORS XIII, The Hague (The Netherlands)*, ISBN 90-76699-01-1 (9/1999), p. 115
4. R. Pohle, M. Fleischer, H. Meixner, *Sensors and Actuators B*, 78, 2001, p. 133
5. S. Emiroglu, N. Barsan, U. Weimar, V. Hoffmann, *Thin Solid Films*, 391, 2001, p. 176
6. P. Schuster, G. Zundel, C. Sandorfy, *The Hydrogen Bond II*, North-Holland Publishing Company, 1976, p. 670
7. N. Barsan, A. Heilig, J. Kappler, U. Weimar, and W. Göpel, *Conf. Proc. EUROSENSORS XIII, The Hague (The Netherlands)*, p. 183-184.
8. J. Kappler, A. Tomescu, N. Barsan, U. Weimar, *Thin Solid Films*, 391, 2001, p. 186
9. U. Weimar, *Gas Sensing with Tin Oxide: Elementary Steps and Signal Transduction*, Habilitationsschrift, University of Tübingen, 2001
10. N. Barsan, U. Weimar, *Journal of Physics: Condensed Matter*, 15 (20), 2003, p. R813
11. W. W. Wendland, H. G. Hecht, *Reflectance Spectroscopy*, New York, John Wiley and Sons, 1966
12. R. D. Aines, G. R. Rossman, *American Mineralogist*, 69, 1984, p. 319
13. Kubelka, Munk, *Zeitschrift für Technische Physik*, 12, 1931, p. 593
14. G. Kortüm, *Reflexionsspektroskopie*, Springer-Verlag, 1969
15. P. Kubelka, *Journal of the Optical Society of America*, 38, 1948, p. 448
16. R. Molenaar, T. Bosch, J. Joop, Z. Joop, *Applied Optics*, 38 (10), 1999

-
- 17 G. Glauning, K.-Kovar, V. Hoffmann, *Fresenius Journal of Analytical Chemistry*, 338, 1990, p. 710
 - 18 N. Barsan, U. Weimar, *Journal of Electroceramics*, 7, 2002, p. 143
 - 19 M. Henzler, W. Göpel, *Oberflächen Physik des Festkörpers*, Teubner Verlag, 1994
 - 20 G. Heiland, D. Kohl, *Physical and Chemical Aspects of Oxidic Semiconductor Gas Sensors*, Seiyama (ed.) *Chemical Sensor Technology*, Vol. 1, Kodansha Ltd, Tokyo in Cooperation with Elsevier Science Publisher, Ch. 2 p. 15-38
 - 21 A. A. Davydov, *Infrared Spectroscopy of Adsorbed Species on the Surface of Transition Metal Oxides*, John Willey & Sons, 1990
 - 22 A. A. Davydov, *Molecular Spectroscopy of Oxide Catalyst Surfaces*, John Willey & Sons, 2002
 - 23 A. Zecchina, S. Coluccia, L. Cerruti, E. Borello, *Journal of Physical Chemistry*, 75, 18, 1971, p. 2783
 - 24 S. Lenearts, J. Roggen, G. Maes, *Spectrochimica Acta Part A*, 51, 1995, p. 883
 - 25 D. H. Sullivan, M. P. Harold and W. C. Conner, Jr., *Journal of Catalysis*, 178, 1998, p. 108
 - 26 M. A. Centeno, I. C. Carrizosa and J. A. Odriozola, *Applied Spectroscopy* 53, 1999 (7), p. 800
 - 27 J. L. Solis, A. Hoel, V. Lantto, C. G. Granqvist, *Journal of Applied Physics*, 89, 2001 (5), p. 2727
 - 28 A. Chiorino, G. Ghiotti, F. Prinetto, M. C. Carotta, C. Malagu, G. Martinelli, *Eurosensors XIV*, ISBN 87-89935-50-0, 2000, Copenhagen, p. 129
 - 29 T. S Rantala, S. Tuomo, V. Lantto, T. T. Rantala, *Physica Scripta*, T54, 1994, p. 252
 - 30 D. E. Cox, T. B. Freyberger, S. Semancik, *Physical Reviews B*, 38, 1988, p. 335

-
- 31 J. P. Joly, L. Gonszales-Cruz, Y. Arnaud, *Bulletin de la Societe Chimique de France*, 11, 1986
 - 32 B. Gillot, C. Fey, D. Delafosse, *Journal de Chimie Physique et de Physico-Chimie Biologique*, 73, 1976, p 19
 - 33 N. Yamazoe, J. Fuchigami, M. Kishigawa, T. Seiyama, *Surface Science*, 86, 1979, p. 366
 - 34 A. M. Volodin, A. E. Cherkasin, *Reaction Kinetics and Catalysis Letter*, 17, 1981, p. 329
 - 35 S. C. Chang, *Journal of Vacuum Science & Technology*, 17, 1980, p. 366
 - 36 T. A. Gundrizer, A. A. Davydov, *Reaction Kinetics and Catalysis Letter*, Vol. 3 (1), 1975, p. 63
 - 37 S. Lenaerts, M. Honore, G. Huyberegts, J. Roggen, G. Maes, *Sensors and Actuators B*, 18-19, 1994, p. 478
 - 38 E. Giamello, Z. Sojky, M. Che, A. Zechhina, *Journal of Physical Chemistry B*, 90, 1986, p. 6084
 - 39 P. G. Harrison, E. W. Thornton, *Tin Oxide Surfaces*, Part 4, 1977
 - 40 C. Li, K. Domen, K. I. Maruya, T. Onishi, *Journal of the American Chemical Society*, 111, 1989, p. 7683
 - 41 M. Che, A. J. Tench, *Advances in Catalysis*, 31, 1982, p. 77
 - 42 M. Che, A. J. Tench, *Advances in Catalysis*, 32, 1983, p. 1
 - 43 P. G. Harrison, A. Guest, *Journal of the Chemical Society, Faraday Transaction 1: Physical Chemistry in Condensed Phases*, 83, 1987, p. 3383
 - 44 J. B Peri, *Journal of Physical Chemistry*, 69, 1965, p. 220
 - 45 H. Knötzinger, P. Ratnasamy, *Catalysis Reviews: Science and Engineering*, 1978, 17, p. 31
 - 46 A. A. Tsyganenko and P. P. Mardilovich, *Journal of the Chemical Society, Faraday Transaction*, 92, Nr 23, 1996, p. 4843

-
- 47 M. I. Zaki, H. Knözinger, *Materials Chemistry and Physics*, 17, 1987, p. 201a
- 48 D. B. Mawhinney, J. A. Rossin, K. Gerhart, J. T. Yates, Jr. 16, *Langmuir*, 2000, p. 2237
- 49 J. Weiss, *Mechanistische Aspekte der Photokatalyse von 2-Propanol und Pt/TiO₂ im Vergleich zur Tieftemperatur – Photooxidation in Festen Gasmatrizen. Eine IR-Spektroskopische Untersuchung*, PhD Thesis, University of Tübingen, 1991
- 50 W. J. Langer, *Mechanistische Aspekte der Adsorption von Wasser und Methanol auf Zinkoxid-Pulvern im Vergleich zu Titandioxid-Pulvern. - Zeitaufgelöste DRIFT-Spektroskopie-*, PhD Thesis, University of Tübingen, 1996
- 51 M. A. Hasan, M. I. Zaki, L. Pasupulety, *Journal of Molecular Catalysis A: Chemical*, 178, 2002, p. 125
- 52 M. A. Hasan, M. I. Zaki, L. Pasupulety, *The Journal of the Physical Chemistry, B*, 106, 2002, p. 12747
- 53 M. Primet, P. Pichat, M. V. Mathieu, *Journal of Physical Chemistry*, 75 (9) 1971, p. 1216
- 54 M. Primet, P. Pichat, M. V. Mathieu, *Journal of Physical Chemistry*, 75 (9) 1971, p. 1221
- 55 M.-I. Baraton, L. Merhari, *Nanostructured Materials*, 10 (5), 1998, p. 699
- 56 C. Lampropoulos, *Die Photooxidation von 2-Propanol an SnO₂-Oberflächen im Vergleich zur Photoreaktion mit SnO₂- Molekülen in Tieftemperaturmatrizen. - Eine IR-spektroskopische Untersuchung-*, PhD Thesis, University of Tübingen, 1995
- 57 N. Sergent, P. Gelin, L. Perier-Camby, H. Praliaud, G. Thomas, *Sensors and Actuators B*, 84, 2002, p. 176
- 58 N. Sergent, P. Gelin, L. Perier-Camby, H. Praliaud, G. Thomas, *Physical Chemistry Chemical Physics*, 4, 2002, p. 4802
-

-
- 59 E. Finocchio, G. Busca, V. Lorenzelli, V. S. Escribano, *Journal of the Chemical Society, Faraday Transaction*, 92 (9), 1996, p. 1587
- 60 R. Pohle, *In-Situ-Untersuchungen gassensitiver Prozesse an Metalloxidoberflächen mit Infrarotspektroskopischen Methoden*, PhD Thesis, Technische Universität München, 2000
- 61 C. D. Kohl, *Gas Sensors*, Chap. 2, Kluwer, Dordrecht, 1992, p. 43
- 62 M. Egashira, M. Nakashima, S. Kawasumi, *Journal of the Chemical Society, Chemical Communications*, 1981 (20), p. 1047
- 63 K. Morishige, S. Kittaka, T. Morimoto, *Bulletin of the Chemical Society of Japan*, 53, 1980, p. 2128
- 64 E. W. Thornton, P. G. Harrison, *Tin Oxide Surfaces Part I*, 1975, p. 461
- 65 A. Guest, PhD Thesis, University of Nottingham, 1985
- 66 F. Berger, E. Beche, R. Berjoen, D. Klein, A. Chambaudet, *Applied Surface Science*, 93, 1996, p. 9
- 67 Y. Matsuura, K. Takahata, K. Ihokura, *Sensors and Actuators*, 14, 1988, p. 223
- 68 K. D. Schierbaum, U. Weimar, W. Göpel, *Sensors and Actuators*, 3, 1991, p. 205
- 69 V. A. Heinrich, P. A. Cox, University Press, Cambridge, p. 312
- 70 M. Caldararu, D. Sprinceana, V. T. Popa, N. I. Ionescu, *Sensors and Actuators B*, 30, 1996, p. 35
- 71 D. S. Vlachos, P. D. Skafidas, J. N. Avaritsiotis, *Applied Physics Letter*, 63, 1993, p. 13
- 72 R. Ionescu, A. Vancu, C. Moise, A. Tamescu, *Sensors and Actuators B*, 61, 1999, p. 39
- 73 G. L. Miessler, D. A. Tarr, *Inorganic Chemistry*, Prentice-Hall, New Jersey, 1991
- 74 D. Scarano, S. Bertarione, G. Spoto, A. Zechhina, C. Otero Arean, *Thin Solid Films*, 400, 2001, p. 50
- 75 D. Scarano, A. Zecchina, *Spectrochimica Acta*, 43A, No.12, p. 1441
-

-
- 76 L.-F. Liao, C.F. Lien, D.-L. Shieh, M.-T. Chen, J.-L. Lin, *The Journal of Physical Chemistry*, 106, 2002, p. 11240
- 77 F. Bocuzzi, A. Chiorino, E. Guglielminotti, *Surface Science*, 368, 1996, p. 264
- 78 J. F. Boyle, K. A. Jones, *Electron. Mater.*, 6, 1977, p. 717
- 79 S. J. Gentry, T. A. Jones, *Sensors and Actuators*, 10, 1986, p. 1
- 80 H. Windischmann, P. Mark, *Journal of the Electrochemical Society: Solid State Science Technology*, 126, 1979, p. 672
- 81 M. J. Willet, *Techniques and Mechanism in Gas Sensing*, Vol. 3, Adam Hilger, Bristol, 1991, p. 61
- 82 P. K. Clifford, D. T. Tuma, *Sensors and Actuators*, 3, 1982/83, p. 233
- 83 R. Ionescu, A. Vancu, *Applied Surface Science*, 74, 1994, p. 197 (297)
- 84 J. Kappler, N. Barsan, U. Weimar, W. Göpel, *Conf. Proc. EUROSENSORS XI*, Warschau (P)
- 85 J. Kappler, *Characterisation of high-performance SnO₂ gas sensors for CO detection by in situ techniques*, PhD Thesis, University of Tübingen, 2001
- 86 C. Xu, J. Tamaki, N. Miura, N. Yamazoe, *Sensors and Actuators B*, 3, 1991, p. 71
- 87 N. Yamazoe, *Sensors and Actuators B*, 17, 1994, p. 241
- 88 V. Ambrazeviciene, A. Galdikas, S. Grebinskij, A. Mironas, H. Tvardauskas, *Sensors and Actuators B*, 4, 1993, p. 27
- 89 Duk-Dong Lee, Byung-Ki Sohn, *Sensors and Actuators*, 12, 1987, p. 441
- 90 G. S. V. Coles, S. E. Bond, G. Williams, *Sensors and Actuators B*, 4, 1991, p. 485
- 91 D. Bianci, G. E. Garder, G. M. Pajong, S. J. Teichner, *Journal of Catalysis* 38, 1975, p. 135
- 92 K. M. Sancier, *Journal of Catalysis*, 20, 1971, p. 106
- 93 P. A. Sermon, G. C. Bond, *Catalysis Reviews*, 8, 1973, p. 211

-
- 94 G. E. Batley, A. Exstrom, D. A. Johnson, *Journal of Catalysis*, 36, 1975, p. 285
 - 95 G. Ghiotti, A. Chiorino and F. Boccuzzi, *Sensors and Actuators*, 19, 1989, p. 151
 - 96 A. Chiorino, G. Ghiotti, F. Prinetto, M. C. Carotta, G. Martinelli, M. Merli, *Sensors and Actuators B*, 44, 1997, p. 474
 - 97 Harrick cooperation
 - 98 S. Emiroglu, *Infrarotspektroskopische Untersuchungen an SnO₂-Pulvern und Gassensoren*, Diploma Thesis, University of Tübingen, 2000
 - 99 B. Orel, U. Lavrencic-Stangar, Z. Crnjak-Orel, P. Bukavec, M. Kosec, *Journal of Non-Crystalline Solids*, 167, 1994, p. 272
 - 100 R. S. Hiratsuka, C. V. Santilli, D. V. Silva, S. H. Pulcinelli, *Journal of Non-Crystalline Solids*, 147/148, 1997, p. 67
 - 101 X. Liu, R. E. Truid, *The Journal of the American Chemical Society*, 1997, 119, p 9856
 - 102 G. Ghiotti, A. Chiorino, W. Pan, L. Marchese, *Sensors and Actuators B*, 7, 1992, p. 691
 - 103 International Union of Pure and Applied Chemistry, Commission on Molecular Structure and Spectroscopy, "Tables of Wavenumbers for the Calibration of Infra-Red Spectrometers", London, Butterworths, 1961, Reprinted from *Pure and Applied Chemistry*, Vol. 1, No. 4
 - 104 P. Concepción, B. M. Reddy and H. Knözinger, *Physical Chemistry Chemical Physics* 1, 1999, p. 3031
 - 105 M. J. Willet, *Tin (IV) Oxide Gas Sensors*, PhD Thesis, 1987
 - 106 M. J. Willet, *Techniques and Mechanism in Gas Sensing*, Vol. 3, Adam Hilger, Bristol, 1991, p. 89
 - 107 P. K. Dutta, A. Ginwalla, B. Hogg, B. R. Patton, B. Chieroth, Z. Liang, P. Gouma, M. Mills and S. Akbar, *The Journal of Physical Chemistry B*, 103, 1999, p. 4412

-
- 108 Nakamoto, *Infrared Spectra of Inorganic and Coordination Compounds*, Wiley Interscience, 1970, p. 166
- 109 S. Harbeck, A. Szatvanyi, N. Barsan, U. Weimar, V. Hoffmann, *Thin Solid Films*, 436, 2003. p. 76
- 110 W. Schmid, Consumption measurements on SnO₂ sensors in low and normal oxygen concentration, PhD Thesis, University of Tübingen, 2004
- 111 S. Hahn, SnO₂ thick film sensors at ultimate limits: Performance at low O₂ and H₂O concentrations; Size reduction by CMOS technology, PhD Thesis, University of Tübingen, 2002
- 112 F. Prinetto, G. Ghiotti, *The Journal of Physical Chemistry B*, 2000, 104, p. 11117
- 113 M. A. Barteau, *Journal of Vacuum Science & Technology*, 11, 1993, p. 2162
- 114 S. R. Morrison, *The Chemical Physics of Surfaces*, Plenum Press, New York, 1990
- 115 C. Morterra, E. Garrone, V. Bolist, B. Fubini, *Spectrochimica Acta*, 43A, No. 12, 1987, p. 1577
- 116 S. R. Morrison, *Sensors and Actuators* 11, 1987, p. 83
- 117 A. Chiorino, G. Ghiotti, F. Prinetto, M.C. Carotta, C. Malagu, G. Martinnelli, *Sensors and Actuators B*, 78, 2001, p. 89

List of Publications

Part of this work was already published as

FULL PAPERS

In situ diffuse reflectance infrared spectroscopy study of CO adsorption on SnO₂, S. Emiroglu, N. Barsan, U. Weimar, V. Hoffmann, Thin Solid Films, 391, 2001, 176-185.

Drift studies of thick film un-doped and Pd-doped SnO₂ sensors: temperature changes effect and CO detection mechanism in the presence of water vapour, S. Harbeck, A. Szatvanyi, N. Barsan, U. Weimar, V. Hoffmann, Thin Solid Films, 436, 2003, 76-83.

CONFERENCE PRESENTATIONS

Diffuse Reflectance Infrared Spectroscopy Study of Water Vapour-CO Interaction at the Surface of SnO₂ Powders, S. Emiroglu, N. Barsan, U. Weimar, V. Hoffmann, Conf. Proc. IMCS 2000, Basel / Switzerland, 2000, 344.

In situ DRIFT Studies on Adsorption Phenomena on SnO₂, S. Emiroglu, N. Barsan, U. Weimar, V. Hoffmann, II International Seminar on Semiconductor Gas Sensors (SGS), Ustron / Poland, 2000.

DRIFT-Investigations on SnO₂ surfaces, S. Harbeck, N. Barsan, U. Weimar, V. Hoffmann, GdCh: Elektrochemisches Grundlagensymposium: Elektrokatalyse und heterogene Katalyse, Pommersfelden / Germany, 2001.

DRIFT Studies of Thick Film SnO₂ Sensors: Direct Characterization and CO Detection Mechanism, S. Harbeck, A. Szatvanyi, N. Barsan, U. Weimar, V.

Hoffmann, Conf. Proc. EUROSENSORS XVI, Prague / Czech Republic, 2002, 243-244.

DRIFT Studies of Thick Film SnO₂ Sensors: Direct Characterization and CO Detection Mechanism, S. Harbeck, A. Szatvanyi, N. Barsan, U. Weimar, V. Hoffmann, III SGS, Ustron / Poland, 2002.

Effects of the Pd Dopant on the Surface Reactions of SnO₂ Thick Film Sensors, S. Harbeck, A. Szatvanyi, N. Barsan, U. Weimar, V. Hoffmann, 203rd Meeting of the Electrochemical Society, Paris / France, 2003, Abstract #2878.

Work not related to this thesis:

Alkyl chain effects in thin films of substituted phthalocyanines studied using infrared spectroscopy, A. Haug, S. Harbeck, D. Dini, M. Hanack, M. J. Cook, H. Peisert, T. Chassé, submitted to Applied Surface Science,

Influence of the alkyl chain lengths in substituted phthalocyanines on their interface and bulk properties, A. Haug, S. Dick, S. Harbeck, D. Dini, M. Hanack, H. Peisert, T. Chassé, AOFA 13, Angewandte Oberflächen Analytik Dresden / Germany, 2004.

Meine akademischen Lehrer:

K. Albert, E. Bayer, D. Christen, H. Eckstein, G. Gauglitz, F. Gönnerwein, W. Göpel, G. Häfelinger, H. Hagenmaier, M. Hanack, V. Hoffmann, W. Jäger, G. Jung, S. Kemmler-Sack, W. Koch, B. Koppenhöfer, D. Krug, N. Kuhn, E. Lindner, M. E. Maier, H.-J. Meyer, U. Nagel, H. Oberhammer, D. Oelkrug, H. Pauschmann, G. Pausewang, H. Pommer, G. Reinhardt, K.-D. Schierbaum, V. Schurig, E. Schweda, F. F. Seelig, H. Stegmann, J. Strähle, U. P. Weimar, W. Voelter, K.-P. Zeller, C. Ziegler

Danksagung

Diese Arbeit wurde von PD Dr. U. Weimar, Prof. Dr. V. Hoffmann und Dr. N. Barsan begleitet. Zu allererst möchte ich ihnen für ihr stetiges Interesse an dieser Arbeit und für ihre individuelle Unterstützung ganz herzlich danken. Ich konnte durch diese Zusammenarbeit sehr vieles erfahren und lernen.

PD Dr. Udo Weimar danke ich für die Überlassung des interessanten Themas und für die hervorragenden Arbeitsbedingungen, die es mir ermöglichten auf einem weiten Feld wertvolle Erfahrungen zu sammeln. Dank seines Vertrauens konnte ich an zahlreichen Konferenzen und Forschungsprojekten teilnehmen, bei denen ich vielseitige Einsichten bekommen habe. Er hatte immer ein offenes Ohr für mich und seine persönliche Unterstützung in entscheidenden Momenten hat mir sehr viel bedeutet.

Besonders danken möchte ich meinem geschätzten Lehrer Herrn Prof. Dr. Volker Hoffmann für die beispielhafte Betreuung. Er hat versucht, mir nicht nur von seinem Ozean an großem Wissen etwas weiterzugeben, sondern auch gezeigt beim alltäglichen Kampf mit den verschiedenen Geräten mit den praktischen Problemen umzugehen. Ohne seine Hilfe insbesondere bei der Interpretation der Spektren und seine hilfreichen Diskussionen wäre es mir viel schwerer gefallen, diese Arbeit in der jetzigen Form anzufertigen. Zu jeder Zeit hat mir die Zusammenarbeit mit ihm sehr viel Freude bereitet.

Dr. Nicolae Barsan danke ich für sein stetiges Interesse an meiner Arbeit und für die sehr fruchtbaren Diskussionen, die zu dieser Arbeit sehr vieles beigetragen haben. Seine Art der Motivation hat mich immer vorangetrieben. Es war zudem immer ein großes Erlebnis mit ihm auf Dienstreise zu gehen.

Jürgen Kappler danke ich für die Versorgung mit Sensoren für diese Arbeit. Bei der Zusammenarbeit und den gemeinsamen MISSY-Projekttreffen habe ich ihn sehr schätzen gelernt.

Dr. Alexandru Oprea danke ich für seine technische Hilfe beim Aufbau der Messanlage und die angenehme Zusammenarbeit.

Ich danke außerdem Prof. Dr. Dines Christen für seine Anregungen auf dem Gebiet der Spektroskopie und seine immerwährende Hilfsbereitschaft.

Wolfgang Neu, Reiner Schwarzer, Klaus Schaupp und seinen Mitarbeitern danke ich für die Hilfe beim Aufbau sowie die schnelle Anfertigung und Reparatur der Apparaturen.

Christine Weinl, Michael Wandel, Wolf Schmid, Simone Hahn, Georg Belge, Matthias Vollprecht und Jan Claußen danke ich für die gute Zusammenarbeit und insbesondere für die schöne Zeit in Tübingen seit Studienbeginn. Die lustigen Abende und die viele zusammen verbrachte Zeit werden mir immer in Erinnerung bleiben. Ein Dankeschön geht auch an Almuth Liebich, die leider frühzeitig in die weite Welt gezogen ist.

Ich danke allen meinen ehemaligen und jetzigen Kollegen im VG und im B-Bau. An dieser Stelle möchte ich die ehemaligen Kollegen Stefan Strathmann, Michael Frank, Christopher Fietzek, Andreas Krauss, Nico Papamichail und Martin Herold hervorheben. Die Mittagspausen im „Kalender“ mit anschließendem Besuch des „Pico“ und die lustigen Skiurlaube auf dem Golm liegen leider weit zurück.

PD Dr. Götz Reinhard und seinen ehemaligen Mitarbeitern Olaf Wurzinger, Martin Rösch und Ralf Meyer danke ich für ihre Hilfe bei der „Motorola“-anlage und für den Spaß im 10. Stock.

Prof. Dr. T. Chassé möchte ich danken für die Bereitstellung der neuen, interessanten Aufgaben, die es mir ermöglicht haben, weitere Erfahrungen auf dem Gebiet der Spektroskopie zu sammeln.

Meinem Zimmerkollegen Zhang Lei danke ich für die sehr angenehme Zusammenarbeit und zusammen mit Tobias Nischalke für das Korrekturlesen dieser Arbeit.

Ganz besonders möchte ich meinem Mann Mika Harbeck danken für seine stetige Hilfsbereitschaft und insbesondere für sein Verständnis für alle meine Launen während der Doktorarbeit.

Danken möchte ich auch meiner Familie in weiter Entfernung (Türkei, Norddeutschland, Finnland) für ihre vielfältige Unterstützung während des Studiums und bei der Doktorarbeit.

Den Projektpartnern in MISSY und GASMOH gilt mein Dank für die gute Zusammenarbeit und den Geldgebern für die Finanzierung der Arbeit.
